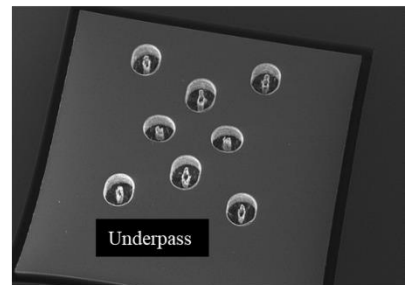
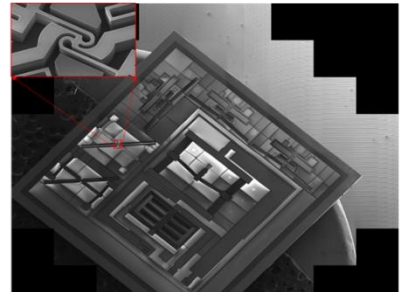
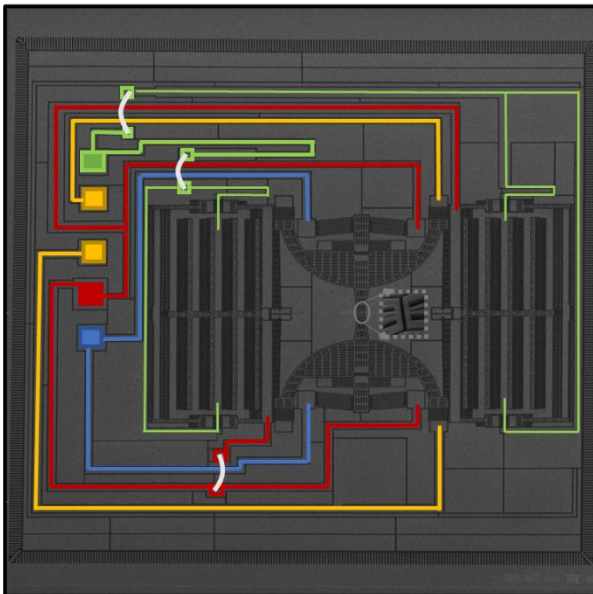


Naga Manikanta Kommanaboina

Development of MEMS-Based Devices for Characterizing 2D Nanomaterials at Low Temperatures





Doctoral School in Civil, Environmental and Mechanical Engineering
Topic 2. Mechanics, Materials, Chemistry and Energy – 35° cycle 2019/2023

Doctoral Thesis – November 2023

Naga Manikanta Kommanaboina

Development of MEMS-Based Devices for Characterizing 2D Nanomaterials at Low Temperatures

Supervisors

Assoc. Prof. Maria Pantano, University of Trento

Mr. Alvisè Bagolini, Fondazione Bruno Kessler



Contents on this book are licensed under a Creative Common Attribution
Non Commercial - No Derivatives
4.0 International License, excepts for the parts already published by other publishers.

University of Trento
Doctoral School in Civil, Environmental and Mechanical Engineering
<http://web.unitn.it/en/dricam>
Via Mesiano 77, I-38123 Trento
Tel. +39 0461 282670 / 2611 - dicamphd@unitn.it

Acknowledgments

I would like to express my sincere gratitude to the many individuals and organizations whose support made the completion of this Ph.D. possible. First and foremost, I am deeply grateful to my dedicated supervisors, Assoc. Prof. Maria Pantano and Mr. Alvis Bagolini. Their consistent guidance and encouragement were crucial throughout my doctoral research journey. I appreciate the CNR Genova group for their valuable support during experiments and collaboration. Additionally, I extend special thanks to Mr. Teferi Sitotaw Yallew for his collaborative spirit during the fabrication process and motivation.

I extend my gratitude to Fondazione Bruno Kessler (FBK), with particular acknowledgment to the MNF and MST groups, for their research and facility support, which significantly contributed to the success of the thesis. Also, special thanks to the MONSTRE 2D project, funded by the MIUR Progetti di Ricerca di Rilevante Interesse Nazionale (PRIN) Bando 2017.

I would like to acknowledge the constant support and motivation provided by Revathi U and Sameer Balaji during my research period. Their encouragement was instrumental in keeping me focused and motivated. I owe a debt of gratitude to all my mentors, especially Mr. Ram Naresh K and teachers, for their invaluable insights and guidance throughout my academic journey.

My special thanks go out to my FBK colleagues for their assistance, support, and intellectual exchange. Their contributions enriched my research experience. I deeply appreciate my department (DICAM) and the university for providing constant support and the opportunity to delve into the current trendy topic, which has been both inspiring and challenging.

A heartfelt thank you goes out to my volleyball team members and friends for their support, providing a healthy balance to my academic pursuits.

Finally, and most importantly, I am deeply grateful as I dedicate my PhD achievement to my Parents.

Abstract

Investigates the mechanical and electronic properties of two-dimensional nanomaterials under strain, addressing gaps in the existing literature. The primary challenge with these materials is the inconsistent application of high strain rates and the absence of experimental data at low temperatures. To overcome these challenges, we develop Microelectromechanical Systems (MEMS)-based devices for characterizing 2D nanomaterials and semiconductor materials at low temperatures.

Four MEMS-based devices are developed to facilitate this characterization. The first device is a unique MEMS testing platform with on-chip actuation, sensing, and feedback control systems, capable of applying controlled displacements to nanoscale specimens while minimizing temperature fluctuations. To achieve this, MEMS thermal actuators with an axial stiffness of 40253.6 N/m are used. Capacitive sensors and V-beam amplification mechanisms are designed for precise measurement. The second device, the cascaded MEMS device, employs horizontal and vertical V-shaped structures to measure stress-strain curves of 2D nanomaterials at low temperatures. The third device is a customized MEMS electrostatic actuator for bending tests on silicon material under low-temperature conditions. Finally, two MEMS rotational structures, including a novel C-shaped structure, are developed to amplify movement.

The MEMS devices are fabricated using bulk micromachining and deep reactive-ion etching (DRIE) with silicon-on-insulator (SOI) wafers, incorporating underpass technology for electrical isolation within the MEMS-based testing platforms. To optimize DRIE etching parameters for creating underpass islands in SOI MEMS, a study was conducted considering a total of nine wafers, divided into two batches for fabrication process, and examining their behavior concerning the etching process.

The devices are optically characterized at room temperature and tested in a vacuum environment and at low temperatures using scanning tunneling microscope (STM) tool.

Contents

1.1 Introduction	4
1.2 Types of 2D nanomaterials.....	5
1.3 Strain Engineering	18
1.4 Types of Strain Applied to 2D Materials.....	19
1.5 Strain Induction Techniques in 2D Materials	21
Artificial Strain	24
1.6 Experimental Techniques of Studying Mechanical Properties in 2D Materials	37
1.6.1 In Situ Microscope Techniques	38
1.6.2 In Situ Integrated Microscopy Techniques	48
1.7 Challenges and Limitations	49
2.1 Introduction	51
2.2 MEMS-Based Tensile Testing Platforms	52
2.3 Mechanical Design of the Thermal Actuator.....	54
2.5 Numerical Modeling.....	58
2.5.1 Static Structural Simulations	60
2.5.2 Multiphysics Simulations	61
2.6 The Electro-Capacitive Sensor	65
2.6.1 Differential Transverse Comb-based Capacitors.....	65
2.6.2 Rotational Comb Drive.....	68
2.6.3 Parallel Plate Capacitive Sensor	73
2.6.4 Analytical Modelling.....	82
2.7. Final Configuration of MEMS-Based Tensile Testing Device....	85
3.1 Introduction	90
3.2 Design of MEMS Based Tensile Testing Platform-1	91
3.3 Analytical Modelling.....	92
3.3.1 Horizontal Thermal Actuators	92
3.3.2 Vertical V-Shaped Structure.....	93
3.4 Numerical Analysis	95

3.5 Design of MEMS Based Tensile Testing Platform-2	101
3.5.1 Analytical Modelling and Numerical Analysis	102
4.1 Introduction	107
4.2. Design and Analytical Modelling	109
4.2.1 Spring Design	109
4.2.2 Comb Drive Actuator	112
4.2.3 Static Structural Simulations	114
4.3 MEMS Based Rotational Structures	116
4.3.1 Mechanical Design of the C-Shaped Rotational Structure ..	118
4.3.1 Analytical and Numerical Modelling	123
5.1 Introduction	131
5.1.1 Surface and Bulk Micromechanics	132
5.1.2 SOI Micromechanics	133
5.2 Fabrication Technologies.....	133
5.2.1 Deposition Technology.....	134
5.2.2 Patterning Technology.....	137
5.2.3 Etching Technology.....	142
5.3 Mask Designing.....	144
5.4 Fabrication Sequence.....	149
5.4.1 Metal Deposition and Patterning	150
5.4.2 Metal Etching	151
5.4.3 Masking Layer Deposition	151
5.4.4 Silicon Etching	156
5.4.5 Final Processing with HF Vapor Etching	159
5.5 Wire Bonding Within the MEMS Device	160
6.1 Fabrication Results	165
6.2 Electrical Characterization at Room Temperature.....	172
6.2.1 MEMS Based Rotational Structures.....	173
6.2.2 MEMS Electrostatic Actuator.....	174
6.2.3 MEMS Based Tensile Testing Device.....	176

6.3 Electrical Characterization in Low Temperature STM's vacuum chamber	178
Conclusions	182
Future Works	184
Appendix	185
Bibliography	186

1.1 Introduction

In recent years, the research on 2D nanomaterials has seen a significant surge, with many new materials being synthesized and characterized. Graphene, discovered in 2004 by Novoselov and colleagues, is an extensively studied ultrathin 2D nanomaterial consisting of a single layer of carbon atoms arranged in a hexagonal lattice [1]. Its unique properties, including ultrahigh room-temperature carrier mobility, excellent electrical and thermal conductivities, and high Young's modulus, make it a popular subject of study. Boron nitride, another 2D material consisting of a single layer of boron and nitrogen atoms, has also been identified as a promising material. Novoselov and colleagues' simple method of using adhesive tape to isolate single layers of graphene and boron nitride has played a crucial role in the study of these materials. The materials have been studied using a range of techniques, including transmission electron microscopy and X-ray diffraction [2].

2D nanomaterials are highly attractive for a range of applications due to their unique electronic, optical, and mechanical characteristics. Additionally, their optical properties, such as absorption and emission, make them useful for photonics, optoelectronics, and biosensing. These materials are suitable for catalysis, energy storage and conversion, nanoelectronics, sensors, and membranes. The tunability of 2D nanomaterials is one of their main advantages, as their properties can be tailored to specific applications by manipulating their dimensions, composition, and structure. However, the low dimensionality of 2D nanomaterials can result in poor mechanical stability and limited electronic performance. Continued innovation in modulating the properties of 2D nanomaterials holds great promise for their future applications [3], [4]. To overcome these limitations, new approaches have been developed, such as confinement in the 2D plane, which leads to quantum confinement effects and enhanced surface-to-volume ratios. In this chapter, the concept of strain engineering and its applications to 2D nanomaterials is introduced. The different types of 2D nanomaterials are discussed and the different types of strain that can be applied to these materials are explored. Various techniques for inducing strain in 2D materials and for studying their mechanical properties experimentally are also discussed.

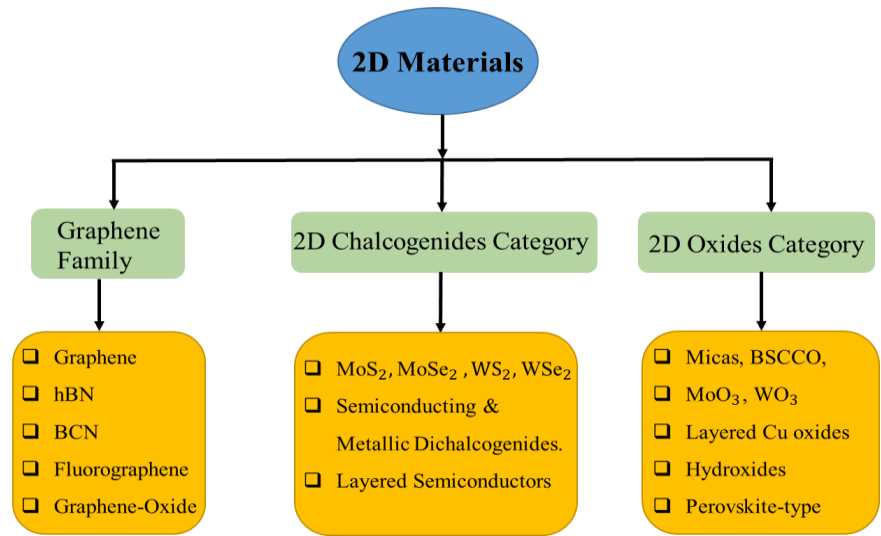


Figure. 1.1: Main Categories of 2D Nanomaterials [5].

1.2 Types of 2D nanomaterials

The unique properties of 2D nanomaterials have made them a focus of research in recent years. These materials are known for their high surface area, exceptional mechanical and electrical properties, and tunable electronic structures, which make them attractive for various applications. The field of 2D materials encompasses a wide range of materials with unique electronic, optical, and mechanical properties. Three main categories of 2D materials can be distinguished: the Graphene family, 2D chalcogenides, and 2D oxides, as shown in Figure 1.1. Graphene, a single layer of carbon atoms arranged in a hexagonal lattice, is known for its exceptional strength, electrical conductivity, and thermal conductivity, making it highly sought after in electronics and energy storage. The 2D chalcogenides category includes materials such as molybdenum disulfide and tungsten diselenide, which exhibit unique optical and electronic properties, useful in applications such as LEDs and solar cells. The 2D oxides category includes materials such as titanium oxide and zinc oxide, which can exhibit a range of electronic and optical properties and have potential applications in catalysis, energy storage, and sensing.

There are various types of 2D nanomaterials that have become attractive these days, each with distinct properties and applications. The discovery of graphene led to the investigation of other 2D materials such as transition metal dichalcogenides (TMDs), hexagonal boron nitride (h-BN), and other materials. TMDs, for example, are semiconducting materials that can be used in electronic and optoelectronic devices, while h-BN has excellent insulating properties and can be used as a substrate for graphene-based devices, shown in Figure 1.2. The family of graphene-based 2D materials is expanding rapidly, and scientists are exploring their unique properties and potential applications.

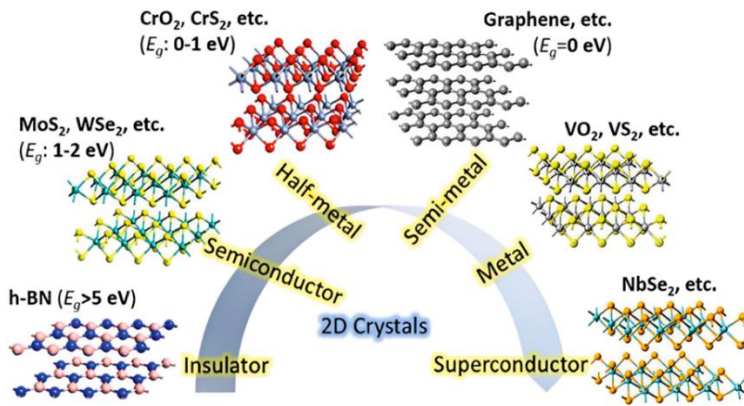


Figure. 1.2. Properties of 2D materials in different categories from insulator to superconductor [6].

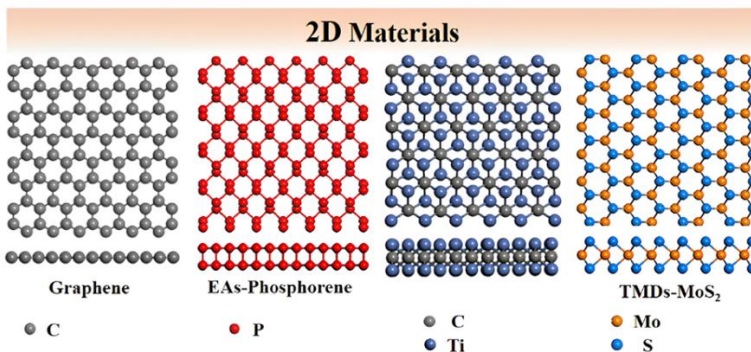


Figure. 1.3: Crystalline structures of various 2D materials [7].

Graphene is a well-known 2D nanomaterial that consists of a single layer of carbon atoms in a hexagonal lattice structure. With a thickness of 0.34 nm, it has remarkable mechanical, thermal, and electrical properties. Graphene, with its C-C bond distance of 0.142 nm (shown in Figure 1.4), has been studied for its potential use in numerous applications including energy storage, sensors, and electronic devices [8], [9]. The carbon atoms in graphene are arranged in a hexagonal lattice structure and each of these atoms is sp^2 hybridized. This means that each carbon atom forms three bonds with its neighboring carbon atoms, as illustrated in Figure 1.3 [10], [11]. Graphene exhibits exceptional mechanical, thermal, and electrical properties, making it an ideal candidate for a range of applications. Its high tensile strength and flexibility have led to its use as a reinforcement material in composites [12]. Its excellent thermal conductivity makes it suitable for use in heat management systems [13], while its high electrical conductivity has been investigated for use in electronics and energy storage devices. Graphene's surface area-to-volume ratio and its ability to selectively absorb molecules make it a promising candidate for use in sensors and catalysis [10], [11]. Graphene has been studied extensively for its potential use in various fields such as nanoelectronics, optoelectronics, biomedicine, and energy conversion and storage. Researchers continue to explore new ways to manipulate the properties of graphene to unlock its full potential in these areas [8], [9]. Additionally, graphene is nearly transparent, with a high optical transmittance of about 97%, making it suitable for use in transparent conductive films [10].

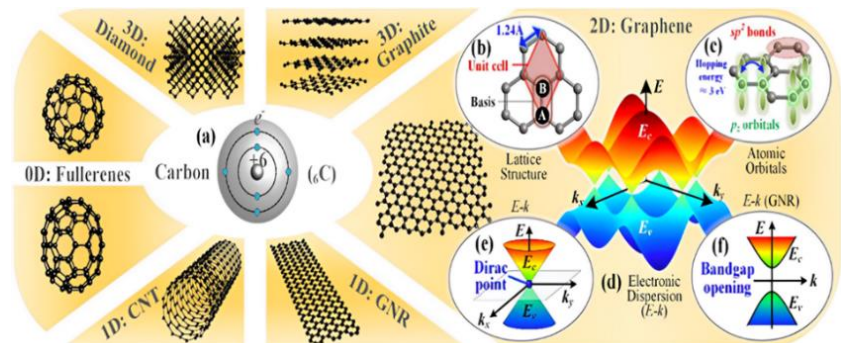


Figure. 1.4: Illustrates (a) different carbon allotropes, ranging from 0D to 3D, (b) unit cell of graphene, (c) atomic orbitals of graphene, (d, e) The energy dispersion of graphene, (f) The energy dispersion of a semiconducting graphene nanoribbon (GNR) [6].

Graphene's remarkable strength, with a tensile strength of about 130 gigapascals with young's modulus of 1 TPa, can be attributed to the covalent bonding between the carbon atoms in the graphene lattice, which creates a rigid and stable structure [12]. Graphene-based materials have shown great potential in thermal management applications. A study demonstrated that a graphene-epoxy composite exhibited a thermal conductivity of up to 15 W/mK, which is significantly higher than other conventional thermal interface materials [13]. Moreover, graphene-based thermal interface materials have been developed that exhibited excellent thermal conductivity and mechanical properties, making them a promising candidate for aerospace thermal management applications. Graphene-based composites have been studied for their potential as high-performance electromagnetic interference (EMI) shielding materials for aerospace applications, high-performance thermal interface materials for electronic devices, and high-performance composites for various applications, including aerospace, automotive, and sports equipment. Graphene oxide has also been investigated for its potential in the development of antibacterial materials for various applications [14].

Graphene-based materials have also been studied for their potential in aerospace applications in the form of coatings. A recent study reported the development of a graphene oxide-based coating that exhibited excellent corrosion resistance properties, including high barrier properties, high mechanical strength, and high chemical stability [15]. Some of the technical data mentioned in the paper includes the use of graphene oxide-based coatings to protect steel and aluminium alloys, as well as the use of these coatings to reduce the corrosion rate of copper in acidic solutions. The researchers found that the coating effectively protected aerospace components and structures from corrosion in harsh environments [16]. The use of graphene-based coatings in aerospace applications could have a significant impact on the performance and reliability of aerospace components and structures. Corrosion is a major problem in the aerospace industry, and the development of effective corrosion-resistant coatings is essential for ensuring the safety and longevity of aerospace systems. Aircraft corrosion is a complex issue that involves several different types of corrosion. These include uniform, exfoliation, intergranular, and pitting corrosion, as shown in

Figure 1.5 a-d. These forms of corrosion can have varying appearances and may be caused by different mechanisms, either on their own or in combination. The impact of each type of corrosion on structural performance can also differ significantly. Due to the complexity and diversity of corrosion, it can be difficult to monitor and manage effectively.

Graphene-based materials have attracted significant attention in the development of sensors due to their unique properties. These properties make them ideal candidates for use in various sensing applications. Graphene-based sensors have been shown to exhibit high sensitivity to various analytes, such as gases and biomolecules. For instance, graphene-based gas sensors have been shown to have high sensitivity to gases such as NO_2 , NH_3 , and H_2S . Moreover, graphene-based biosensors have been used for the detection of various biomolecules, such as DNA, proteins, and viruses [17].

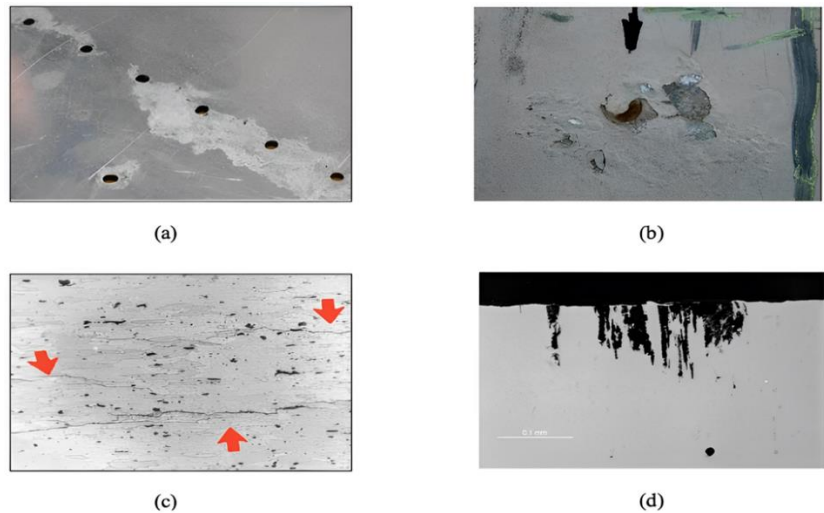


Figure. 1.5: (a) Uniform corrosion on an aluminium aircraft structure (b) Exfoliation corrosion at fastener holes in F-18 upper wing skins (c) Intergranular corrosion of a failed 7075-T6 aluminium aircraft component (d) Pitting corrosion resulted from the corrosion media attaching to the exposed end grains [16].

The selectivity of the sensors can be enhanced through various functionalization techniques, such as surface modification and chemical doping. Graphene-based sensors have also been shown to have fast

response times, allowing for rapid detection of analytes. For example, some graphene-based gas sensors have response times in the order of seconds [18]. Graphene-based sensors can also exhibit high stability over time, allowing for long-term sensing applications. The stability of the sensors can be enhanced through various encapsulation and protection techniques. Additionally, graphene-based sensors can be integrated with other electronic components, allowing for the development of miniaturized sensing devices. The integration of the sensors can be achieved through various methods, such as inkjet printing and microfabrication techniques [19]. However, there are some challenges associated with the use of graphene-based materials in sensing applications, such as their tendency to aggregate and their sensitivity to environmental factors such as temperature and humidity. Further research is needed to optimize the fabrication methods and properties of graphene-based sensors and to address these challenges for their successful integration in various sensing applications.

Graphene and graphene-based materials have been extensively studied for their potential use in a variety of energy storage applications, including batteries, supercapacitors, and fuel cells. Their exceptional properties such as high surface area, excellent electrical conductivity (up to $\sim 10^6$ S/cm), mechanical strength (with a Young's modulus of 1 TPa), and chemical stability make them attractive candidates for these applications [19], [20]. The use of graphene-based materials in energy storage devices can improve the performance, durability, and safety of these devices. High electrical conductivity of graphene can enhance the electron transfer rate and improve the energy storage capacity of the devices. The excellent thermal and chemical stability of graphene-based materials can prevent thermal runaway and improve the durability and lifespan of the devices. Additionally, combining graphene with other materials such as metal oxides and polymers can further enhance the electrochemical activity and stability of the materials. The promising properties of graphene and graphene-based materials make them potential candidates for the future of energy storage technology, and optimizing their properties and fabrication methods is essential for their successful integration into energy storage devices [20].

Graphene and graphene-based materials (GBMs) have unique physical, chemical, and biological properties that make them attractive for a variety of biomedical applications, such as drug delivery, biosensing,

and tissue engineering [21]. GBMs have high surface area, excellent mechanical strength, and biocompatibility, and have shown antibacterial, anti-inflammatory, and anticancer properties. GBMs have been used as drug carriers to enhance drug solubility and stability, as well as to improve drug targeting and release. The large surface area and high electrical conductivity of GBMs have also been exploited for biosensing applications, such as glucose and DNA sensing. GBMs have been investigated for their potential in tissue engineering due to their ability to support cell growth and proliferation. However, the biocompatibility and safety of GBMs still need to be thoroughly evaluated to ensure their safe use in biomedical applications.

In the field of flexible electronics, GBMs have been developed into thin films using chemical vapor deposition and transferred onto flexible substrates, exhibiting high conductivity (up to 5,000 S/cm), flexibility, and transparency (> 90% in the visible range) [22]. These materials have the potential to be used in various electronic devices, including displays and touchscreens. Researchers have demonstrated a graphene-based light-emitting device that exhibited high efficiency (up to 1.6%) and flexibility with stable performance under bending and twisting. In the field of water purification, GBMs have been developed into graphene oxide-based membranes using vacuum filtration methods [23]. These membranes have exhibited high water flux (up to 4,800 L/m²/h) and removal efficiency for various contaminants, including dyes, heavy metals, and bacteria (> 99.9% removal). Graphene oxide-based membranes have the potential to improve the efficiency of water treatment processes. Furthermore, researchers have developed a graphene oxide-based membrane using vacuum filtration and thermal reduction, exhibiting high permeability (up to 1010 L/m²/h/bar) and selectivity (> 97% rejection) for water filtration. These materials have potential applications in desalination and purification of contaminated water sources.

Hexagonal boron nitride (h-BN) is another type of two-dimensional material with a hexagonal lattice structure similar to graphene (shown Figure 1.6) but composed of alternating boron and nitrogen atoms instead of carbon [24]. It has received significant attention due to its unique properties such as wide bandgap, high thermal stability, and excellent dielectric properties. h-BN also exhibits high mechanical

strength, chemical inertness, and high thermal conductivity, making it a promising material for various applications, including electronics, optics, and energy storage [25].

In electronics, h-BN has been used as a dielectric material in various electronic devices, including field-effect transistors (FETs) and vertical tunnel FETs, resulting in improved device performance and reduced power consumption. Additionally, h-BN has been explored for its potential use in optics, serving as a substrate for growing other 2D materials such as graphene and transition metal dichalcogenides (TMDs) which exhibit strong photoluminescence and good electrical properties [26]. It has also been used as a substrate for graphene-based photodetectors, resulting in high responsivity and fast response times [26], [27]. In the field of energy storage, h-BN has been investigated as a separator material in lithium-ion batteries, resulting in higher capacity and longer cycle life. It has also been used as a host material for sodium-ion batteries, resulting in improved electrochemical performance and stability. These promising applications demonstrate the potential of h-BN as a versatile material in various fields [28].

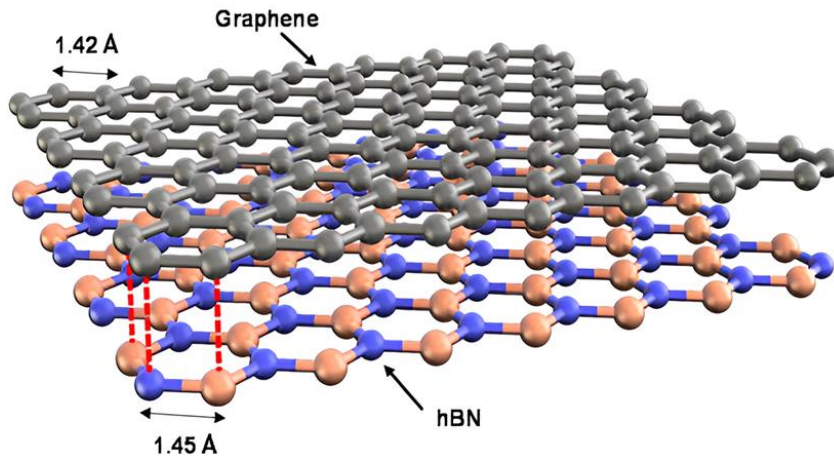


Figure. 1.6. Honeycomb lattice structures of Graphene and h-BN matching [27].

Several studies have been conducted on the mechanical properties of hexagonal boron nitride (h-BN). One study proposed a method to study high order elastic constants of 2D hexagonal structures and obtained a continuum description of the elastic properties of monolayer h-BN

using ab initio density functional theory [29]. Another study investigated the effects of h-BN content on the mechanical properties of produced lining samples and found that adding h-BN up to 10% by volume did not cause a significant change in hardness and bending strength values of linings [30]. Additionally, h-BN has been found to have mechanical robustness, thermal stability, and chemical inertness, making it a strong candidate for two-dimensional material in various applications [24], [28]. In addition to its unique properties, h-BN can form composites with various other materials such as metal chalcogenides and graphene oxide sheets.

Transition metal dichalcogenides (TMDs) are a class of materials that consist of a transition metal atom (such as Mo, W, or Nb) sandwiched between two chalcogen atoms (such as S, Se, or Te) in a layered crystal structure [3]. Unlike graphene, which is a semimetal, TMDs are semiconductors with a bandgap that can be tuned by changing their thickness. TMDs have unique electronic and optical properties, making them attractive for applications in optoelectronics, electronics, and energy storage. They can also be used as catalysts for various chemical reactions [31]. In their bulk form, TMDs are insulators or semiconductors. However, when they are thinned down to a few atomic layers, they become direct bandgap semiconductors with strong light-matter interactions. This property makes TMDs attractive for optoelectronic applications such as photodetectors, solar cells, and light-emitting diodes (LEDs). Additionally, TMDs have high carrier mobility, which makes them promise for applications in high-speed electronics [32]. TMDs also have high surface area and can be easily functionalized with different chemical groups, making them useful for energy storage applications such as supercapacitors and batteries. They can also act as efficient catalysts for various chemical reactions due to their unique electronic and structural properties [31]. Examples of TMDs include molybdenum disulfide (MoS_2), tungsten diselenide (WSe_2), and titanium disulfide (TiS_2), among others. Molybdenum disulfide (MoS_2) has been investigated more than other transition metal dichalcogenides (TMDs) for several reasons. Firstly, MoS_2 is one of the most abundant TMDs and is relatively easy to synthesize. MoS_2 is also used as a substitute for graphene and other semiconductor appliances with high capability of practices in nano-electronic, energy-storing,

photocatalysts, optical sensors, biosensors, and other applications [32], [33]. MoS₂-based nanostructures have unique physicochemical, optical, and electrical properties that have earned substantial thoughts from the scientific communities [34]. MoS₂ has also been extensively exploited in biomedical applications due to its unique physicochemical properties and biocompatibility [35]. Furthermore, MoS₂ can form heterostructures with other 2D materials, such as graphene or other TMDs, which can lead to novel properties and applications.

Molybdenum disulfide (MoS₂) is a 2D nanomaterial that has attracted significant interest due to its unique properties and potential applications. MoS₂ is a layered material consisting of molybdenum atoms sandwiched between two layers of sulfur atoms. This structure results in a high surface area, which makes MoS₂ an attractive material for a wide range of applications. MoS₂ is an inorganic compound that belongs to the transition metal dichalcogenides (TMDs) family, which consists of a transition metal like Molybdenum and a chalcogen like Sulfur. It has promising properties, such as a large band gap (~1.8 eV) that changes from an indirect gap to a direct one in thin structures, making it an ideal material for downscaling electronic devices. Unlike graphene, MoS₂ does not have surface dangling bonds and has high mobility even with high-κ dielectric materials. It is easy to fabricate and has a high yield at a low cost [36]. Furthermore, its covalent and Van der Waals bonds make it optimal for gas sensing, and it has less contact resistance and higher performance than Silicon. MoS₂ has a wide range of applications in different fields, including bio-applications like DNA, cancer, and Corona Virus detection. Studies have also shown that it may be effective in curing cancer and Alzheimer's disease and has no biological interaction, making it safe for injection in human bodies [33]. While Silicon-based semiconductor devices face issues related to quantum and tunneling effects at the nanoscale, MoS₂ has shown promise in terms of its electronic and quantum characteristics when transitioning from a bulk material to a two-dimensional structure [37]. The optical properties of MoS₂ are essential for its use in optoelectronics. MoS₂ has a high absorption coefficient (~500 nm) for short wavelengths and a low absorption coefficient for long wavelengths. Its tunable bandgap allows for a wide range of applications with different photoresponsivity and specific detectivity.

MoS₂ multilayers and monolayers have a high refractive index, making them useful in coating. The PL properties of monolayer MoS₂ can be enhanced by adding H₂O₂ solution. TMDs have a low PL quantum yield of between 0.01 and 6%, but MoS₂'s QY was improved to 95% by treating it with an organic superacid, which also increased its carrier lifetime to nearly 10.8 ns, making it useful for high-performance solar cells and lasers. The mechanical properties of monolayer MoS₂ are notable, with a high strength and good elasticity comparable to that of graphene oxide, and a Young's modulus of 0.33 ± 0.07 TPa. Additionally, its flexibility prevents deformation and band gap shifts, which can occur in other semiconductors under strain. However, strain can be used to change MoS₂ electronic properties from a semiconductor to a metal, causing deformation and transforming it to a metal at high strain values [38]. The electronic properties of MoS₂ multilayers are characterized by an indirect band gap of 1.2 eV, which increases as the number of layers decreases until a direct band gap of 1.8 eV is achieved in monolayer MoS₂. However, this value is still far from the direct band gap of silicon, which is 1.12 eV. The band gap of MoS₂ is affected by mechanical strain, which can change it from a direct to an indirect band gap and cause the material to transition from a semiconductor to a metal. The properties of MoS₂ are determined by the 4d and 3p orbitals in Mo and S, respectively. The projected density of states (PDOS) of bulk and monolayer MoS₂ are similar, but there are some peaks in PDOS in the case of monolayer MoS₂. Doping with certain elements can change the type of semiconductor MoS₂ is, with chromium, copper, and scandium causing it to behave as an n-type semiconductor and nickel or zinc causing it to behave as a p-type semiconductor. Doping with titanium can cause MoS₂ to behave as either a p-type or n-type semiconductor depending on the levels and sites of doping. At low doping levels of titanium below 2.04%, MoS₂ behaves as a p-type semiconductor. However, interstitial doping of titanium at 3.57% causes MoS₂ to behave as an n-type semiconductor, and at high doping levels of 7.69%, MoS₂ becomes a ferromagnetic half-metal with spin polarization of 1. The substitutional doping of titanium did not show any change in electronic properties for the three doping concentrations mentioned. With the advancement of spintronics and the shift towards nanoscale technology, it has become imperative to investigate the electron spin of materials such as MoS₂. TMDs, which are non-magnetic, have the potential to become tunable semiconductors if

magnetism can be induced in them. A study conducted on multilayer MoS₂ revealed that it possesses a long spin diffusion length of 235 nm, and that in-plane spin polarization can restrict electron spin-relaxation. Another study showed that MoS₂ exhibits semi-metallic ferromagnetic characteristics when doped with Sc, with a unity spin polarization value that is highly desirable in spintronics [38].

Black phosphorus (BP) is a two-dimensional material that has recently gained interest due to its unique properties, such as high mobility, tunable direct bandgap, and anisotropic properties. BP is the most stable phosphorus allotrope and can be produced through high temperature and pressure or mineralizer auxiliary synthesis [39]. BP has potential applications in various fields, including electronics, photonics, and biomedicine [39]–[41]. BP's unique structure, which includes puckered structures in the armchair direction and double-layered arrangements in the zigzag direction, gives it distinct thermoelectric, topological, electronic conductivity, and mechanical properties. These properties make BP an advanced material for use in moderate band gap-based nano-electronic and nanophotonic devices, as well as in optoelectronics, transistors, sensors, and thermoelectric applications. Research efforts are ongoing to deepen our understanding of BP's fundamental properties and to explore new applications for this material. BP nanostructures, prepared using chemical and mechanical exfoliation methods, demonstrate great potential for use in field-effect transistors, memory devices, diodes, demodulators, and photodetectors. BP is a material that exhibits a tunable band gap which can vary from 0.3 to 1.5 eV depending on the interlayer stacking pattern. This property, combined with enhanced anisotropic in-plane properties and charge carrier mobility, allows BP to absorb a wide range of light in the mid-infrared system of the solar spectrum, making it a promising material for use in photo detectors. Compared to graphene and other 2D materials, BP has better metal-semiconductor transformation, resulting in structural changes in the layer's number and stress level. This unique property makes BP an attractive material for use in catalysis. Black phosphorus (BP) exhibits unique electrical, thermal, and mechanical properties that make it a promising material for various applications. Both the single and multilayer forms of BP have direct but tunable bandgap properties, making it an ideal semiconductor device for

efficient photo-electrical conversion and light emission. The thermal conductivity anisotropy of BP is high and depends on the size, temperature, and strain of the material. The mechanical properties of BP show high mechanical ductility and anisotropy, making it superior to other 2D materials like graphene. When tensile strain is applied appropriately, the bandgap of BP can transition from direct to indirect, and the order of charge transportation can change. BP's mechanical anisotropy has been utilized in nanoelectromechanical devices, which exhibit excellent nanoelectromechanical attributes. Studies on the mechanical properties of BP have revealed its high mechanical ductility, excitable electronic arrangement, and extreme anisotropy. BP possesses good ductile strain in the armchair direction (30%) and the zigzag direction (27%) [42]. The mechanical anisotropy of BP nanosheets shows superior mechanical flexibility in Young's modulus compared with other 2D materials like graphene (44 GPa in armchair and 166 GPa in zigzag directions). Single-layer BP has excellent flexibility due to its smaller Young's modulus value. The tensile strain of phosphorene is weaker than those of MoS₂ and graphene, as the extension in bond angles and layer bond are less compared to the linear bond. The mechanical anisotropy of BP has been applied in nanoelectromechanical devices, which exhibit excellent nanoelectromechanical attributes. BP's ductility can be used to regulate the bandgap from direct to indirect and to change the charge transportation order [39]. In summary, the research shows that phosphorene has lower Young's modulus values compared to MoS₂ and graphene due to weak P-P bond interactions, and that the other 2D materials exhibit greater ductility than phosphorene under tensile strain. The study also found that the puckered honeycomb structure of BP, which contains sp³ non-equivalent hybridization of each P atom, gives rise to remarkable mechanical, thermal, electrical, and optical anisotropic properties. These findings provide insight into the potential for novel BP-based opto-electrical devices, especially in the realm of optoelectronics where BP's optical anisotropy could lead to more efficient systems.

Despite its promising properties of 2D materials, there are still some, one of the main challenges is the structural degradation of some atomically thin 2D layers in ambient conditions, which can lead to

decreased performance and reliability of devices that use these materials. This degradation can be caused by a variety of factors such as exposure to oxygen, moisture, and temperature fluctuations. Therefore, developing robust encapsulation techniques and optimizing device fabrication processes are critical for ensuring long-term stability of 2D materials-based devices. Another challenge is the limited scalability of the current synthesis methods for 2D materials, which often rely on micromechanical exfoliation of bulk crystals. This limits the size of the crystals to a few micrometers and makes it difficult to produce large-area films that are uniform and defect-free. Developing scalable and cost-effective synthesis methods for 2D materials is therefore crucial for enabling their widespread commercial adoption. In addition, integrating 2D materials into existing device architectures can be challenging due to the differences in their physical and electronic properties compared to traditional semiconductors. This can require significant modifications to device design and fabrication processes, which may increase the complexity and cost of production. Finally, the lack of standardization in the characterization and measurement of 2D materials poses a challenge for comparing results across different research groups and establishing reliable performance metrics. Developing standardized protocols for the synthesis, characterization, and performance evaluation of 2D materials is important for advancing the field and enabling broader collaboration and commercialization efforts [43], [44].

1.3 Strain Engineering

Strain engineering has become a widely used technique to modify the physical properties of materials by applying external mechanical strain to them. This technique has been extensively applied to two-dimensional nanomaterials such as graphene, transition metal dichalcogenides (TMDs), and black phosphorus. Two-dimensional nanomaterials have unique mechanical and electronic properties that can be modified using strain engineering techniques. Theoretical calculations have shown that ideal single-crystal graphene can achieve high elastic strains of up to 30%, presenting new opportunities to manipulate the chemical and physical properties of 2D materials through elastic strain engineering [45].

Two-dimensional materials with tunable direct band gaps have gained popularity in the field of optical and optoelectronic devices due to their ability to efficiently absorb, emit, and convert photons. These materials have unique properties such as transparency and flexibility, which make them suitable for emerging applications in wearable electronics and transparent display screens. To further broaden the application fields of 2D materials, various techniques have been developed to modulate their properties, including doping, alloying, inducing defects, forming van der Waals heterostructures, electrostatic regulation, and strain engineering. In 2D nanomaterials, strain engineering is a particularly relevant technique as it can modify both their electronic and mechanical properties. Strain can induce changes in the band structure, carrier mobility, and electronic density of states of 2D materials. It can also alter their mechanical properties such as elasticity, strength, and fracture toughness. Unlike bulk materials, 2D materials can withstand greater elastic strain without fracturing. Moreover, their high sensitivity to strain means even small strains can significantly alter their physical properties. The atomic-scale thickness of 2D materials enables various deformation methods to be designed, both in-plane and out-of-plane, which provides more options for inducing strain. In summary, 2D materials with tunable direct band gaps possess unique properties that make them highly suitable for emerging applications, and strain engineering is a promising technique for modulating their properties and expanding their potential uses.

1.4 Types of Strain Applied to 2D Materials

Two-dimensional materials, such as graphene and transition metal dichalcogenides (TMDs), possess unique properties that make them promise for various technological applications. One way to modify and control their properties is by applying strain to them. There are different types of strain that can be applied to 2D materials, and each type can lead to different effects on the material's properties [46].

A homogeneous uniaxial strain is a type of mechanical strain where a 2D material is uniformly stretched or compressed in one direction. This can be done by growing the material on a substrate with a different

lattice constant or by bending the material. This strain has a significant impact on the electronic, optical, and mechanical properties of 2D materials. It can change the electronic band structure of materials like graphene and transition metal dichalcogenides, leading to a tunable bandgap for optoelectronic applications. Uniaxial strain can also increase the mechanical strength and stiffness of materials like MoS₂. The ability to achieve homogeneous uniaxial strain has led to the development of strain engineering techniques that can be used to tune the properties of 2D materials for various applications, such as modulating the optical properties of WS₂ monolayers for nanophotonic devices.

Homogeneous biaxial strain is when a 2D material is uniformly stretched or compressed in two perpendicular directions, which can be achieved through mechanical methods such as placing the material on a substrate with a different thermal expansion coefficient. This strain can significantly impact the mechanical and electronic properties of 2D materials. For instance, studies have shown that applying homogeneous biaxial strain to graphene can increase its strength and stiffness by up to 33% and 22%, respectively. Similarly, applying biaxial strain to molybdenum disulfide can alter its electronic band structure, resulting in a tunable bandgap. However, the effect of strain on electronic properties is highly dependent on the direction and magnitude of the strain. For example, applying a tensile strain along the armchair direction of MoS₂ can lead to a larger increase in the bandgap compared to applying the same strain along the zigzag direction. The direction and magnitude of the strain also play a crucial role in its impact on the electronic properties of 2D materials.

Inhomogeneous local strain is a type of strain that can be applied to 2D materials through non-uniform stress or strain across its surface. This strain can be generated by using various mechanical methods such as atomic force microscopy or nanoindentation. Studies show that inhomogeneous local strain can significantly impact the mechanical and electronic properties of 2D materials. For example, research investigated the effect of this strain on black phosphorus and found that it can alter the electronic band structure. Similarly, inhomogeneous local strain on graphene can induce defects and wrinkles, which increase its stiffness and strength. These studies demonstrate the

potential of inhomogeneous local strain as a tool for manipulating the properties of 2D materials at the nanoscale. Researchers can use various mechanical methods to generate non-uniform stress or strain and further investigate the impact of this strain on the properties of 2D materials.

1.5 Strain Induction Techniques in 2D Materials

Inducing strain in 2D materials is an important research area that has the potential to revolutionize the field of materials science. By applying controlled mechanical strain to 2D materials, researchers can alter their electronic and mechanical properties, which can lead to improved performance and new applications. Various methods, including mechanical stretching, thermal expansion, and chemical doping, have been developed to induce strain in 2D materials, and understanding these methods and their implications is critical to developing future technological applications. By exploring different methods to induce strain in 2D materials, their advantages and limitations, and their potential applications in various fields, researchers can develop novel materials with tailored properties for a wide range of applications. Therefore, research in strain engineering of 2D materials is of great importance for advancing materials science and technology. The researchers have developed numerous methods to introduce strain in 2D materials to address technical difficulties. Figure 1.7 depicts how the uniformity of strain induced in 2D materials has improved over the year. There are two main categories of strain applied to 2D nanomaterials: intrinsic strain and artificial strain. Intrinsic strain can exist in both planar and buckled 2D nanomaterials [47]. Artificial strain engineering has been successfully applied to diverse 2D materials for improved performance in various reactions [48].

Intrinsic strain methods refer to the techniques used to induce strain in 2D materials without the application of external force. These methods includes thermal expansion, which refers to the phenomenon where two materials expand or contract at different rates when exposed to changes in temperature. This can create strain and deformation in the materials when they are bonded together, especially when one material is constrained by the other. In the context of 2D materials, the selection of a substrate with a different thermal expansion coefficient than 2D

materials can create strain in the 2D materials during the chemical vapor deposition (CVD) or epitaxial growth process, due to the mismatched expansion and contraction rates.

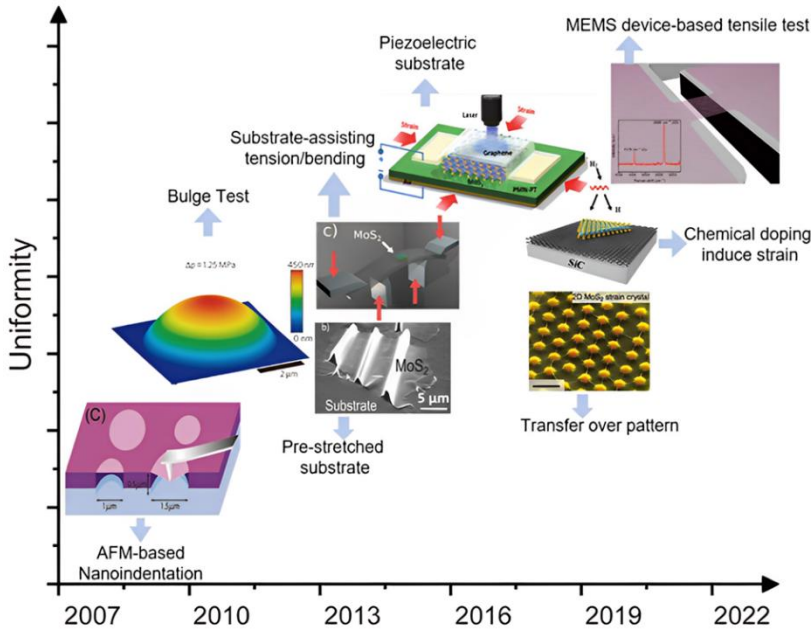


Figure. 1.7: The historical development of strain-based mechanical characterization approaches for 2D nanomaterials [49].

This strain can be either tensile or compressive, depending on the deformation of the substrate, and recent studies show that using flexible substrates with high Young's modulus can effectively induce more strain in 2D materials. Polymer substrates with a high thermal expansion coefficient can induce tensile strain in 2D materials, while those with unique mechanical properties, such as PS, can induce compressive strain. The induced strain can be controlled by adjusting the temperature of the substrate. However, the induced strain may slowly release over time or with a decrease in temperature, which is a challenge that needs to be addressed.

In the semiconductor industry, strain is induced in single crystal materials during epitaxial growth due to the lattice mismatch between the material and the substrate. This method can also be used to induce strain in 2D materials that have an atomic thickness. When two

components of a 2D heterojunction or 2D material and substrate have different lattice constants, it results in either tensile or compressive strain in the 2D material. Lateral heterojunctions are made of two types of 2D materials with similar crystal structures, but different lattice constants have been widely studied. This creates a large strain at the line interface. Researchers grew a monolayer WSe₂-MoS₂ lateral heterojunction using the two-step epitaxial growth method and discovered both tensile and compressive strain in the epitaxial MoS₂ region through PL measurements. Further investigation of the strain distributions caused by lattice mismatch was conducted by imaging the MoS₂ region of in-plane WSe₂-MoS₂ heterojunctions using STM. By analysing the moiré pattern, researchers considered the 2D strain tensor of the central lattice point to be $\epsilon_{aa} = 1.17\%$, $\epsilon_{bb} = -0.26\%$, and $\epsilon_{ab} = \epsilon_{ba} = 0.69\%$, respectively. STEM images showed two types of dislocations at the interface of WSe₂-MoS₂ lateral heterojunctions, resulting in partial relief of strain and then anisotropic strain.

Strain can be induced in 2D materials by transferring them onto patterned substrates. Techniques such as ion-beam sputtering, photolithography, electron-beam etching, and nano self-assembly can be used to modify the surface of rigid substrates and create unique periodic ripple, nanocone, or nanopillar structures. Successful examples include MoS₂ and graphene, where transferring them onto patterned substrates induced local strain. For example, MoS₂ nanosheets were transferred onto a rippled SiO₂/Si substrate, inducing local strain in the obtained MoS₂ ripples. MoS₂ nanosheets transferred onto a patterned Si substrate with Cr hard mask arrays induced tensile strain ranging from 3.46 to 3.65%. Hybrid heterojunctions of nanopatterned substrates and 2D materials can also induce periodic strain. For instance, ZnO nanorod arrays were used to pattern single-crystal ZnO substrates by hydrothermal synthesis, and then monolayer MoS₂ was transferred onto the patterned ZnO substrate, resulting in the formation of organized MoS₂ wrinkles.

The difference in elastic modulus between 2D materials and flexible substrates can cause strain in 2D materials by creating wrinkles. The flexible PDMS substrate is commonly used in this process. The 2D materials are transferred to the pre-stretched PDMS substrate and then released, which induces periodic wrinkles due to differences in elastic

modulus and recovery ability between the materials. If pre-strain is applied in both x and y directions, the release of the pre-strain leads to the formation of 3D wrinkles, which improve light absorption and the performance of optoelectronic devices. Wrinkles also form when 2D materials are transferred to the top surface of a pre-bent PDMS substrate and released to yield uniaxial compression strain. The pre-strain ε_{pre} is defined as follows [46]:

$$\varepsilon_{pre} = \frac{\Delta L}{L} \times 100\% \quad (1.1)$$

where L and ΔL are the initial and stretched lengths of the PDMS substrate, respectively. The induced maximum strain ε on the top of wrinkles can be calculated by the following formula:

$$\varepsilon = \pi^2 h \delta (1 - \sigma^2) \lambda^2 \quad (1.2)$$

where h and σ are the thickness and Poisson's ratio of 2D materials, and δ and λ are the height and width of periodic wrinkles, which can be extracted from the atomic force microscopy (AFM) or the scanning electron microscopy (SEM) image. However, the generation of wrinkles in 2D materials is relatively random and difficult to control. Wrinkles in monolayer or bilayer 2D materials may collapse easily due to their low stiffness, while multilayer 2D materials tend to form stable wrinkles. The strain induced by the pretrained flexible substrates is inhomogeneous, with the largest strain at the top of the wrinkle, usually ranging from 1-2%.

Artificial Strain

The remarkable properties of intrinsic strain in 2D materials have led to numerous efforts to intentionally induce and precisely control strain in these materials. The mechanical methods entail applying external forces to the 2D materials to induce strain, whereas the chemical methods are intended to modify the local lattice structure and introduce strain through mechanisms.

Mechanical Methods

Mechanical methods are techniques that involve physically deforming or bending the 2D material to introduce strain. These methods are often referred to as external or applied strain. There are several mechanical methods to introduce strain in 2D materials, including:

Bulge Test

The bulge test has been a widely adopted method for evaluating mechanical properties of thin film membranes over the last 50 years. Beams et al. were among the first to use this technique to measure the mechanical properties of thin films by calculating the stress and strain in the bulged film. To do this, they assumed a spherical cap with t representing the thickness of the thin film, R denoting the bulge radius of the spherical curvature, P representing the applied pressure difference, and σ and ϵ representing the stress and strain, respectively. The calculation is expressed as follows [50]:

$$\sigma = \frac{PR}{2t} \quad (1.3)$$

in the spherical cap, the spherical curvature R can be replaced by bulge height z , and the film radius a if $z \ll a$:

$$R = \frac{a^2}{2z} \quad (1.4)$$

The bulge test is a widely used method for measuring the mechanical properties of thin film materials. Figure 1.8 shows a pressurized bubble device commonly used. In a single experiment of bulge test, can provide valuable information about different mechanical properties of the thin film on the substrate, including elastic modulus, residual stress, and adhesion to the substrate.

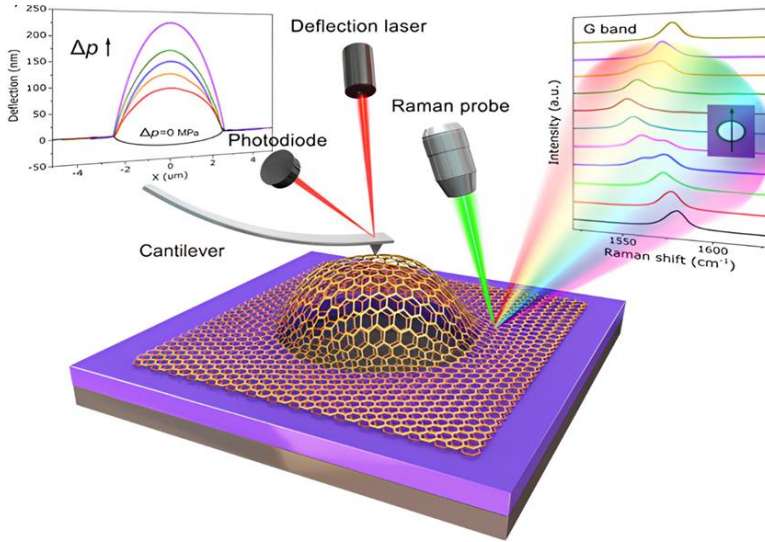


Figure. 1.8: The diagram depicts a bulging test for bilayer graphene. The left inset illustrates the profiles of a graphene bubble under increasing pressure. On the right inset, Raman spectra of a graphene G band are displayed vertically in the direction of a line scan [51].

The bulge test is a useful technique for characterizing the mechanical properties of 2D materials, such as graphene and MoS₂, due to their gas impermeability. To conduct the test, 2D materials are typically exfoliated from bulk materials onto a SiO₂/Si substrate with patterned holes, and then a gas diffusion procedure is used to apply a uniform pressure difference across the material, causing it to bulge upwards. The bulge test measures the deflection and blister radius of the material under a certain pressure difference. Hencky's solution can be used to obtain the following equations to analyze the test results [52]

$$\Delta P = K(v) \frac{E t h^3}{a^4} \quad (1.5)$$

The pressure difference, ΔP , the thickness of the 2D material, t , and Young's modulus of 2D materials, E , as well as coefficients $K(v)$ is dependent on Poisson's ratio (v), are all significant factors in the bulge test. By using AFM to measure the values of h and a , the Young's modulus of 2D materials, E , can be determined by fitting the curve of $\Delta P - K(v) \frac{t h^3}{a^4}$, with the assumption that delamination does not occur. Monolayer and multilayer graphene, h-BN, and MoS₂ with layer

numbers ranging from 10 to 70 have been studied for their bending rigidity and Young's modulus [53]–[56].

The Bulge device has been demonstrated to be an effective method for strain engineering of 2D materials. By applying mechanical deformation to a localized region of the material, biaxial strain can be introduced, with maximum achievable strains of up to 5% observed in the center of bulged MoS₂. Additionally, the device allows for the continuous and reversible tuning of the optical band gap, providing a controlled means for modulating the optical properties of the material. This technique has the potential to optimize and tune the properties of 2D materials for various applications in electronics, optoelectronics, and photonics. It is important to note that the Bulge device may not be suitable for inducing large amounts of strain, as it operates on the principle of inducing mechanical deformation on a localized region of the material, which limits the overall amount of strain that can be applied. The device also requires a sophisticated experimental setup and is time-consuming, which may hinder its practicality for large-scale applications.

Despite these limitations, the bulge device remains a valuable tool for understanding the fundamental properties of 2D materials and strain engineering. By providing a means for precise and controlled modulation of the mechanical and optical properties of these materials, it enables the development of advanced technologies such as flexible electronics and photonics. Further research in this area may involve integrating the Bulge device with other strain engineering techniques to achieve even greater levels of strain and explore new material properties.

Bending of a Flexible Substrate

The bending test is a useful method for applying a controlled uniaxial tensile strain to 2D materials. To do this, the 2D material is first deposited onto a flexible substrate through mechanical exfoliation or vapor transport growth film transfer. By bending the flexible substrate, the top surface of the 2D material is stretched, effectively transferring a uniaxial tensile strain to it. The flexible substrate can be bent using a micrometer stage with a two-point, three-point, or four-point bending

geometry [57]. To determine the strain resulting from the bending, a continuum mechanics model for elastic beams is used, under the assumption that the radius of curvature resulting from the bending is larger than the substrate thickness. This is illustrated in Figure 1.9 (a-b). Additionally, the beam's deformation must occur dominantly in the longitudinal direction, while shear stresses and stresses normal to the neutral axis are considered negligible. By taking these factors into account, the strain can be calculated as described in reference [58]:

$$\varepsilon = \frac{h}{2R} \quad (1.6)$$

The van der Waals interaction between the 2D material and the surface of the flexible substrate is strong enough to prevent slipping of the nanosheet for strain levels up to 1%. However, at higher strain levels, the sheets tend to slip, making it difficult to obtain reproducible results. To overcome this issue, metal strips can be evaporated onto the nanosheets to serve as clamping points. This method has been effectively used to apply strain to graphene and study changes in its Raman vibrational modes. The maximum achievable uniaxial strain reported using this technique varies from 0.5% to 2.5%, depending on the specific experimental conditions [59].

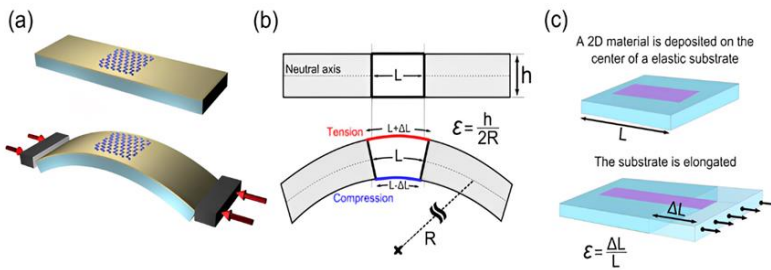


Figure. 1.9: Uniaxial Straining of 2D Materials using Bending and Tensile Test Geometries. (a) Schematic representation of a flexible substrate with a 2D material deposited on it. The two-point bending test geometry enables controlled uniaxial tensile strain to be applied to the 2D material by bending the substrate. (b) Cross-sectional illustration of the flexible substrate before and after bending. (c) Illustration of the method for applying uniaxial tensile strain through elongation of an elastic substrate [60].

Elongating the Substrate

Another technique for studying the mechanical properties and strain engineering of 2D materials involves elongating the substrate on which the material is deposited, as shown in Figure 1.9 (c). This method allows for the application of homogeneous uniaxial tensile strain to the 2D material. To use this technique, the 2D material is deposited onto an elastic substrate, such as a thin polymer film. The substrate is then mounted onto a straining stage, which allows for controlled elongation of the substrate. The straining stage is typically similar to the ones used in material science for tensile tests, with clamps or grips to hold the sample and an actuator to apply the strain. By elongating the substrate, the 2D material is subjected to uniaxial tensile strain, which can be measured using techniques such as Raman spectroscopy or optical microscopy. This allows researchers to study the mechanical properties of the material under controlled strain conditions. Recently, this technique was used to apply uniaxial tensile strain to monolayer WS_2 , a 2D material with potential applications in electronics and optoelectronics. The strain was applied up to 4.0%, allowing researchers to study the material's response to high levels of strain [60]. Substrate-based tension and bending techniques have become a popular choice for demonstrating the effect of strain engineering on two-dimensional (2D) materials, mainly because of their straightforward setup and ease of operation. Previous research mentioned in [46], have utilized these techniques to investigate the strain effect on 2D materials. In particular, under substrate-induced strain, the absorption and photoluminescence (PL) peaks of monolayer MoS_2 can experience significant redshifts. For instance, Conley et al. (2013) have validated that the transition from direct-to-indirect bandgap occurs at a strain of 1%, as confirmed by PL measurements [61].

However, it is important to note that these methods are limited in their ability to achieve high levels of strain compared bulge device, but it is relatively simple and easy to perform but not suitable for studying more complex deformation mechanisms.

Deformation by Indentation

To deform a 2D material using an AFM probe, a monolayer or few-layer 2D material is suspended on a flexible substrate and fixed firmly, shown in Figure 1.10. The deformation of the substrate can be transferred to the attached 2D material through van der Waals force between them when atomically thin materials are placed on flexible substrates. This method is commonly used to apply artificial strain to 2D materials. Another way to generate strain is by mechanically deforming a suspended 2D material using an AFM tip. The deformation of the sample is detected by the deflection of the cantilever, which is measured by a laser beam reflected off the cantilever. The force-indentation depth relationship is then used to calculate the mechanical properties of the material, such as its stiffness, elasticity, and hardness. This technique is capable of achieving atomic resolution and can identify monatomic steps and ripples in the z -direction, resolve lattice orientation, and surface defects in the xy -plane. The tip, which provides high resolution and interacts with the sample surface, is at the end of the cantilever and measures in nanometers [62].

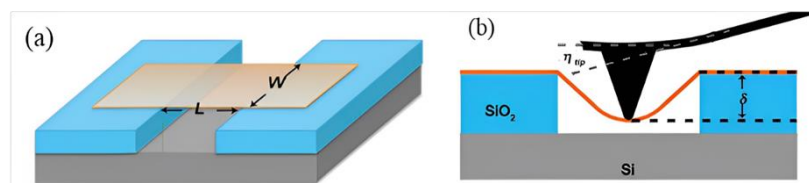


Figure. 1.10. AFM-based methods for determining the elastic properties of 2D materials, a) 2D materials on prepatterned trenches. b) Illustration for the indentation test carried out on a freely suspended 2D sheet with an AFM tip [62].

Several studies have examined the AFM nanoindentation of different 2D materials, including single-layer graphene. AFM nanoindentation was used to determine the mechanical properties of graphene, such as the Young's modulus, strength, and fracture strain, resulting in values of 1 TPa, 130 GPa, and 25%, respectively. Defects were found to significantly decrease both the elastic modulus and strength of graphene. However, the stiffness and strength of polycrystalline graphene were unaffected by the presence of grain boundaries. AFM nanoindentation has also been used to study other 2D materials, such as

graphene oxide monolayers and membranes, revealing Young's moduli of 384 ± 31 GPa and ductile behavior, respectively. Another study examined suspended graphene membranes over circular wells, which exhibited high mechanical strength and stiffness, with an average elastic modulus of 1.1 TPa and a fracture strain of up to 25% [63], [64]. Figure 1.11 showcases different images and representations of graphene membranes with circular holes of various sizes. The figure comprises four images, where A is a scanning electron micrograph of a large graphene flake with partial coverage, full coverage, and fractured indentation of a hole. B represents a noncontact mode atomic force microscopy image of a single membrane with a height profile indicated by a solid blue line. C displays a schematic representation of nanoindentation on suspended graphene membranes, while D shows an AFM image of a fractured graphene membrane. These images provide valuable information about the structural properties and behavior of graphene membranes, which can be significant for various applications such as electronics and energy storage.

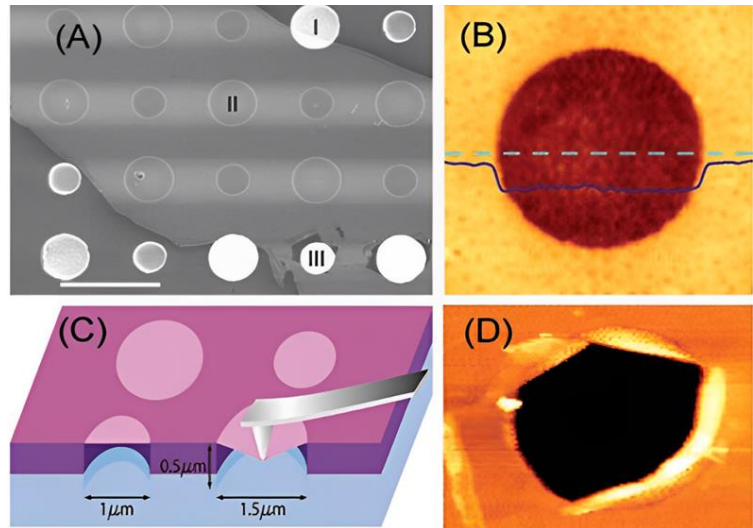


Figure. 1.11: Characterization of Graphene Membranes with Circular Holes Using AFM and Fracture Analysis [64].

The force-displacement data was used in this method to determine the elastic properties and breaking stress of graphene membranes. The elastic response was found to be nonlinear, with a maximum point

defining the intrinsic breaking stress. An elastic response indicates the presence of an energy potential that depends on strain and can be expressed as a Taylor series. The symmetric second Piola-Kirchhoff stress, uniaxial Lagrangian strain, Young's modulus (E), and third-order elastic modulus (D) were used to express the isotropic elastic response under uniaxial extension:

$$\sigma = E\varepsilon + D\varepsilon^2 \quad (1.7)$$

If d is negative, it is causing a decrease in stiffness at high tensile strains and an increase in stiffness at high compressive strains. The value E can be determined from the second-order fourth-rank stiffness tensor, while D is determined from both the second-order fourth-rank stiffness tensor and the third-order sixth-rank stiffness tensor. Nonlinear elastic responses were appropriate for simulations of graphene sheets and nanotubes. The elastic behavior of graphene can be accurately described using a thermodynamically rigorous nonlinear form that captures all important aspects. The intrinsic stress of graphene is the maximum of its elastic stress-strain response and can be expressed as stress:

$$(\sigma) = -\left(\frac{E^2}{4D}\right) \text{ at the strain } (\varepsilon) = -\left(\frac{E}{2D}\right) \quad (1.8)$$

The values of E and D , which represent the material's Young's modulus and bending stiffness, respectively, can be determined through experimental data. By analyzing the force-displacement data, can determine E , while the value of D was inferred from the breaking force [64].

Micro and Nano-Mechanical Devices

Microelectromechanical systems (MEMS) devices have shown great potential in inducing uniaxial strains in two-dimensional (2D) materials and studying their mechanical response. The tensile test, which is the most fundamental mechanical test for determining the mechanical properties of materials, can be used to control the bandgap, conductivity, and optical properties of 2D materials, with potential applications in various fields such as electronics, photonics, and energy

storage. Micromechanical device-based tensile tests offer the advantage of testing small samples with high precision, enabling a detailed understanding of the mechanical properties of 2D materials. MEMS-based platforms have been successfully used to perform tensile tests on various 2D materials, such as graphene, molybdenum disulfide (MoS₂), and black phosphorus (BP), determining their mechanical properties such as ultimate tensile strength, maximum strain, breaking strength, and Poisson's ratio. These findings are crucial for developing devices with improved mechanical performance, including flexible electronics and sensors, which are increasingly being developed with 2D materials. In a study by H. Hugo Perez et al. in 2014 [65], researchers investigated the mechanical response of multilayer graphene using MEMS devices. They induced uniaxial strains using the MEMS devices, monitoring the mechanical response with Raman spectroscopy. The results showed that the MEMS devices were effective in inducing strains and monitoring the mechanical response, demonstrating their ability to evaluate the mechanical response of 2D materials. Microforce sensors and micro-displacement sensors are used to measure the applied force and resulting displacement with high accuracy. The loading-displacement (L-D) curve obtained from MEMS devices provides valuable information about the mechanical behavior of 2D materials. From the L-D curve, the mechanical properties of the 2D material can be determined, including its Young's modulus, ultimate tensile strength, maximum strain, breaking strength, and Poisson's ratio. These properties are crucial for designing and developing advanced devices that utilize 2D materials, such as flexible electronics and sensors. Young's modulus measures the stiffness of a material and can be calculated using the following equation for 2D materials under the assumption of linear elasticity [65]:

$$E = \frac{L \times l}{w \times t \times \Delta D} \quad (1.9)$$

Where E is the Young's modulus, L is the length of the 2D material, W is its width, t is its thickness, and ΔD is the displacement of the sample. By analyzing the L-D curve obtained from MEMS devices, researchers can also determine other mechanical properties of 2D materials, such as the ultimate tensile strength, maximum strain, breaking strength, and Poisson's ratio. These properties are crucial for designing and

developing advanced devices that utilize 2D materials, such as flexible electronics and sensors.

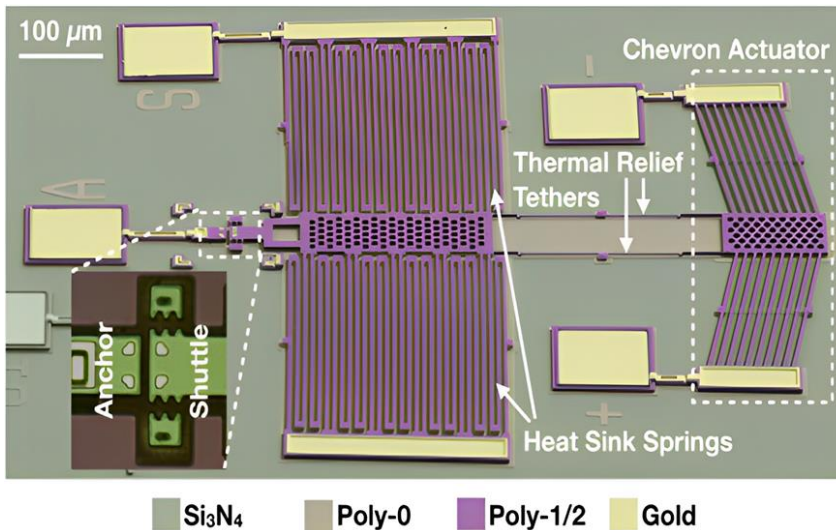


Figure. 1.12: MEMS device used for straining 2D materials [66].

Several research studies have investigated the use of micro-electromechanical systems (MEMS) devices to accurately measure the elastic properties and fracture behaviors of 2D materials. These studies are discussed in the literature [49], [63], [65]–[68]. The MEMS devices used for this purpose are known as in-plane tensile devices, which employ a thermally actuated shuttle to apply tensile strain and a fixed load shuttle to calibrate springs for direct measurement of the stress-strain curve. Figures 1.12 and 1.14 depict the MEMS-based in-plane tensile device and its working principle, respectively, providing a visual representation of the device and its functionality. This enables a better understanding of the experimental setup used to measure the mechanical properties of the sample. The stress-strain curve generated from this device is a crucial tool for gaining insights into the mechanical behavior of the material under tension, allowing researchers to accurately determine its tensile strength, Young's modulus, and ductility.

Other studies have employed a nanomechanical device in a SEM to investigate the fracture behavior of graphene and MoSe₂. This method

involves the transfer of suspended 2D materials onto testing stages and the use of FIB patterning to create a rectangular shape for further testing. By utilizing the "push-to-pull" mechanism, the force exerted on the beam by the indenter is transferred to the tension of the stage, enabling in-plane tensile tests of 2D materials to be carried out [65], [67]. Figure 1.13 showcases a few examples of devices used for in-plane tensile testing of graphene and MoSe₂. These MEMS devices offer a high degree of precision and control in testing the mechanical properties of 2D materials, which is essential for developing next-generation technologies.

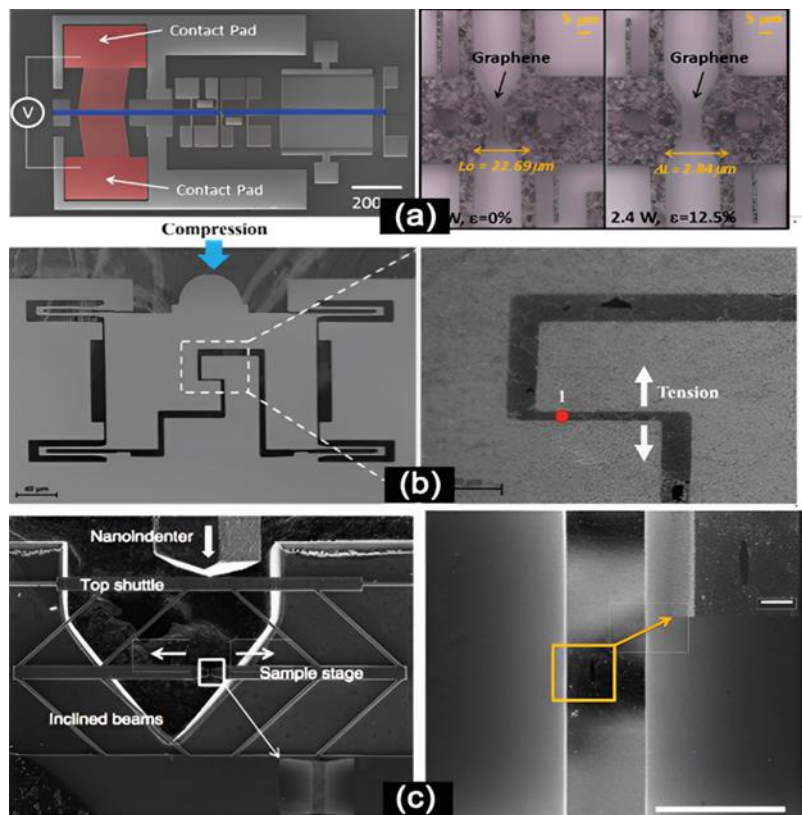


Figure. 1.13: Micro-Electro-Mechanical System (MEMS) Devices for Measuring the Mechanical Properties of 2D Materials: (a) In-Plane Tensile Testing Stage with Thermal Actuation and Strain Measurement of Graphene, and SEM Images of (b) Graphene and (c) MoSe₂ Using "Push-to-Pull" Devices for In-Plane Tensile Testing [65].

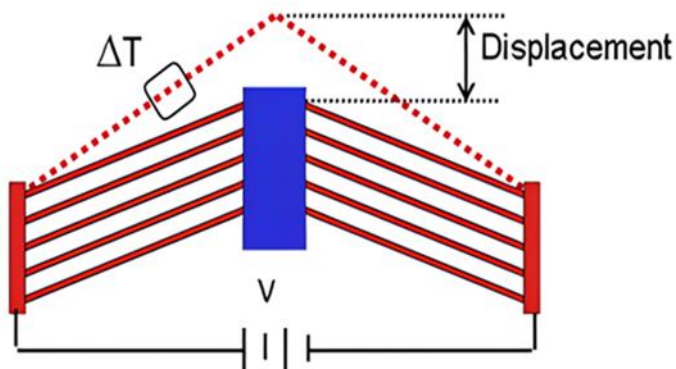
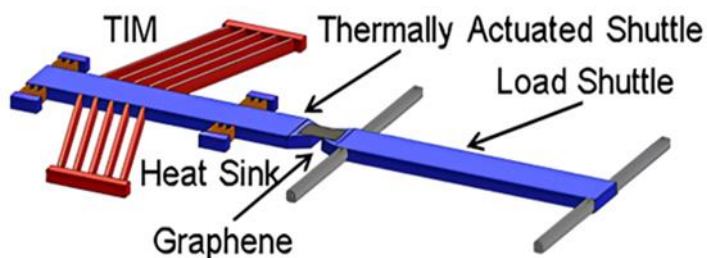


Figure. 1.14: A schematic is shown, depicting the main components and working principle of the Thermal in-plane microactuator [63].

In order to study the mechanical properties of 2D materials, researchers often use MEMS technology, which involves micromechanical devices. These devices can apply precise uniaxial tensile strains to the materials and allow for high magnification imaging to observe their behavior in real-time (Figure 1.14). By using these devices, researchers can gain important insights into the mechanical behavior of 2D materials, which is crucial for developing advanced materials with better mechanical performance, like flexible electronics and sensors. MEMS technology has become a promising technique for studying the mechanical properties of 2D nanomaterials.

Despite the promise of strain engineering for modifying the properties of 2D nanomaterials, there are several challenges that need to be

addressed. One challenge is to develop reliable devices for inducing and measuring strain at the nanoscale, particularly in complex heterostructures. Another challenge is to understand how strain affects the stability and reliability of 2D nanomaterials, particularly in harsh environments.

There are several aspects to the future of MEMS-based tensile testing of 2D materials. Firstly, the development of more advanced and precise devices for studying the mechanical behavior of these materials. For example, the use of MEMS-based devices in combination with other techniques could provide a more complete understanding of the mechanical properties of 2D materials under different types of strain. Secondly, the development of new 2D materials and their incorporation into MEMS devices could open up new opportunities for exploring their unique mechanical properties and potential applications in various fields. Thirdly, the use of MEMS-based devices for in-situ testing of 2D materials under different environmental conditions, such as temperature and humidity, could provide insights into their behavior under real-world conditions. Finally, the integration of MEMS-based devices with other types of sensors, such as chemical and biological sensors, could lead to the development of new types of smart materials and devices for various applications.

1.6 Experimental Techniques of Studying Mechanical Properties in 2D Materials

Investigating the mechanical behavior of 2D nanomaterials is challenging due to their size limitations. Various mechanical characterization strategies, such as measuring properties like strength, stiffness, ductility, and adhesion, have been employed to study their behavior. Traditional observation under a microscope is used to understand qualitative information about deformation mechanisms and failure characteristics. Two main methods, theoretical simulations and experimental techniques, are used to investigate their mechanical properties. However, measuring their mechanical properties is challenging due to their small size and fragile nature. In situ microscopy techniques, such as SEM, TEM, and AFM, are particularly advantageous in investigating the mechanical properties of 2D

materials, from basic behaviors to atomic-level mechanisms. These techniques are versatile and can reveal novel physical phenomena of nanomaterials, allowing investigation of various properties such as electrical, thermal, optical, mechanical, chemical, electromechanical, electrochemical, and mechanochemical properties of nanomaterials. Typically, 2D nanomaterials are single-layer materials consisting of atomic monolayers, making their thickness extremely fine (\AA -nm length scale). In-situ testing in high-resolution microscopes is an effective approach to assess their mechanical response, as mechanical properties can be highly sensitive to material and environmental temperatures.

1.6.1 In Situ Microscope Techniques

In the late 1950s, scientists developed in situ straining stages for electron microscopes, which allowed them to observe the dynamic movement of dislocations in metals. While electron microscopy is a useful tool for investigating the mechanical properties of materials, especially for imaging individual defects in heterogeneous materials, the complex nature of defective structures makes it difficult to connect high-resolution observations to multiscale deformation phenomena. As a result, a multiscale analysis of materials is required to fully understand how they respond to stress. In situ nanomechanical testing offers a way to examine microstructural changes in a controlled manner by applying specific loading geometries and environmental conditions while also enabling sensitive measurements. The various in situ microscopy techniques available, such as atomic force microscopy (AFM), friction force microscopy (FFM), scanning tunneling microscopy (STM), scanning electron microscopy (SEM), and transmission electron microscopy (TEM), have the advantage of intuitively revealing the actual mechanical properties and deformation behavior of materials. These techniques have been widely used to measure and characterize the mechanical properties and deformation behavior of various nanomaterials, including superplastic and ultrahigh strength metallic, semiconducting, and ceramic nanoparticles and 3D nanostructures. The experience and knowledge gained from these studies can provide valuable insight for research in the field of 2D materials. In situ microscopy techniques can be used to establish the relationships between the mechanical properties, deformation behavior, and

structures of 2D materials, with each technique having its own unique characteristics and advantages [69].

In situ AFM technique

The AFM technique is commonly used to measure the mechanical properties of 2D nanomaterials, including Young's modulus, breaking strength, and friction coefficient. AFM has three primary modes of operation: contact, tapping, and noncontact mode. Static AFM deflection method is used to measure the deflection of an AFM cantilever in contact with a sample surface, which can be used to determine the mechanical properties of the material.

AFM-based mechanical testing is used to measure the elastic modulus and fracture strength of 2D materials, starting with graphene. Calibrated AFM tips are used to extract the Young's modulus. AFM and Raman spectroscopy are used to precisely measure the width, length, and thickness of 2D materials, which are usually under tension. After measuring the dimensions, the AFM tip is slowly pushed down in the center of the membrane, while recording the tip deflection (η_{tip}) and the position of the piezoelectric tube (z_{piezo}) moving the tip. The spring constant (k) of the AFM tip is used to calculate the relationship between the force applied by the tip ($F = K \times \eta_{tip}$) and the displacement of the 2D sheet (δ). The displacement can be calculated using the following equation [69]:

$$z_{piezo} = \eta_{tip} + \delta \quad (1.10)$$

To determine the Young's modulus (E) of 2D materials, the effective spring constant (K_{eff}) can be obtained from the F - δ graph in the linear region where there is small displacement. This is applicable to a doubly clamped beam in equilibrium with a static force applied at the center and under axial tension. By relating K_{eff} and dimensional parameters (W, L, t) according to continuum mechanics, the Young's modulus can be determined using the formula for a beam's stiffness under bending and tension, which takes into account the dimensions of the beam and its material properties. The equation used to determine the Young's modulus is:

$$K_{eff} = 16.233 \times E \times W \times \left(\frac{t}{L}\right)^3 + 4.93 \times \frac{T}{L} \quad (1.11)$$

To determine the Young's modulus (E) of suspended 2D materials, the effective spring constant (K_{eff}) is measured and fitted with the term $W \times \left(\frac{t}{L}\right)^3$. If the lengths (L) of the sheets are similar, the $\left(\frac{T}{L}\right)$ term can be modeled as a constant offset, allowing E to be extracted from the slope. The equation for determining E is given as [70]:

$$E = \frac{K_{eff}}{16.233 W} \left(\frac{L}{t}\right)^3 - \frac{4.93}{16.23} \times \frac{TL^2}{Wt^3} \quad (1.12)$$

However, measuring interfacial properties requires additional sample preparation processes such as creating wrinkles and blisters. Although it is easy to measure mechanical parameters, this technique cannot visually represent crack formation and propagation processes.

In situ SEM Technique

In situ scanning electron microscopy (SEM) is a powerful technique for investigating the mechanical properties of materials at the nanoscale. The scanning electron microscope (SEM) has a spatial resolution of several nanometers and allows for the introduction of various probes, such as optical fiber, electrical measurement, and force sensing probes, to measure multiple properties of nanomaterials within its large sample chamber (Figure 1.15 a). By performing appropriate measurements within the SEM, it is possible to successfully obtain various mechanical properties and behaviors of 2D materials. For example, Researchers applied a tensile load to the graphene sample while simultaneously imaging it using SEM and found that graphene has high strength and stiffness, but also exhibits significant deformation before failure. The use of in-situ SEM allowed for precise measurements of the mechanical properties of graphene, which are crucial for designing graphene-based devices and structures for various applications. The approach used in this study can be applied to measure the mechanical properties of other two-dimensional materials [71].

Molybdenum disulfide (MoS_2) is another two-dimensional material with promising mechanical properties. Researchers used in-situ SEM to

measure the mechanical properties of MoS₂ by applying a compressive load to the sample while imaging it using SEM. The results showed that MoS₂ has high strength and stiffness, but also exhibits significant plastic deformation before failure around 10 GPa. This information is important for designing MoS₂-based devices and structures, such as transistors and sensors. The in-situ SEM technique allowed for real-time observation of the deformation behavior of MoS₂, which can inform future research on this material's mechanical properties [72].

The AFM indentation and microelectromechanical systems (MEMS) device are commonly used to investigate the mechanical properties of 2D materials in situ SEM. The AFM indentation test measures the elastic modulus of the material, while the MEMS device offers controlled actuation, high-resolution force and displacement measurements, and is small enough to fit into the SEM for in-situ testing. These methods are commonly used due to their accuracy and precision in measuring the mechanical properties of materials at the micro and nanoscale. MEMS devices have been explored for advanced nanomechanical testing, such as temperature-controlled testing and high-strain-rate testing [69], [72]–[75].

In several studies, researchers have used in situ scanning electron microscopy (SEM) to investigate the mechanical properties of various 2D materials. Researchers examined the mechanical behavior of molybdenum disulfide (MoS₂) monolayers using a microelectromechanical system (MEMS) device inside the SEM chamber. Real-time measurements of the elastic modulus, yield strength, and ultimate strength of MoS₂ were obtained, and it was found that the elastic modulus of MoS₂ monolayer is lower than its bulk modulus, indicating the effect of dimensionality on the mechanical properties of 2D materials [69]. The literature highlights the promise of utilizing in situ SEM measurements with MEMS devices to investigate the mechanical properties of 2D materials [49], [63], [65], [67], [69], [73]–[77]. The advantage of in situ SEM is its ability to perform real-time observations of the deformation behavior of materials while measuring their mechanical properties. MEMS devices offer controlled actuation, high-resolution force and displacement measurements, and are small enough to fit inside the SEM chamber, making them ideal for in situ testing. These methods have been used to study various 2D

materials, including graphene, molybdenum disulfide, and tungsten disulfide, providing valuable insight into the mechanical properties of these materials and their potential applications.

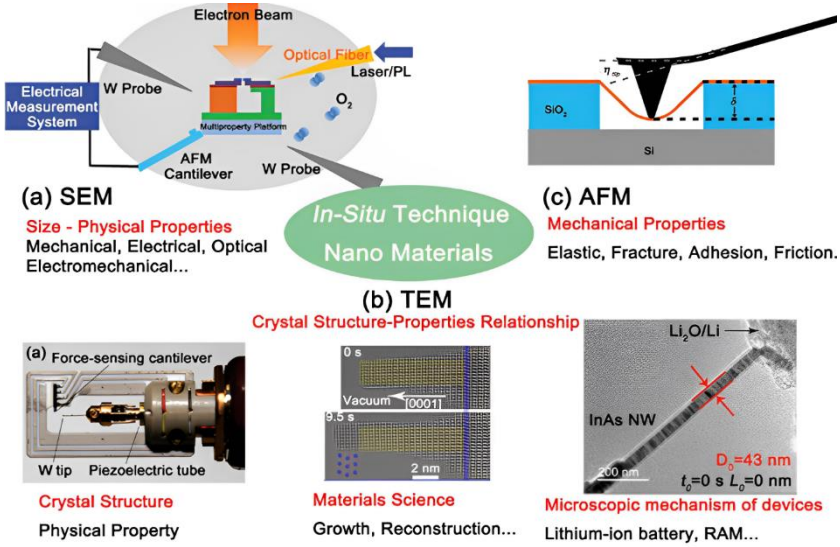


Figure. 1.15. In situ techniques for measuring mechanical properties in 2D materials [69].

Zhang et al. (2014) [78] conducted a study on the mechanical behavior of graphene under increasing tensile load using in-situ tensile testing and real-time SEM imaging. The study employed a pre-crack in the graphene membrane to determine fracture toughness using Griffith's theory. The stress-strain relationship was recorded, and the material's brittle nature allowed for the application of Griffith's theory of brittle fracture to determine the critical stress for fast fracture onset. The experimental setup included a nano indenter and a push-to-pull micromechanical device. The findings provide valuable insights into the mechanical properties of graphene and can inform the development of new materials with tailored properties for specific applications. To determine the fracture toughness, Griffith's theory was used, and equation (1.13) was applied.

$$K_c = \sigma_c \sqrt{\pi a_0} \tag{1.13}$$

The graphene membrane was subjected to tensile loading, and a central crack was observed to gradually grow under increasing load. Real-time SEM imaging allowed for the monitoring of crack growth and deformation behavior during the tensile loading process. Eventually, the loading resulted in the failure or splitting of the graphene into two halves. The study also recorded the quantitative stress-strain relationship, showing a linear response until the fracture point. Since the response was brittle in nature, Griffith's theory of brittle fracture was considered to determine the critical stress for the onset of fast fracture, with a central pre-crack of length $2a_0$. Equation (1.14), which involves Young's modulus and surface energy, was applied for this determination:

$$\sigma_c = \sqrt{\frac{2\gamma E}{\pi a_0}} \quad (1.14)$$

In situ TEM Technique

In situ transmission electron microscopy (TEM) nanomechanical testing is a powerful tool for studying the mechanical properties of 2D materials. It utilizes the sensitivity of TEM to lattice distortion to visualize both elastic and plastic deformation via strain fields from several hundred nanometers down to the atomic-length scale. Advanced imaging and diffraction scanning transmission electron microscopy (STEM) techniques have emerged due to the development of fast detection systems of several hundred frames per second. In situ TEM high-resolution observation provides more detailed information at the atomic scale compared to in situ AFM indentation and in situ SEM tensile testing. In situ TEM tensile testing and high-resolution observation can reveal the in-plane mechanical properties and the mechanism of the nanomechanical behavior of 2D materials. In situ TEM tensile testing is used to measure the fracture strength and toughness of 2D materials. For example, a study on the tensile response of patterned high crystallinity GNRs with a width less than 100 nm was conducted through PTP devices equipped in a TEM system. Another study measured the mechanical properties of carbon-linked GO nanosheets using a TEM-compatible MEMS device. In situ TEM nanomanipulation and observation can easily reveal the nanomechanical behavior in response to an external load, while

structural changes due to phase transitions can also be captured by in situ TEM observation [69].

2D materials have been the focus of considerable attention in recent years, owing to their unique mechanical properties and potential applications. In situ TEM has emerged as a valuable tool for studying the mechanical behavior of these materials. Real-time observation of the material's response to stress has been found to be particularly effective in investigating their deformation and fracture behavior. Furthermore, in situ TEM has been used to study dislocations, deformation twinning, and grain boundary-mediated plasticity in 2D materials, providing valuable insights into their mechanics [79].

The use of in situ TEM was found to be particularly effective in studying the deformation and fracture behavior of 2D materials, as it allowed for the real-time observation of the material's response to stress. Supported by this finding, a study investigated the behavior of dislocations, deformation twinning, and grain boundary-mediated plasticity in 2D materials using in situ TEM. Through this approach, the study was able to obtain valuable insights into the mechanics of these materials, which could inform the development of new materials with enhanced mechanical properties for various applications. These developments have the potential to advance our understanding of 2D materials and inform the development of new materials with enhanced mechanical properties for various applications.

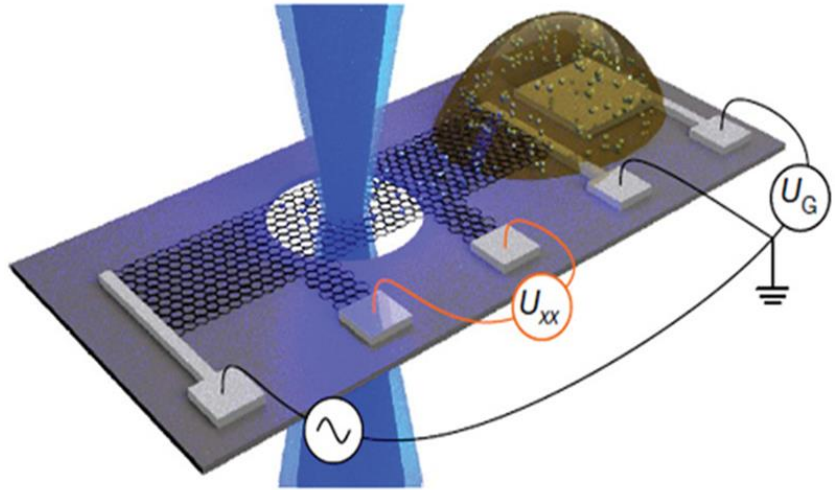


Figure. 1.16: In situ transmission electron microscopy setup [71].

Figure 1.16 depicts a schematic diagram of an in-situ transmission electron microscopy (TEM) device constructed using a bilayer graphene, multielectrode, and a droplet reserve on a silicon nitride covered silicon chip. The device consists of a microfabricated membrane that is composed of a bilayer graphene sheet and suspended over the sample chamber. The multielectrode located on the sides of the membrane is used for applying mechanical loads such as bending and tension to the sample. The droplet reserve is used to encapsulate the sample, which allows for precise control of the environment and minimizes the effects of surface contamination during imaging. The use of graphene in the device not only provides excellent mechanical properties but also enhances the electrical conductivity and sensitivity of the device. This innovative in-situ TEM device has the potential to greatly advance our understanding of the dynamic behavior of materials at the nanoscale.

Scanning Tunneling Microscopy (STM)

Scanning Tunneling Microscopy (STM) is a powerful tool that has revolutionized the field of materials science and nanotechnology. It was first developed in the 1980s and has since been used to image surfaces with atomic resolution and to manipulate individual atoms and

molecules on the surface of a sample [80]. By scanning a sharp metal tip across the surface of a sample at a very close distance (shown in Figure 1.18), STM can create an image of the surface with atomic resolution. One of the most significant advantages of STM is its ability to image surfaces at the atomic scale, providing unprecedented resolution and detail. STM has been used in a wide range of applications, including the study of semiconductors, metals, and biological molecules. It has enabled the discovery of new materials, such as fullerenes and graphene, and has advanced our understanding of the properties of existing materials. Additionally, STM has been used in industrial applications, such as in the fabrication of integrated circuits and the characterization of materials used in electronic devices.

There are several studies exemplify the versatility of STM. In the case of graphene on a BN substrate, for example, in situ STM was used to investigate the local microscopic properties of the graphene and its interaction with the substrate [81]. The study found that the graphene exhibited strong adhesion to the substrate and showed evidence of strain-induced deformations, highlighting the importance of mechanical properties in the graphene-BN system. Similarly, in the review mentioned, in situ STM was used to investigate the electronic properties of graphene, such as its band structure and charge transport properties [82]. This information is crucial for understanding the material's behavior in electronic devices and for developing new graphene-based technologies. Finally, in situ STM has also been used in conjunction with other techniques, such as spectroscopy, to investigate the properties of graphene-based nanocomposites [83]. By combining these techniques, researchers can obtain a more complete picture of the material's properties and how they are affected by the presence of other components.

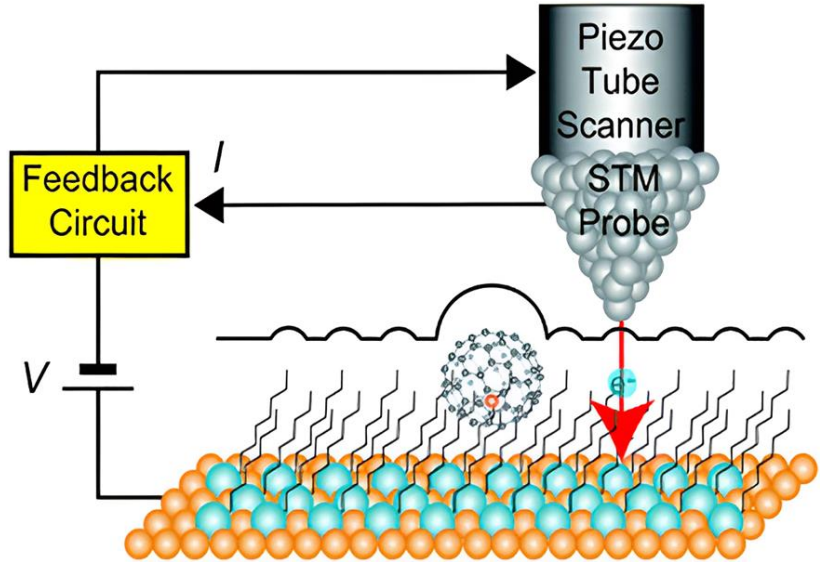


Figure. 1.18: Illustration of scanning Tunneling Microscopy [84].

Low-Temperature Scanning Tunneling Microscope (LT-STM)

The low-temperature scanning tunneling microscope (LT-STM) is a cutting-edge instrument that allows researchers to study materials and surfaces at the nanoscale under controlled low-temperature conditions. This is an extension of the scanning tunneling microscope (STM), which operates at room temperature. The LT-STM operates at extremely low temperatures, typically between 4 and 77 Kelvin (-269 to -196 degrees Celsius), offering several advantages over the STM. One of the most significant advantages of the LT-STM is its ability to achieve higher resolution imaging of surfaces and structures due to reduced thermal vibrations and noise at low temperatures. This enables researchers to study the properties of materials at a higher level of detail. In addition, the LT-STM provides more precise control over the surface properties of the sample being studied, such as its electronic and magnetic properties, due to the controlled environment and low temperatures. The LT-STM is also more sensitive to changes in the electronic and magnetic properties of the sample than the STM, thanks to the lower temperatures that reduce thermal noise, making it easier to detect small changes in electronic and magnetic properties. The low temperatures also enable the study of unique phenomena and behaviors that cannot be observed at room temperature, which is essential for

understanding the properties and behavior of materials at the nanoscale. The LT-STM has become an indispensable tool in the fields of physics, chemistry, materials science, and engineering. It provides a means to study materials at the nanoscale under controlled conditions, advancing our understanding of materials and enabling the development of new materials and technology. The LT-STM is revolutionizing the way researchers investigate materials and surfaces, and its potential applications are vast. With its high resolution and sensitivity, it has the potential to unlock new discoveries and innovations that could transform numerous industries [80].

In a study, a low-temperature scanning tunneling microscope (STM) was used to examine the surfaces of NbN and graphite at a temperature of 6.5 K [85]. The STM is typically operated at 4.2 K but can be cooled down to 1.4 K by pumping the helium bath of the cryostat [86]. The system used in the study had very low spatial drift, with lateral drift less than 2 nm/h and vertical drift less than 0.65 nm/h [85]. Cryogenic temperatures were necessary to obtain high resolution in separating quantized energy level structures [87]. The STM was housed in an ultra-high vacuum (UHV) chamber to avoid contamination of the sample and to allow the use of cryogenic temperatures [88]. The study demonstrates the potential of low-temperature STMs for examining surfaces at the atomic level.

1.6.2 In Situ Integrated Microscopy Techniques

The use of in situ microscopy techniques has been instrumental in studying the mechanical properties and fracture behavior of 2D materials from various perspectives. To achieve a better understanding of these materials, researchers often integrate multiple techniques. In situ atomic force microscopy (AFM) and scanning electron microscopy (SEM), in situ AFM and transmission electron microscopy (TEM), in situ SEM and TEM, and in situ AFM, SEM, and TEM have all been used to investigate the mechanical properties and deformation behavior of 2D materials at different size levels. These integrated techniques allow one microscopy technique to be the primary research method while others serve as supplements, providing high-resolution observation and data collection. In situ microscopy techniques have been used to study the mechanical properties of 2D materials. Many

reviews focus on the use of scanning electron microscopy (SEM), transmission electron microscopy (TEM), and atomic force microscopy (AFM) for this purpose [89]. These techniques have been used to characterize the deformation behavior of 2D materials. These studies demonstrate the usefulness of in situ microscopy techniques for studying the mechanical properties of 2D materials. Figure 1.17 illustrates various in-situ integrated microscopy techniques used for analyzing the nanomechanical properties and behaviors of 2D materials and operational conditions for each technique.

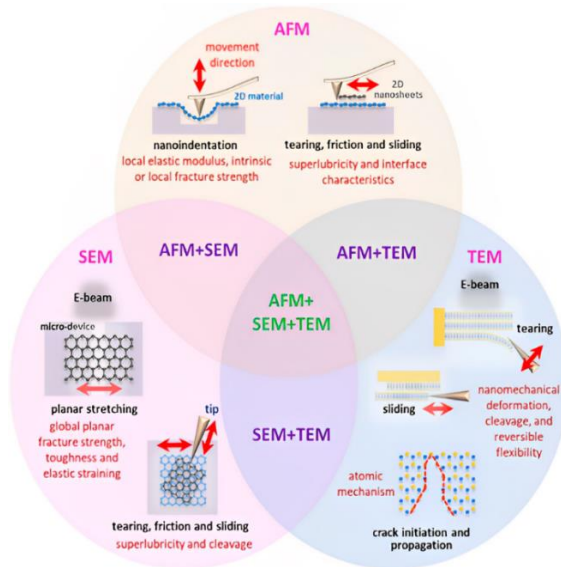


Figure. 1.17: Applications and Diagrams of Different In Situ Microscopy Techniques for Analyzing the Nanomechanical Properties and Behaviors of 2D Materials (the black font indicates the operational behaviors and conditions, while the dark red font represents the properties and behaviors of 2D materials that can be observed and measured by each in situ microscopy technique) [89].

1.7 Challenges and Limitations

The use of an LT-STM has certain limitations and challenges that must be addressed to achieve accurate results. One major challenge is the need to maintain extremely low temperatures throughout the experiment, which can alter the sample or tip properties and requires specialized equipment and careful thermal management. Achieving and maintaining high vacuum conditions is also necessary to minimize

sample contamination, but it can be challenging and require advanced equipment. The high voltage used during imaging can lead to sample damage, particularly if the tip is in contact with the surface for an extended period. Additionally, maintaining a stable temperature throughout the experiment is crucial, as small temperature fluctuations can affect the measurement results.

However, when considering the use of micro-electromechanical systems (MEMS) devices in LT-STM tools, there are also potential gaps to consider. For example, the limited availability of MEMS devices that can withstand the extremely low temperatures required for LT-STM operation can restrict the types of experiments that can be performed. Additionally, the materials used in MEMS devices may exhibit unexpected behavior or become brittle at cryogenic temperatures, which can affect their performance. The integration of MEMS devices into LT-STM tools may also pose challenges in terms of compatibility, alignment, and specialized testing and calibration procedures to ensure accurate and reliable measurements.

Despite these challenges, the use of MEMS devices in LT-STM tools has the potential to offer insight into the mechanical behavior of 2D materials, providing critical information for the design of materials and devices for various applications. MEMS devices have been utilized for advanced nanomechanical testing, such as temperature-controlled testing and high-strain-rate testing. By using specialized knowledge and training, advanced data analysis techniques, and careful equipment maintenance, researchers can effectively utilize LT-STM tools with MEMS devices to advance the understanding of nanoscale materials and their behavior.

This chapter 2 focuses on the development of a novel Microelectromechanical Systems (MEMS)-based testing platform for characterizing the strain engineering of 2D nanomaterials. This platform integrates on-chip actuation, sensing, and feedback control systems, allowing controlled displacements to be applied for the characterization of two-dimensional (2D) materials. It is compatible with various characterization instruments, including Scanning Tunneling Microscopes (STMs), enabling highly accurate displacement measurements. The primary goal in developing this platform was to achieve substantial sample displacements while concurrently minimizing temperature variations within the sample area. This ensures the highest sensitivity in displacement measurement, making it an ideal tool for strain engineering characterization.

2.1 Introduction

In recent years, the mechanical and electronic properties of 2D nanomaterials, such as graphene, have garnered considerable attention due to their potential applications in cutting-edge electronic and optoelectronic devices [90]. However, certain potential gaps in the literature, which could further enhance our understanding of these materials, remain to be addressed. A salient gap lies in the need for a uniform, high strain rate induced in 2D materials. This is essential for improving the reproducibility of experimental results. Additionally, the need for precise and accurate measurements of the strain applied to samples, particularly at low temperatures where thermal fluctuations may impact the accuracy of strain values, is also a critical area that requires further investigation [91]. The advancement of MEMS-based tensile testing platforms, combining on-chip actuation, sensing, and feedback control, is another pivotal need for the characterization of 2D materials in advanced microscopes, such as in-situ microscopes [92]. These platforms can enhance the accuracy and precision of experimental measurements, yielding invaluable information on the mechanical and electronic properties of these materials. Finally, the effects of low temperatures on the mechanical and electronic properties of strained graphene and other 2D materials remain insufficiently understood. Thus, more comprehensive investigations are necessary to better understand these material's behavior at low temperatures and to

facilitate the development of more sophisticated electronic and optoelectronic devices.

There is a need for a comprehensive approach to address these gaps in the literature on 2D nanomaterials is becoming increasingly apparent. The development of novel MEMS-based tensile testing platforms capable of facilitating the characterization of 2D nanomaterials at low temperatures and in advanced microscopes, such as in-situ microscopes, is a priority. By incorporating on-chip actuation, sensing, and feedback control, these platforms can improve the accuracy and precision of experimental measurements, inducing uniform high strain rates to 2D materials. They also ensure accurate and precise measurements of the strain applied to the samples. Such platforms can significantly enhance our understanding of these materials under strain and at low temperatures, setting the stage for the development of advanced electronic and optoelectronic devices with superior performance and efficiency.

2.2 MEMS-Based Tensile Testing Platforms

The study of mechanical properties and failure mechanisms of thin films typically involves tensile tests. Recent years have witnessed numerous studies subjecting nanoscale materials to tensile loading using either 'off-chip' actuators or 'on-chip' Microelectromechanical Systems (MEMS) actuators [74], [93]–[95]. These function within diverse size and scale ranges. Off-chip actuators are commonly employed to test specimens with thicknesses ranging from 400 nm to 1 μm . In contrast, on-chip actuators are applied to specimens in even thinner ranges, such as 75–250 nm. Off-chip actuators, which primarily utilize piezoelectric and form separate test platforms from the test specimen, provide the advantage of simpler setup due to their size. Experiments are generally conducted under an optical microscope. Since the specimen is independent of the actuators, a wide range of specimen materials can be selected. On the other hand, on-chip actuators generally restrict the choice of specimen materials as they are either co-fabricated along with the actuator mounted later using a probe and focused ion beam in a scanning electron microscope. Nonetheless,

on-chip actuators offer benefits such as precise sample alignment and high load and displacement resolution.

MEMS-based tensile testing devices can generally be categorized into four levels of increasing sophistication for characterizing nanomaterials. The first category comprises devices that provide structural support for handling and loading specimens, with external actuation and sensing. The second category integrates force and/or strain sensing, while still requiring external actuation. The third category features on-chip actuation and sensing. The fourth and most advanced category combines on-chip actuation, sensing, and feedback control to enable pure displacement or force-controlled experiments, which is instrumental for characterizing materials in advanced in situ microscopes.

The characterization of 2D material's strain engineering properties requires novel material testing systems capable of delivering micrometer-range displacement. MEMS technology provides the means to develop devices that apply external stress to nanomaterials, estimate their mechanical properties, and characterize fracture or deformation evolution. Two types of MEMS actuators are commonly employed for on-chip tensile testing of nanoscale materials: comb drive actuators and chevron-type thermal actuators. This is due to their easy integration with standard microfabrication processes. Electrostatic actuation is a method frequently utilized in MEMS for tensile testing of micro and nano-scale materials [96]. This method leverages the interaction between electric charges that generate an attractive or repulsive force between two conductive structures. A commonly utilized type of electrostatic actuator is the comb drive mechanism, comprising interdigitated finger structures. While this mechanism has several advantages, it also has significant limitations that require careful consideration when designing and operating MEMS devices for nano-scale material characterization.

In contrast, MEMS thermal actuators, which generate a displacement via the principle of thermal expansion, offer several advantages over other types of MEMS actuators. They are capable of generating larger displacements, operating at higher frequencies, and producing uniform and isotropic stresses. Thermal actuation has proven reliable and

effective for accurately testing material properties, essential for materials development and improvement. To ensure effective and reliable material testing platforms, several design criteria need to be considered. First, an actuator operating at low voltage should be selected, ensuring the temperature at the actuator-specimen interface remains below 100°C to prevent specimen damage. The system should also operate in displacement control, with the actuator's stiffness being considerably higher than the stiffness of the specimen and the sensing system. Furthermore, the thermal actuator must remain stable without buckling within the operational temperature range. The testing system should also be compatible with advanced in situ microscopes to enable accurate observation and measurement of the tested material properties.

2.3 Mechanical Design of the Thermal Actuator

Designing a chevron-type thermal actuator involves considering various physical properties that span electrical, thermal, and mechanical domains. Within this context, numerous geometric parameters can be tuned, such as beam length, cross-sectional area of the beam, beam inclination angle, and the number of parallel beams. Understanding how these parameters affect the actuator's performance is vital for appreciating the necessary trade-offs in the design process. Given the inherently non-linear nature of thermal actuators, precise prediction of their behavior is crucial for detailed model studies [96], [97].

A V-shaped MEMS thermal actuator was designed with the goal of achieving accurate displacement control during specimen testing. The desired displacement and temperature at the sample location were aimed to be approximately 0.8 μm in total and as close to the ambient temperature as feasible. The thermal actuator consists of pairs of stepped beams that connect to a substrate and a central shuttle, as shown in Figure 2.1. These stepped beams are uniquely structured, with thinner regions situated at both ends and a thicker section in the middle. These thinner segments are an essential aspect of the actuator's design because they reduce beam stiffness and permit a wider range of motion. Leveraging these stepped beams and a central shuttle, the thermal actuator can transform thermal energy into mechanical motion. It is crucial to understand the design parameters and their influence on

actuator performance for the creation of an effective and reliable system for material testing.

The performance of an actuator is characterized by two parameters: maximum displacement (d_A) and axial stiffness (k_A). A high k_A value is vital to reduce deformation during testing and ensure most displacement is transferred to the sample. In the absence of a sample, the force acting on the actuator can be expressed as [95], [98]:

$$F = k_A \times U_u \quad (2.1)$$

where k_A denotes the actuator stiffness and U_u represents its undisturbed displacement.

The displacement at the actuator end changes when a sample is connected, which can be expressed as:

$$F = k_A \cdot U_d + k_s \cdot U_d \quad (2.2)$$

where k_A represents the actuator stiffness, k_s signifies the specimen stiffness, and U_d is the displacement at the actuator end where the specimen is connected.

Generally, the displacement at the actuator end changes when a sample is connected. Specifically, based on the two above equations, it can be deduced that:

$$k_A \cdot U_u = k_A \cdot U_d + k_s \cdot U_d \quad (2.3)$$

Thus, by rearranging equation (2.3):

$$\frac{U_d}{U_u} = \frac{1}{1 + \left(\frac{k_s}{k_A}\right)} \quad (2.4)$$

To ensure the thermal actuator displaces the same amount even when a sample is mounted, the ratio $\left(\frac{k_s}{k_A}\right)$ needs to be minimized as much as possible.

Concerning the sample, its stiffness can be assessed as that of a body under tensile load:

$$k_s = \frac{EA}{L} \quad (2.5)$$

where E signifies the Young's modulus, A denotes the transverse area, and L represents the length. For reliable testing across a variety of materials, the actuator stiffness should exceed the sample stiffness (k_s) by at least two orders of magnitude.

To make sure the actuator can fracture various samples, a high maximum displacement is required, while keeping the axial stiffness high. To attain this, two analytical models are formulated that connect the actuator's characteristic parameters (such as thickness, length, width, and the number of V-shaped beams) to these prerequisites. However, due to the structural complexity, the analytical model (according to the procedure outlined in [93]) can only supply an approximate parameter set to steer the design process. Hence, a more accurate final design demands a numerical modeling approach based on Finite Element Method (FEM) analysis.

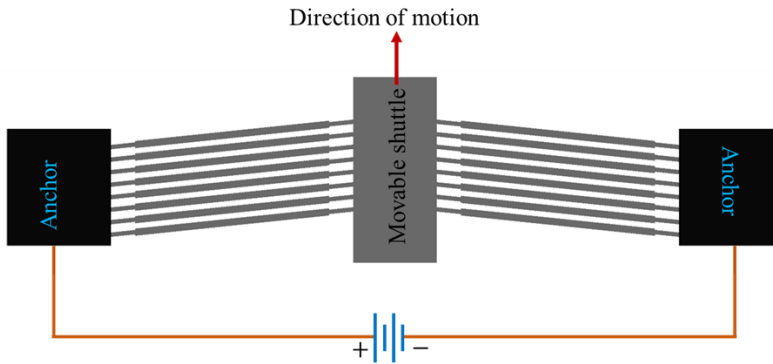


Figure 2.1: Schematic of the thermal actuator

2.4 Analytical Modeling

For precise displacement control in a thermal actuator, it is imperative that the actuator's axial stiffness significantly surpasses the specimen's

stiffness. The impact of the relative magnitudes of the thermal actuator's stiffness (k_A) and the specimen's stiffness (k_S) on displacement (d) is substantial. When the stiffness of the thermal actuator is ten times the specimen's stiffness, the displacement reaches 72% of the displacement (d_0) noted in the absence of a sample. Moreover, when k_A is double k_S , displacement rises to 90% of d_0 .

The axial stiffness of the thermal actuator can be determined using the following equation [99], [100]:

$$k_A = \frac{N \sin^2 \theta \times (w_1 + w_2) E \times t}{L_A} \quad (2.6)$$

Where, N signifies the number of beams, θ denotes the inclination angle of the beams, and w_1 and w_2 represent the widths of the smaller beam and rigid beam regions, respectively. E is the Young's modulus, t is the thickness, and L_A is the total length of the chevron beams.

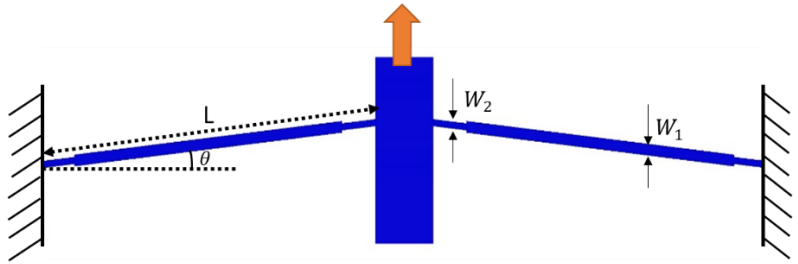


Figure 2.2: Schematic diagram of the stepped V-beam structure.

However, a notable limitation of using thermal actuators is the significant temperature increase they can induce, which might limit their usability. It is vital to meticulously control the temperature of the actuator, especially in devices used for material characterization at the specimen's points of contact. Incorporating heat sink beams can help mitigate unwanted thermal effects [101]. These beams are positioned close to the specimen to minimize the actuator's temperature influence on the specimen. For a pair of heat sink beams, the stiffness in the direction of shuttle movement is given by:

$$k_h = 2 \times \frac{12EI_S}{L_S^3} = \frac{12Eb_s^3t}{L_S^3} \quad (2.7)$$

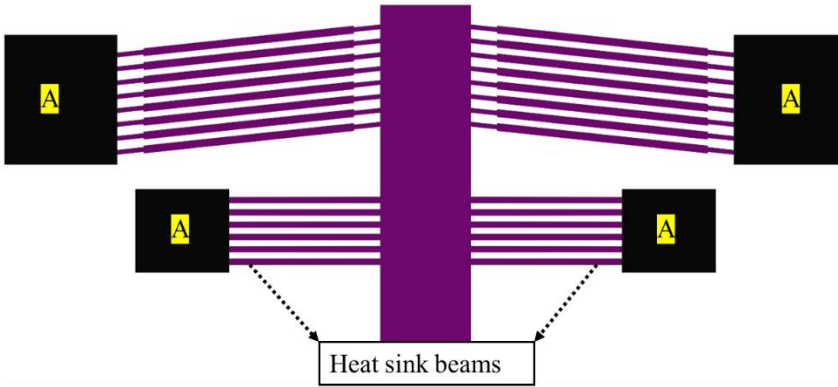


Figure 2.3 : A schematic of a thermal actuator with heat sink beams.

Applying equations 2.6 and 2.7, the axial stiffness of the thermal actuator with heat sink beams can be calculated as 20126.8 N/m.

2.5 Numerical Modeling

The understanding and optimization of MEMS-based actuators performance are crucial and can be significantly facilitated through the use of numerical modeling and simulation. Among various methods available, Finite Element Analysis (FEA) stands as a widely adopted approach. This method allows for the accurate prediction of structural, thermal, and electrical behaviors of MEMS devices, enabling a precise modeling of intricate interactions occurring between different physical domains. FEA modeling, which represents the thermal actuator as a three-dimensional solid, takes into account a number of crucial aspects. These aspects include the geometry of the device, the properties of the material used, boundary conditions, and loading conditions. In order to correctly portray the device's geometry, appropriate elements are chosen. The model also incorporates material properties such as electrical resistivity, thermal conductivity, and mechanical attributes of the actuator's material. The computational model utilizes principles from various disciplines. For thermal behavior, principles of heat transfer are applied. Electrical behavior is modeled by incorporating

Ohm's law and principles of electromagnetism, considering resistive heating due to the electric current. Mechanical behavior, on the other hand, is modeled using principles of solid mechanics, which include stress, strain, and deformation.

Boundary conditions simulate the physical constraints of the actuator. For instance, fixed supports at the base of the actuator represent the connection to the substrate, while free conditions are set at the moving parts. Loading conditions simulate the input voltage applied to the actuator, alongside the resulting heat generation due to resistive heating. After the application of suitable numerical methods to solve the FEA model, the results are post-processed and analyzed. This analysis explores aspects of the actuator's behavior such as displacement, temperature distribution, stress, strain, and the exerted force. The information gathered hereafter is harnessed to optimize the actuator's design and performance. For instance, modifying the actuator's geometry could lead to an improved displacement range or enhanced thermal efficiency. Altering the material properties might bolster the mechanical robustness or electrical efficiency of the actuator. Additionally, simulation results assist in identifying suitable operating conditions for the actuator, including the optimal input voltage and operating temperature.

Using commercial finite element software like Ansys for linear 'static structural and multiphysics simulations' can further enhance this analysis. This software offers a specialized module designed explicitly for combined electrothermic-structural simulations. By comparing numerical results with those obtained from analytical modeling, a comprehensive understanding of the actuator's behavior can be achieved, proving particularly beneficial for an in-depth analysis of the thermal actuator.

Numerical modeling and simulation thus form a powerful toolset for the design, optimization, and validation of MEMS-based thermal actuators' performance. They complement experimental approaches by offering detailed insights into the actuator's behavior, which might be challenging to acquire through experimental measurements alone. Furthermore, these methods offer a cost-effective alternative for

exploring various design options and operating conditions, accelerating the practical application development and deployment of these devices.

2.5.1 Static Structural Simulations

Linear structural simulations were conducted to investigate the influence of key parameters, such as the angle, length, and width of the V-beam, on the thermal actuator's output displacement and stiffness. During these simulations, all anchor points remained fixed, and silicon was used as the material for all structures. The simulations incorporated relevant silicon material properties, including a Young's modulus (E) of 169 GPa, a Poisson's ratio (ν) of 0.28, and a density (ρ) of 2330 kg/m³ [95]. The primary objective of these structural simulations was to assess the critical factors affecting the performance of the thermal actuator, specifically the V-beam's angle, length, and width. These parameters have a substantial impact on the actuator's output displacement and stiffness, which are essential considerations for its design and optimization.

The results of static structural simulations indicate a notable influence of stepped beams on output displacement, especially when compared to standard V-beam structures. This influence is particularly evident at low included angles, as depicted in Figure 2.4.

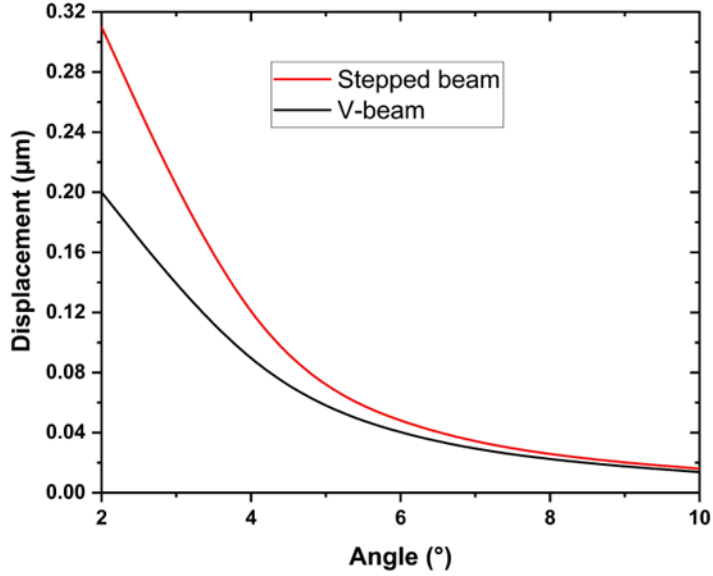


Figure 2.4: Comparison of stepped beam and standard V-beam.

2.5.2 Multiphysics Simulations

The real-time performance of the MEMS-based thermal actuator was evaluated through Multiphysics simulations with a primary emphasis on the thermal impact on the sample's displacement. The simulations deployed a sample possessing a stiffness of 835 N/m and the actuator's behavior under various boundary conditions. Mechanical boundary conditions were set to be immobile at the anchors, while the thermal boundary conditions were assigned to room temperature. Regarding the electrical boundary conditions, one anchor was grounded, and the other was exposed to varying voltage levels (0V to 3 V, incremented by 1 V), enabling the study of consequent displacement in the sample area.

The application of voltage induced current flow through the V-shaped beams, generating heat due to the Joule effect. This effect triggered a temperature rise in the structure, leading to beam expansion and consequent movement of the central shuttle. However, this temperature rise may impact other components of the device, including the sample placement area. To mitigate and manage this temperature increase, heat sink beams were integrated for efficient heat dissipation via conduction. The electro-thermal analysis, as represented in Figure 2.5, revealed that

the thermal actuator elevated the sample location temperature significantly to 126 °C when biased with 3 V, delivering a displacement of 1 μm. However, post the inclusion of heat sinks, the temperature decreased to 80 °C, and the total displacement reduced to 0.45 μm to the sample at 3V. The maximum stress observed within the structure is below 100 MPa with the same input voltage.

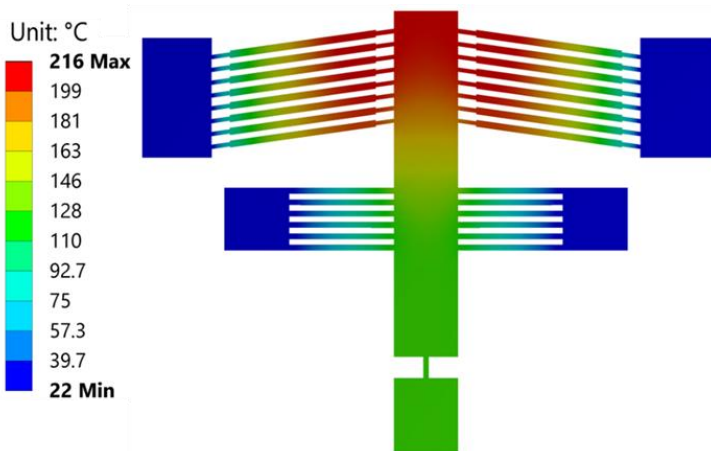


Figure 2.5: Maximum temperature of the thermal actuator when biased with 3 V.

The comprehensive simulations conducted shed invaluable light on the thermal actuator's performance. It was discerned that the maximum temperature at the sample location was reached within the anticipated displacement range (~ 0.8 μm). This presents a potential challenge, as it can be possibility to initiate thermal fluctuations, thereby compromising the accuracy and reliability of the 2D material sample's results. Consequently, it became crucial to control the temperature increase at the location of the sample in order to ensure the reliable and precise results.

To comply with design requirements, a paired set of opposite V-shaped thermal actuators was incorporated. This arrangement was designed to minimize the development of temperature gradients at the sample location. The utilization of paired thermal actuators ensures a smaller temperature distribution at the sample area, as both actuators contribute to the sample displacement. This method benefits from achieving the required displacements at lower voltages, thereby reducing power consumption and optimizing system performance. Additionally,

employing paired thermal actuators results in a reduced temperature range at the sample location, thereby enabling accurate and reliable results.

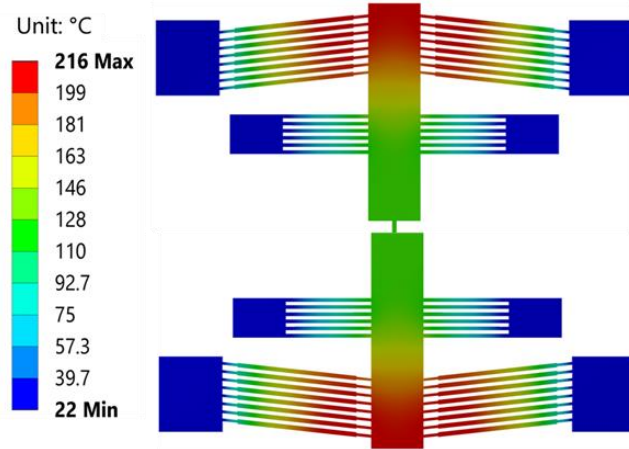


Figure 2.6: Maximum temperature in symmetrical thermal actuators when biased with 3V.

The simulations conducted in this study demonstrate that symmetrical thermal actuators can achieve the desired displacements with minimal temperature increases at the sample location, as depicted in Figure 2.6. This observation is supported by the temperature change data in Figure 2.7, indicating that longer heat sink beams result in both increased displacement and temperature increments at the sample location while decreasing stiffness. To optimize performance, we selected heat sink beam lengths based on the simulation results. These chosen lengths strike a balance between achieving higher stiffness and delivering the desired displacement to the sample, all while maintaining acceptable temperature increments.

The simulations in this study confirm that symmetrical thermal actuators can achieve the intended displacements while minimizing temperature increases at the sample location. This conclusion is reinforced by the temperature change data presented in Figure 2.7, which reveals that longer heat sink beams lead to increased displacement and temperature elevation at the sample location while reducing stiffness.

To ensure optimal performance, heat sink beam lengths were selected based on the simulation results. These lengths aim to strike a balance between enhancing stiffness and delivering the desired displacement to the sample while keeping temperature increments at the sample location within acceptable limits.

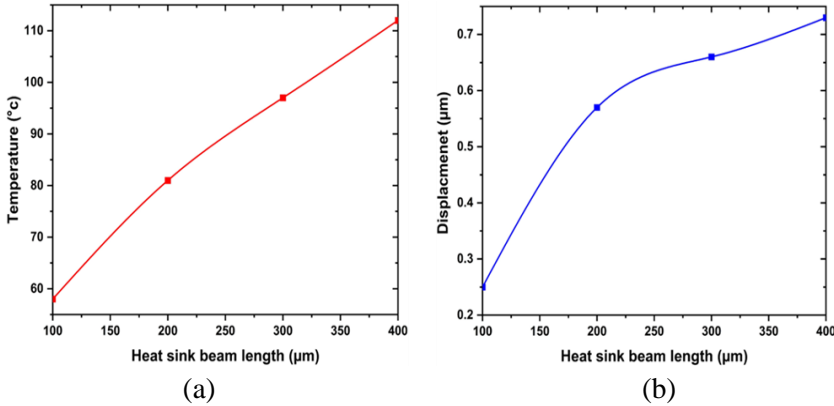


Figure 2.7: (a) temperature variation and (b) displacement in the thermal actuators with respect to the heat sink beam length variation at a constant 3V.

The optimal performance of MEMS V-shaped thermal actuators heavily depends on the appropriate choice of heat sink beam lengths and widths, as demonstrated by Multiphysics simulation results. While longer heat sink beams can provide the desired sample displacement, they also lead to increased temperature increments and decreased stiffness (Figure 2.7). Conversely, shorter beams can increase stiffness but reduce the sample's displacement delivery. Additionally, the width of the heat sink beam plays a pivotal role in performance optimization. Wider beams have shown a reduction in temperature increase at the sample location, while narrower beams enhance displacement delivery to the sample location. However, a judicious trade-off is required to achieve higher stiffness, deliver the desired sample displacement, and ensure that the temperature increase at the sample location remains within acceptable limits.

The length of the heat sink beams is inversely proportional to the temperature increment observed at the sample location and directly related to the delivery of displacement to the sample. Thus, the careful

selection of heat sink beam length is critical for controlling temperature effects and ensuring the optimal performance of the thermal actuator.

2.6 The Electro-Capacitive Sensor

The electro-capacitive sensor is a specific sensor class that quantifies alterations in capacitance, attributable to external forces. To maintain a compact form while ensuring a sensitivity threshold of at least 5 fF/nm, three distinctive types of capacitive sensors were examined.

2.6.1 Differential Transverse Comb-based Capacitors

The inaugural type is the differential transverse comb-based capacitors, employed as readout devices for quantifying the displacement delivered to the sample. The fundamental operating principle of transverse comb-based differential sensors lies in the fact that the applied force or displacement to the movable combs amplifies the finger gap on one side of the movable combs, while concurrently reducing it equivalently on the opposite side. As shown in Figure 2.8, when the gap between the movable combs changes, there is an increase in capacitance on one side and a decrease on the other side.

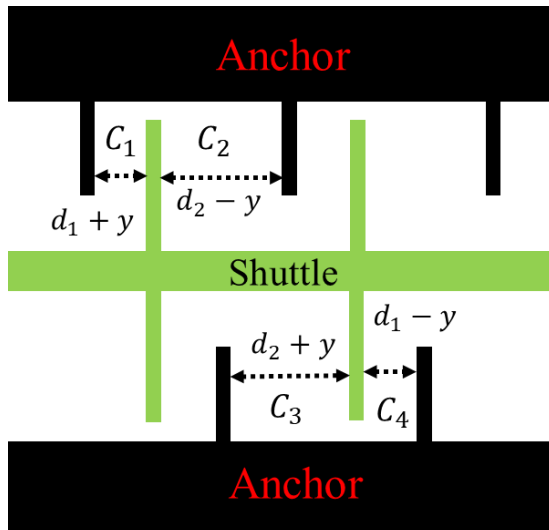


Figure 2.8: Schematic of triplate comb drive configuration.

When there is no displacement, the sensor's output is zero. However, when the sample is stretched by the thermal actuator, it experiences a displacement (y), leading to a capacitive change within the unit, as shown in Figure 7. This change can be calculated by disregarding fringe effects, as expressed by the following equations [95]:

$$\Delta C = (C_1 + C_2) - (C_3 + C_4) \quad (2.8)$$

$$\Delta C = \epsilon A \left[\frac{1}{d_1 - y} + \frac{1}{d_2 + y} \right] - \epsilon A \left[\frac{1}{d_1 + y} + \frac{1}{d_2 - y} \right] \quad (2.9)$$

Where ϵ represents the permittivity of air and A denotes the transverse area of the comb drive elements. After applying certain simplifications, the change in capacitance, ΔC , can be expressed as:

$$\Delta C = \epsilon A \left[\frac{2y}{d_1^2 - y^2} - \frac{2y}{d_2^2 - y^2} \right] \quad (2.10)$$

If $y^2 \ll d_1^2 \ll d_2^2$, it follows simply that.

The change in capacitance can be expressed as:

$$\Delta C = 2N\epsilon A \frac{y}{d_1^2} \quad (2.11)$$

Given a small displacement y and considering d_1 to be significantly smaller than d_2 (where $d_1 = 2 \mu\text{m}$ and $d_2 = 20 \mu\text{m}$), the change in sensor capacitance, ΔC , can be calculated. Using equation (2.11), the calculated change in capacitance is 5.11 fF, given that the total number of movable combs is 132, $A = \text{Area}$ ($700 * 25 \mu\text{m}$), $x = \text{displacement}$, $d_1 = 2 \mu\text{m}$, and $\epsilon_0 = 8.852 * 10^{-12} \text{ F/m}$. Therefore, the total sensitivity (S) of the capacitive sensor can be calculated as:

$$(S) = \frac{\Delta C}{y} = 5.11 \text{ fF/nm.}$$

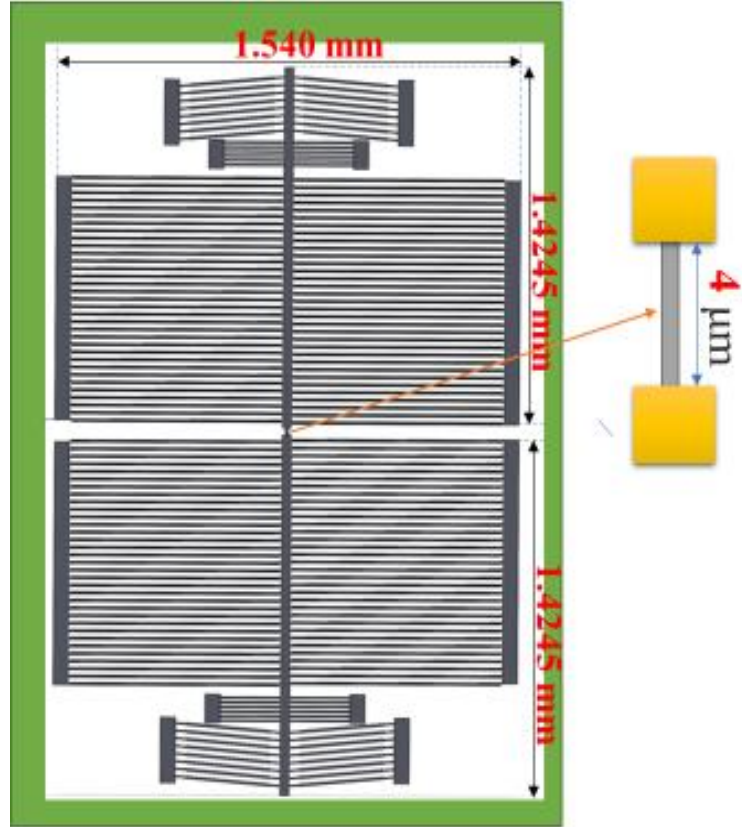


Figure 2.9: Schematic representation of the overall footprint of the MEMS testing platform integrated with a triplate capacitive sensor.

Despite the fact that triplate comb-drive capacitive sensors provide a number of benefits, including high sensitivity and great linearity, there are still issues with their current design that need to be resolved. For example, the size of the total device is larger (Figure 2.9) than the requirements for the intended in situ microscope equipment. This size discrepancy may cause compatibility issues and make it challenging to integrate the sensor into the system.

Furthermore, instability issues may arise in the triplate comb-drive capacitive sensors due to the long comb fingers that are present in the design. These instability issues can affect the accuracy and reliability of the sensor and must be addressed. Another limitation of the triplate comb-drive capacitive sensors is the inability to accurately measure the true displacement delivered to the sample, as the area occupied by the

sensor affects the measurement. This limitation arises due to the design of the sensor, which occupies a significant amount of space. Given the limitations of the triplate comb-drive capacitive sensor design, it is necessary to adopt a new type of capacitive sensor that addresses these issues in the MEMS based tensile testing devices.

2.6.2 Rotational Comb Drive

MEMS rotational comb drives are compact, low power devices with high accuracy, which have gained significant attention. These devices operate based on rotational comb drives, where two sets of interdigitated comb structures rotate in opposite directions, inducing a rotational motion in the device. These drives serve as displacement readout sensors for measuring the displacement delivered to the MEMS devices.

The rotational comb drives function by stretching the thermal actuator, which results in displacement, leading to a capacitive change. This change in capacitance is proportional to the angular displacement of the device, providing precise measurements of the rotational motion. The capacitive change is determined by the total capacitance (C_{total}), which includes the overlap capacitance ($C_{overlap}$) and gap capacitance (C_{gap}) between the concentric interdigitated combs (Figure. 2.10).

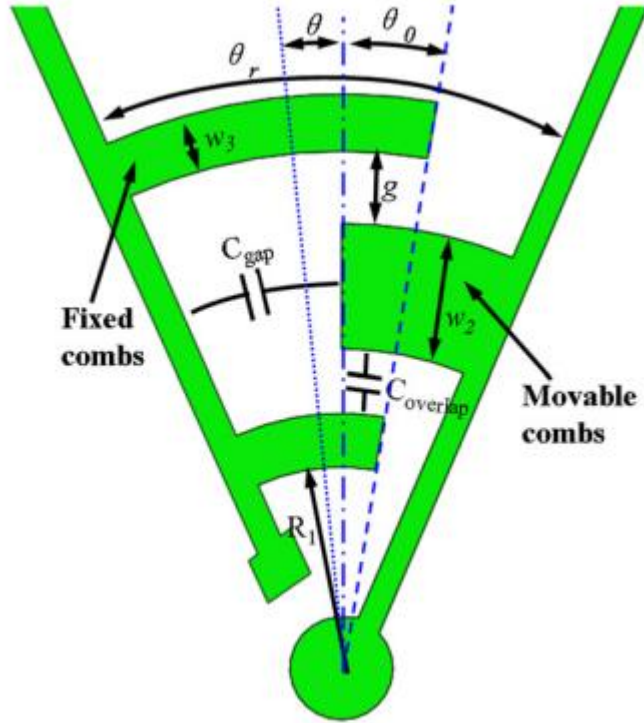


Figure. 2.10: Schematic depiction of the rotational comb drive configuration [102].

To simplify the model, all gaps are assumed to be parallel plates, and Gauss's law is used to calculate the total capacitance. The movable combs are activated by applying an excited acceleration, resulting in an angle θ being rotated from the initial overlap angle θ_0 , leading to a total overlap angle of $\theta_0 + \theta$ [102]:

$$C_{total} = C_{overlap} + C_{gap} \quad (2.12)$$

The overlap capacitance for comb fingers is given by:

$$C_{total} = \epsilon \theta (\theta + \theta_0) \times A (n) \quad (2.13)$$

Where,

$$A(n)=\sum_{i=0}^n \left\{ \left[\ln \left(\frac{R_1+2(i-1)(W_f+g)}{R_1+2(i-1)(W_f+g)-g} \right)^{-1} \right] \left[\ln \left(\frac{R_1+2(i-1)(W_f+g)}{R_1+(2i-1)(W_f+g)-g} \right)^{-1} \right] - \left[\ln \left(\frac{R_1}{R_1-g} \right)^{-1} \right] \right\}, \text{ and } W_f = \frac{(w_1+w_2)}{2}$$

The gap capacitance can be calculated by:

$$C_{gap} = \epsilon t W_f B(n) \frac{1}{\frac{\theta_r - \theta_0}{2}} \quad (2.14)$$

Where,

$$B(n) = \sum_{i=0}^n \left\{ \frac{1}{R_1+2(i-1)(W_f+g)} + \frac{1}{R_1+(2i-1)(W_f+g)} \right\}$$

Where ϵ denotes the permittivity of free space with a known value of 8.854×10^{-6} pF μm^{-1} , t is assigned to the thickness of the combs, R_1 represents the radius of the concave surface of the first movable comb set, g signifies the gap existing between the fixed and movable combs, w_1 is the width of the movable combs, w_2 corresponds to the width of the fixed combs, and θ_r is the initial angle between the fixed and movable arms.

Taking into account the nonuniform displacement inherent to the rotational comb drive, the capacitance of each comb can be determined using equation (2.13). According to the calculations of capacitance changes, the realization of the intended sensitivity calls for the inclusion of 6335 combs, arranged into approximately 19 sets. Nevertheless, such a substantial integration of combs raises considerable challenges, encompassing a need for more space and an escalated device complexity, which could heighten the risk of device fragility or even failure during the fabrication process.

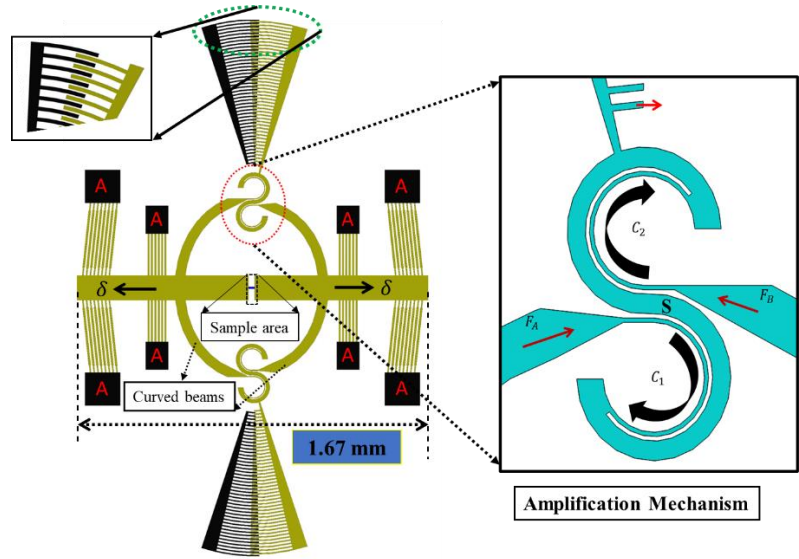


Figure. 2.11: Schematic of the MEMS testing platform featuring a rotational comb drive linked to a sigmoidal shape amplification mechanism.

A sigmoidal shape amplification mechanism is adopted, which utilizes thin curved hinges for magnifying displacements and facilitating high sensitivity. These hinges, labeled as C_1 and C_2 , exhibit opposing rotational movements, yielding rotational displacements, as illustrated in Figure. 2.11. The thin curved beams, in contrast to pseudo-rigid bodies S , deflect significantly. The amplification mechanism is interfaced with the thermal actuator's central shuttle via elliptical beams, as shown in Figure. 2.11.

2.6.2.1 Static Structural Analysis

Ansys® finite element analysis-based simulations were employed to examine the effectiveness of the amplification mechanism in enhancing the displacement to the capacitive readout sensor. The mechanism assumes a sigmoidal shape and comprises thin curved hinges (C_1 and C_2), designed to lower their stiffness and facilitate rotational motion. Upon delivery of displacement by symmetrical thermal actuators, forces F_A and F_B are transmitted to the curved hinges C_1 and C_2 , inducing clockwise and anticlockwise rotations about their rotational centers. The curved hinges C_1 and C_2 subsequently generate rotational output displacement. When each thermal actuator applies a

unidirectional input displacement of $0.5\ \mu\text{m}$ in the x-direction, an amplified displacement of $4.2\ \mu\text{m}$ (shown in Figure. 2.12) is produced at the furthest comb-drive electrodes. This mechanism affords an amplification ratio of approximately 8.4.

The central shuttle of the thermal actuator has been reduced to half its original size compared to the previously considered triplate capacitive sensors, enabling closer proximity for displacement readings to the sample. The device experiences a maximum stress of $73.7\ \text{MPa}$, whereas the stress concentration at the amplification mechanism measures $17.1\ \text{MPa}$ (Figure. 2.13). This particular amplification mechanism offers several advantages. It effectively mitigates internal stresses that could arise during operation, thereby improving the device's durability and robustness. Additionally, the mechanism exhibits a high degree of operational stability, ensuring consistent and reliable performance. Lastly, the design maximizes the overall relative rotations of the hinge, allowing for accurate and precise output measurements.

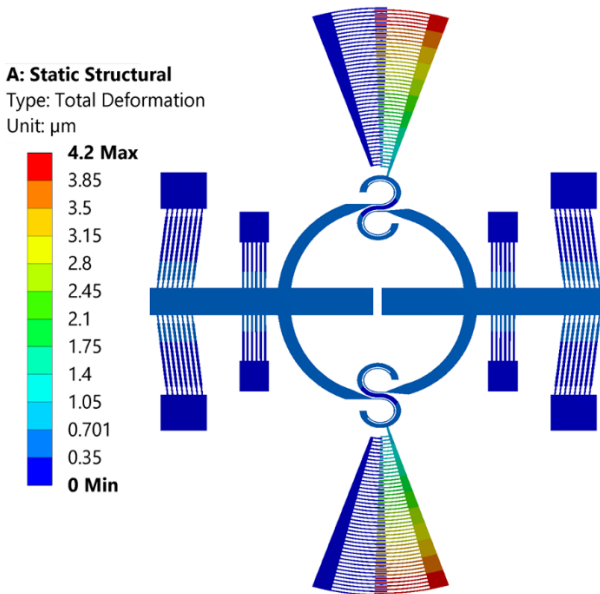


Figure 2.12: Results of static structural simulation showing output displacement.

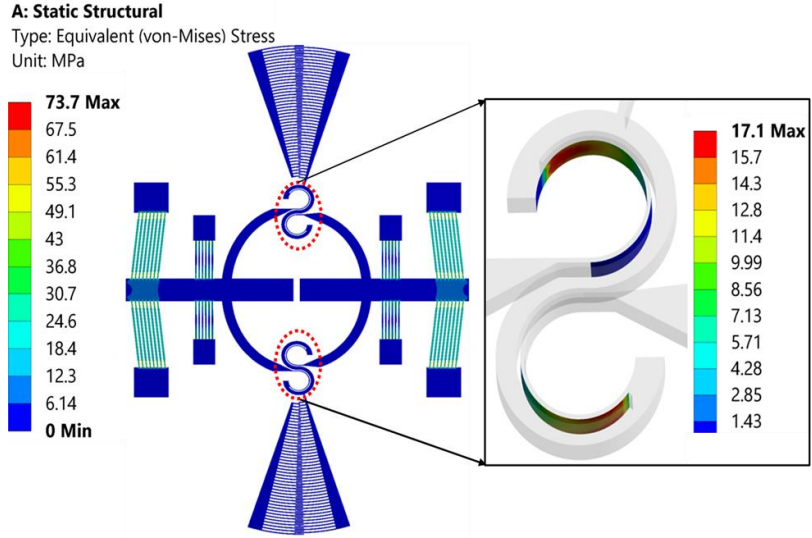


Figure. 2.13: Illustration of maximum stress distribution.

Rotational comb-drive capacitive sensors offer several advantages, but their current design faces unresolved challenges. To achieve the desired sensitivity, it's necessary to incorporate a significant number of rotational comb drives, which, in turn, increases the overall size of the device. To address these issues, a new sensor design is needed. This new sensor should aim to provide high sensitivity, excellent linearity, and a compact form factor that can seamlessly fit into in-situ microscope equipment. Furthermore, the new sensor should also tackle the non-linear displacement issues inherent in rotational comb-drive capacitive sensors, enabling accurate measurements of the true sample displacement.

2.6.3 Parallel Plate Capacitive Sensor

After analyzing the limitations of diverse comb drive configurations, the parallel plate comb drive emerges as the most suitable choice. This is primarily due to the uniform capacitance change across the comb fingers that parallel plate comb drives ensure, which is a critical prerequisite for accurate output measurements. Given the relatively small displacement range at the sample site, the introduction of a suitable amplification mechanism to enhance the displacements for the capacitive sensors is warranted. Such a mechanism would permit

precise and efficient displacement amplification, culminating in improved sensitivity and resolution. Conversely, other comb drive designs, such as triplate comb drives, suffer from instability issues stemming from elongated comb fingers, potentially leading to inaccuracies in the measurements.

A MEMS-based capacitive displacement sensor that employs a parallel plate comb drive operates by leveraging the change in capacitance between two parallel plates as the inter-plate distance varies. The plates are connected to a stationary and a movable electrode via a series of comb-like structures that interdigitate (Figure 2.14). The movable electrode is affixed to a mechanical structure that moves in response to applied displacement, thereby altering the plate separation and, consequently, the capacitance. This capacitance is subsequently measured using external circuitry, providing a means to discern the displacement experienced by the movable electrode.

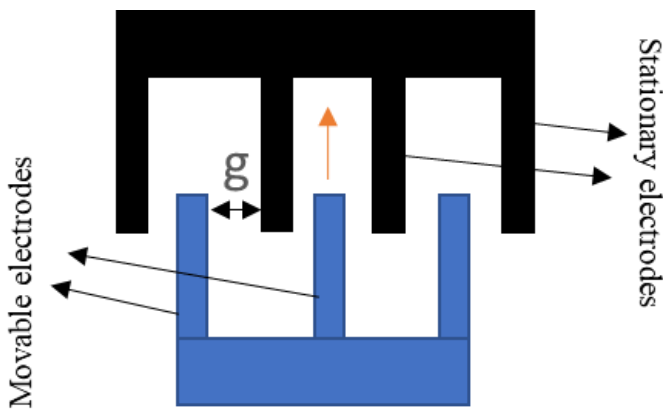


Figure. 2.14: Schematic Representation of a Parallel Plate Comb Drive.

Accurate measurement of small sample displacements necessitated the incorporation of the V-beam amplification mechanism, which comprises two flexible beams similar to the designs previously introduced in the literature [103-108], in conjunction with optimizing the parallel plate comb drive. The primary goal is to detect displacements as small as 100 nanometers with precision, requiring a sensitivity threshold of at least 5 femtofarads per nanometer, all within a compact design framework.

In this context, three distinct models were employed, with each model incorporating the V-beam amplification mechanism (shown in Figure 2.15), characterized by a pair of flexible beams. When subjected to an applied force, these beams exhibit movement along the x-axis and expansion along the y-axis, effectively mitigating x-direction compression. The primary distinction among the three models lies in their methods of transferring displacement from the thermal actuator to the comb drive [3].

Table 2.1. Comparing Amplification Factors in MEMS Devices with V-Beam Configurations.

Amplification factor [103]	20 at 2V (non-uniform)
Amplification factor [104], [105]	10
Amplification factor [105]	10 at 2 μm of input displacement
Amplification factor [106]	6.5
Amplification factor [107]	19 at 1 μm of input displacement
Amplification factor [108]	10

For instance, in Model 1, a direct linkage was established between the amplification mechanism and the central shuttle of the thermal actuator. In Model 2, however, a vertical beam was introduced to transmit displacement from the thermal actuator's shuttle to the amplification mechanism. In contrast, Model 3 employed elliptical proof masses to facilitate the connection with the amplification mechanism.

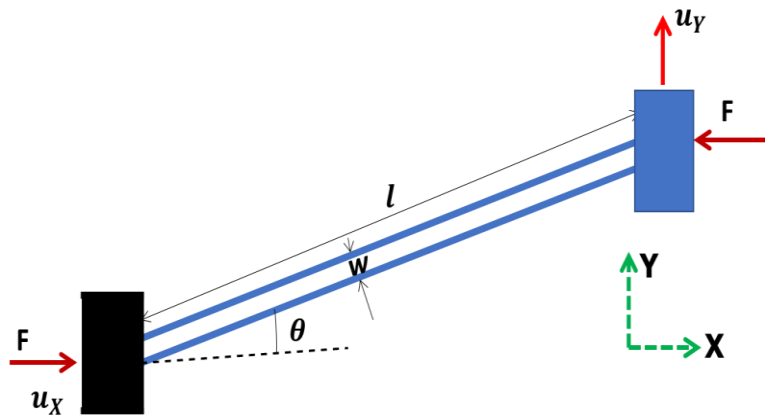


Figure. 2.15: Schematic of V-beam amplification mechanism.

2.6.3.1 Static Structural Analysis

To predict the performance of the V-beam amplification mechanism across various models, three-dimensional (3D) static structural analyses were conducted. During these simulations, all anchoring points were mechanically fixed. Silicon was chosen as the constituent material for all structures due to its unique properties. The parameters for Silicon used were as follows: Young’s modulus, $E = 169 \text{ GPa}$, Poisson’s ratio (ν) = 0.28, and density (ρ) = 2330 kg/m^3 . To streamline the simulation process, simplified models were used.

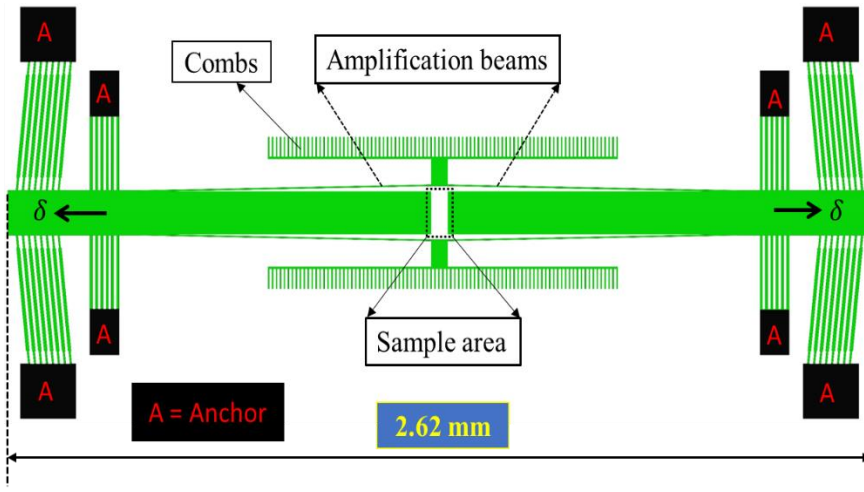


Figure. 2.16: Diagram of the MEMS-based testing platform using v-beam amplification in model-1.

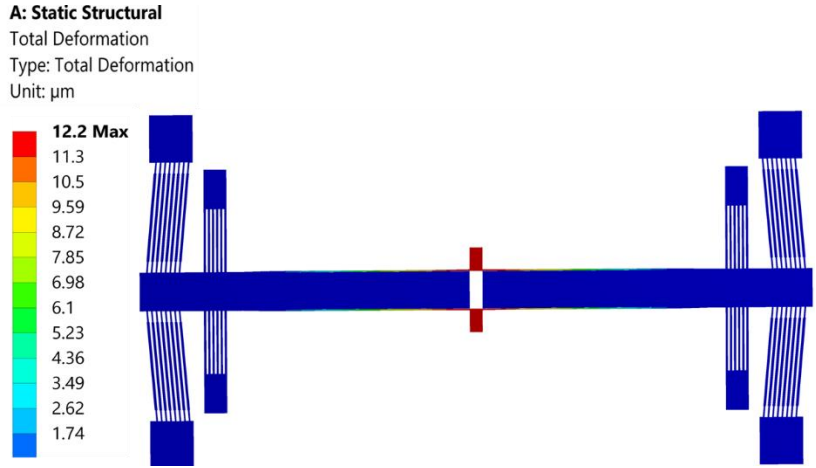


Figure. 2.17: Maximum output displacement in model-1 with an applied input displacement of $0.5 \mu\text{m}$

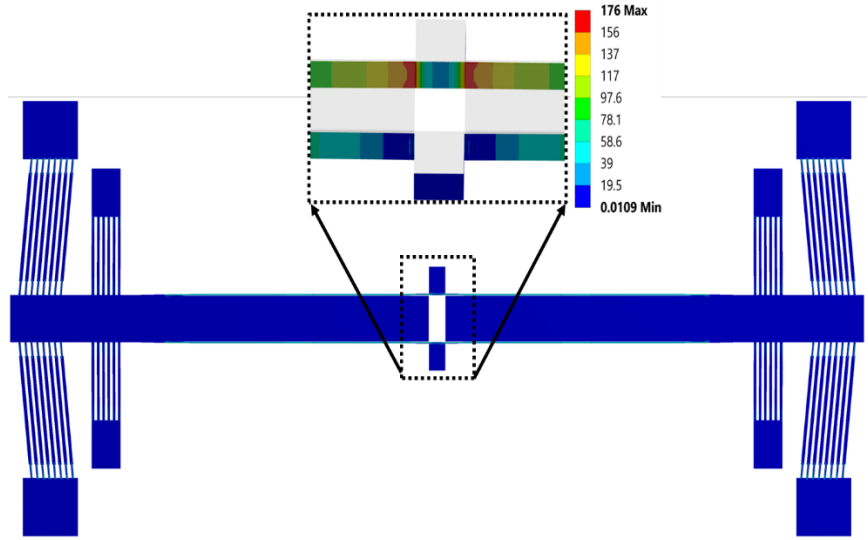


Figure. 2.18: Distribution of maximum stress in model-1 with an applied input displacement of $0.5 \mu\text{m}$.

A static structural simulation was performed for Model-1 under unidirectional loading conditions. An input displacement of $0.5 \mu\text{m}$ was applied to the central shuttle of the thermal actuator along the x-axis, causing the amplification mechanism to move $12.2 \mu\text{m}$ in a direction perpendicular to the applied displacement. The simulation revealed a

maximum stress of 176 MPa, as shown in Figures 2.17-2.18. This structure is suitable for both in-plane and out-of-plane displacements in the y-direction. This structure can accommodate both in-plane and out-of-plane displacements in the y-direction. However, when utilized for in-plane displacement, certain limitations exist—for example, it cannot move beyond approximately 14 μm —owing to the chosen angle of 1° . The amplification mechanism was designed 13.9 μm off from the sample location.

In Model-2, a rectangular movable shuttle was vertically connected to the central shuttle of the thermal actuator, creating a link to the amplification mechanism (refer to Figure 2.19). A static structural simulation was carried out under unidirectional load conditions. With an input displacement of 0.5 μm applied to the thermal actuator's central shuttle along the x-axis, the amplification mechanism exhibited a displacement of 23.5 μm perpendicular to the applied input (Figure 2.20). The simulation also revealed the presence of maximum stress, which is depicted in Figure 2.21. This design accommodates both in-plane and out-of-plane displacements in the y-direction.

It's worth noting that the total output displacement at the comb drive doubled compared to Model-1. However, there are significant concerns regarding the device's length and the stiffness of the V-beams since the comb drive relies on the support of the amplification mechanism. If there isn't sufficient stiffness, the entire structure could potentially collapse or break due to the high number of combs present in the device.

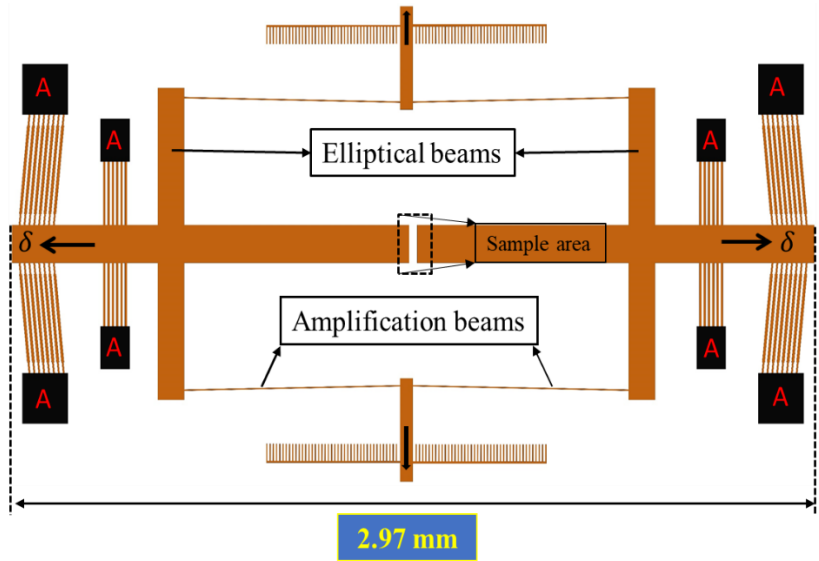


Figure. 2.19: Schematic of the amplification mechanism in model-2 for the mems testing platform.

A: Static Structural

Total Deformation
 Type: Total Deformation
 Unit: μm
 Time: 1

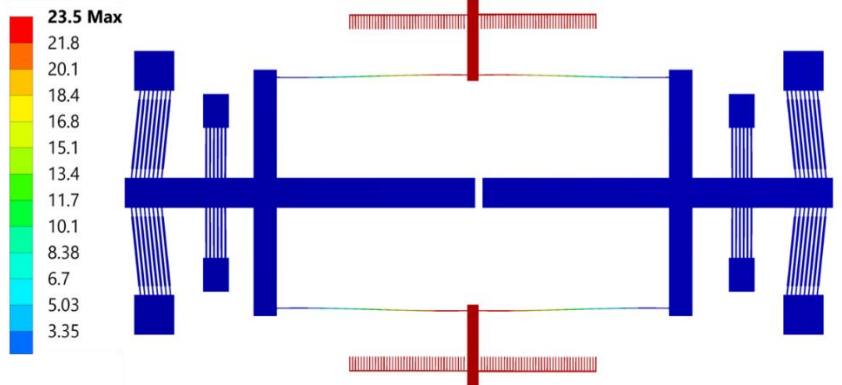


Figure 2.20: Maximum achieved displacement in model-2 with a 0.5 μm input displacement.

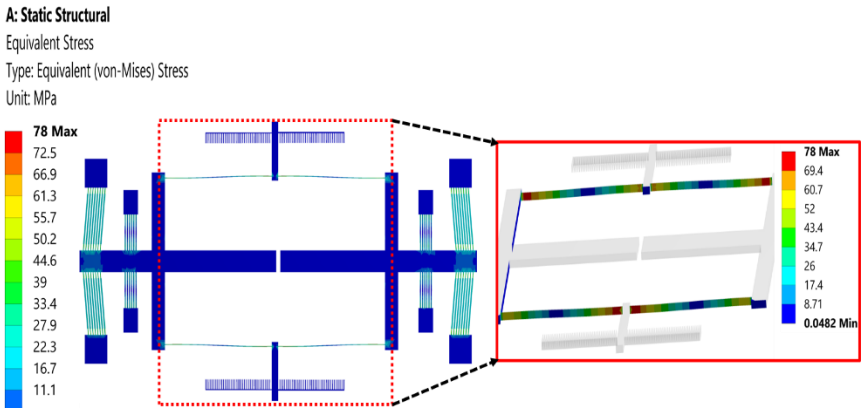


Figure 2.21: Distribution of maximum stress with a 0.5 μm input displacement applied in model 2.

The superior amplification performance demonstrated by Model-2 over Model-1 stimulated further refinement and evolution of the latter. In the revised Model-3, a defining feature is the use of an elliptical proof mass, illustrated in Figure. 2.22, which connects the central shuttle of the thermal actuator to the amplification mechanism. This ingenious adjustment not only condenses the total footprint of the device but also enhances its stiffness relative to Model-1.

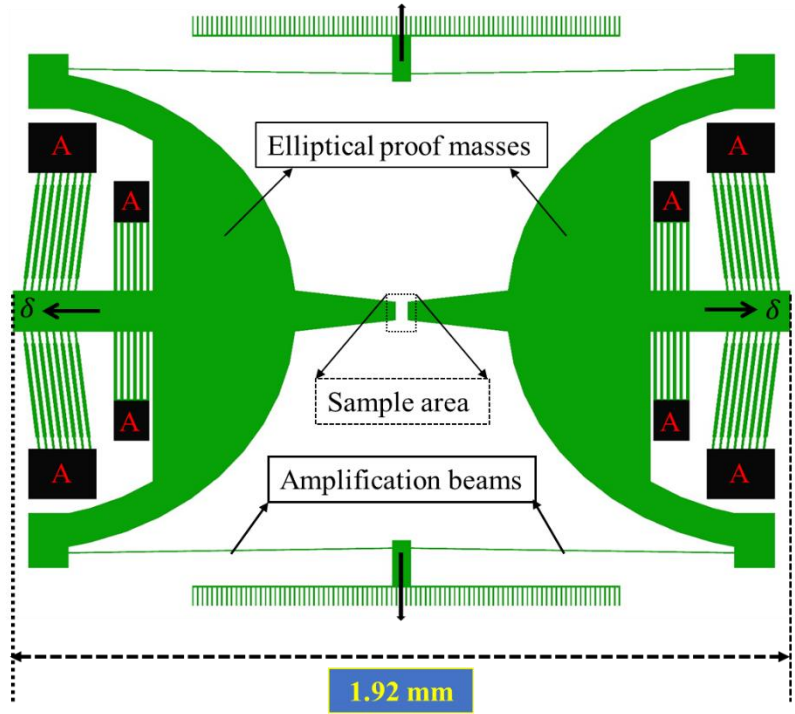


Figure. 2.22: Schematic of the model-3 amplification mechanism within the MEMS testing platform.

When a $0.5 \mu\text{m}$ input displacement was applied along the x-axis by the thermal actuators in Model-3, the V-shaped beam exhibited elastic deformation, resulting in a vertical displacement of $25.2 \mu\text{m}$ in the y-direction. The stress distribution analysis revealed a maximum stress level of approximately 182.6 MPa , as depicted in Figure 2.23. This value is well below the typical yield strength of silicon, which is 7 GPa [3]. This finding reinforces the structural robustness of the design and reduces the risk of mechanical failure under operational conditions.

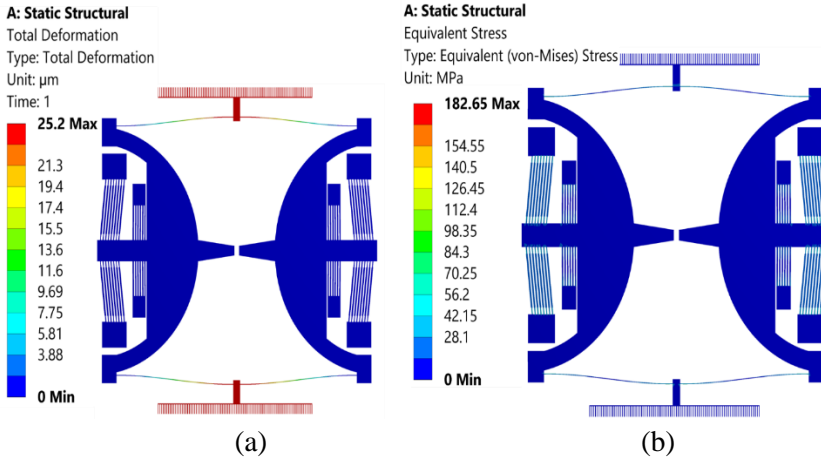


Figure. 2.23: Maximum displacement and stress distribution variables (b) in model-3 amplification mechanism.

2.6.4 Analytical Modelling

From an analytical point of view, the amplification mechanism can be modeled through the elementary theory of bending. By referring to the schematic of Figure 2.15, which shows the simplified model of one-half of the amplification beam, the deflected amplification beam is subjected to equal and opposite end forces F , along with the couples that prevent the rotation motion. Based on these conditions, the displacement in the axial direction (u_x) and lateral displacement (u_y) can be calculated as [97], [109]:

$$u_x = u_y = \frac{F \sin \theta}{k_T} \quad (2.15)$$

Where $k_A = \frac{E * w * h}{l}$ is the axial stiffness of the amplification beam and $k_T = \frac{E * w^3 * h}{l^3}$ is stiffness in the transversal direction, E is the Young's modulus, l is the length, w is the width, θ is the angle of beam, and h is the thickness ($25 \mu\text{m}$) of the amplification beam. Considering the values reported in Table 1, the axial stiffness of V-beam amplification beam results to be 42250 N/m . while the transversal stiffness results to be $\approx 1 \text{ N/m}$. The amplification ratio of the selected mechanism can be calculated as [97]:

$$Am = \frac{\Delta y}{\Delta x} = \frac{1 - \left(\frac{w}{l}\right)^2}{2 \times \left(\tan \theta + \left(\frac{\left(\frac{w}{l}\right)^2}{\tan \theta} \right) \right)} \quad (2.16)$$

The amplification ratio calculated using Equation 2.16 demonstrates a strong agreement, with a maximum difference of approximately 3% when compared to the simulation results (Figure 2.24).

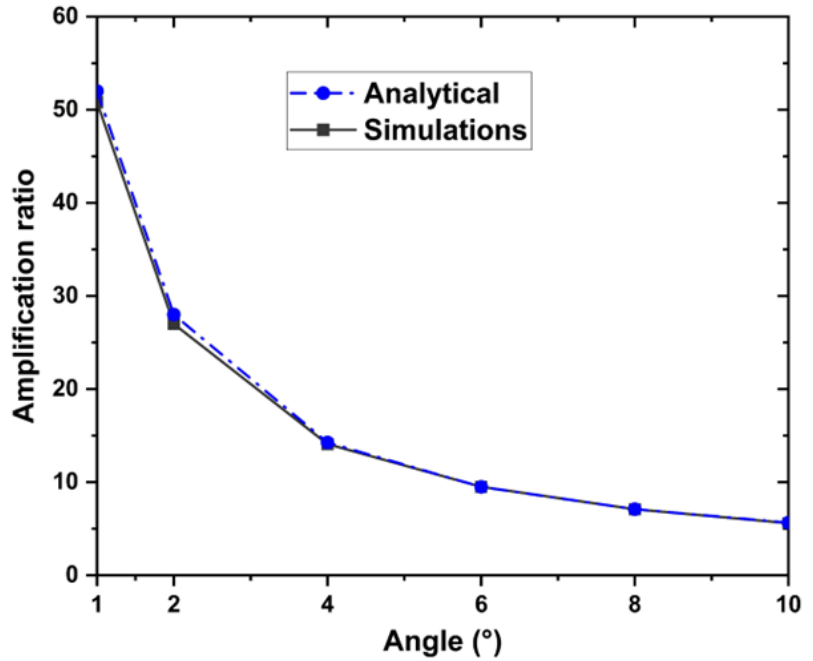


Figure. 2.24: Amplification ratio comparison with analytical formulas and simulation results with respect to the beam angle.

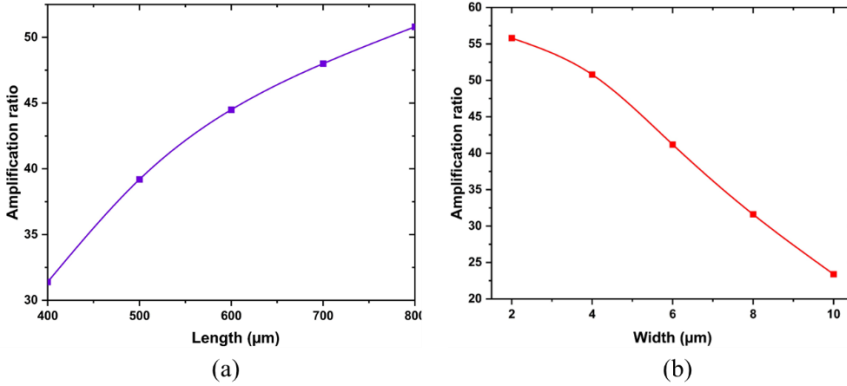


Figure 2.25: Comparison of amplification ratio with v-beam lengths and widths.

In Figure 2.25, it is evident that the amplification ratio increases with the length of V-beams. Conversely, the width of the V-beams has an inversely proportional relationship with the output amplification ratio. This means that when selecting an amplification mechanism, a trade-off between V-beam length and width needs to be carefully considered.

Table 2.2. Geometrical parameters of the device.

Total length of the beam (L_A)	350 μm
Thin beam (hinge) region length	35 μm
Thicker beam region length	280 μm
Width of small beam region (w_1)	6 μm
Width of thicker beam region (w_2)	10 μm
Number of beams pairs	8
Inclination angle	6°
Thickness (t)	25 μm
Heat sink beams ($N = 6$) width	8 μm
Heat sink beam length (L_S)	200 μm
Amplification beams ($N = 4$) width	4 μm
Amplification beam length (l)	800 μm
Amplification beam angle (θ)	1°
Curved hinges (C_1, C_2) radius (R)	50 μm
Curved hinge (C_1, C_2) width	4 μm

2.7. Final Configuration of MEMS-Based Tensile Testing Device

The MEMS-based tensile testing device's final configuration (Figure 2.27) includes double sets of opposing V-shaped thermal actuators, heat sinks, a displacement amplification mechanism, comb drives, and a specimen (Figure 2.26). Etch holes, referred to as "trenches," were added to facilitate the release of wide moving parts through HF vapor, although they are not shown in Figure 2.26.

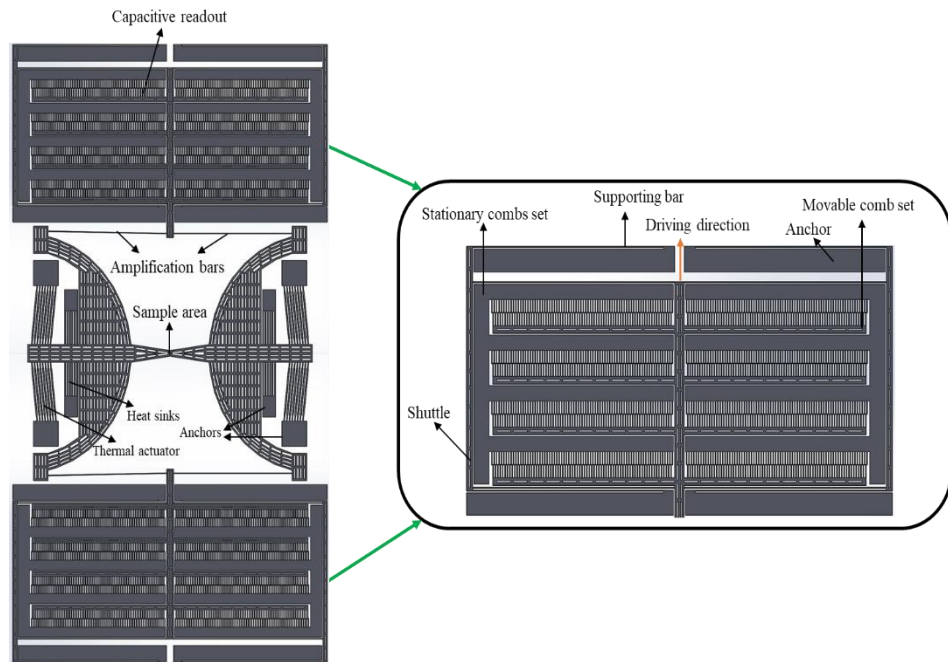


Figure 2.26. MEMS based testing platform with a comprehensive view of its components.

Steady state thermal analysis was conducted on the final MEMS based testing platform (as depicted in Figure 2.26), which comprises two symmetrical thermal actuators, heat sink beams, an elliptical proof mass, an amplification mechanism, a sample, and comb drives for capacitive sensing of displacement. This analysis considered the key electrical and thermal properties of silicon, including a thermal conductivity (K) of 130 [W/mK], a coefficient of thermal expansion (α) of $2.6 \times 10^{-6} \text{ K}^{-1}$, and a resistivity of 0.005 $\Omega \cdot \text{cm}$. To actuate the device,

a variable bias voltage was applied between the anchor points of the thermal actuators. At 3V, each side of the sample exhibited a displacement of 0.48 μm in the x-direction, achieving an overall maximum displacement of 19.74 μm at the comb-drive fingers location (in the y-direction). The device reached a maximum temperature of 131°C, with the sample location experiencing a temperature of 81°C (shown in Figures 2.28-2.29). The maximum stress of 71.56 MPa (Figure 2.30).

It is noteworthy that increasing the voltage applied to the thermal actuators resulted in greater output displacement. In the final configuration of the MEMS based testing platform, the displacement at the capacitive readout location proved sufficient to attain the targeted sensitivity of 5 fF/nm, utilizing approximately 1100 comb drives.

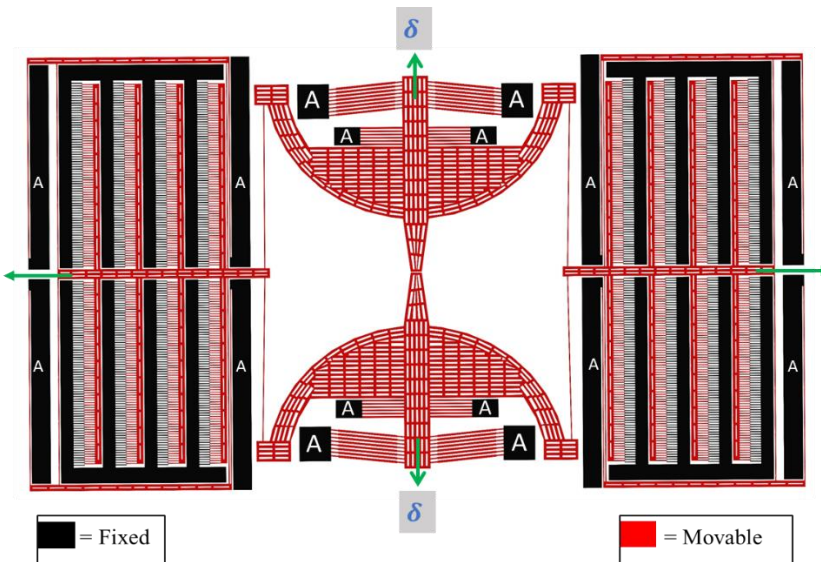


Figure 2.27: CAD model of the designed MEMS testing platform

In order to investigate the impact of 2D materials such as graphene when integrated with the designed MEMS device, simulations were conducted. These simulations involved a specimen with a stiffness of 835 N/m, which corresponds to a monolayer graphene specimen measuring 4 μm in length and 10 μm in width and were used to assess the actuator's displacement capabilities.

Chapter -2: MEMS Based Testing Platform for Investigating Strain Engineering Characterization of 2D Nanomaterials.

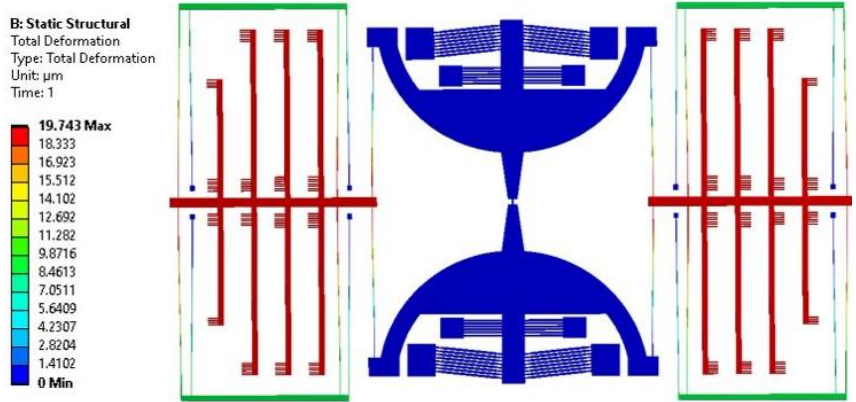


Figure 2.28: Displacement field that results when the thermal actuators are biased with a 3V with sample included.

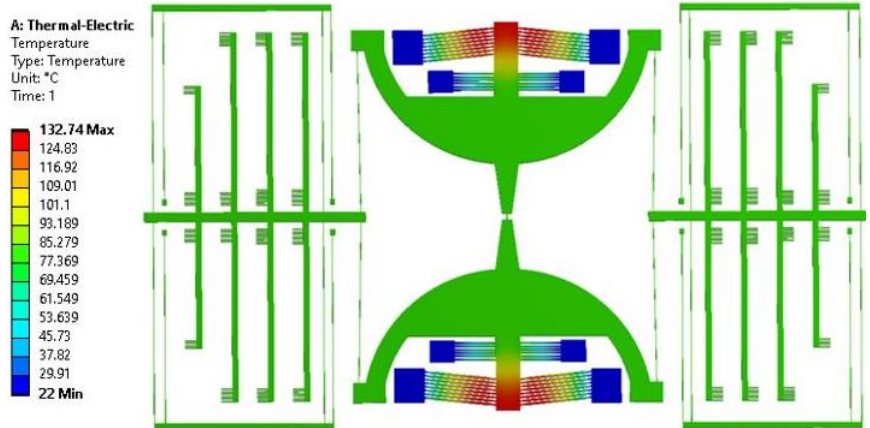


Figure 2.29. Maximum temperature when the thermal actuators are biased with a 3V with sample included.

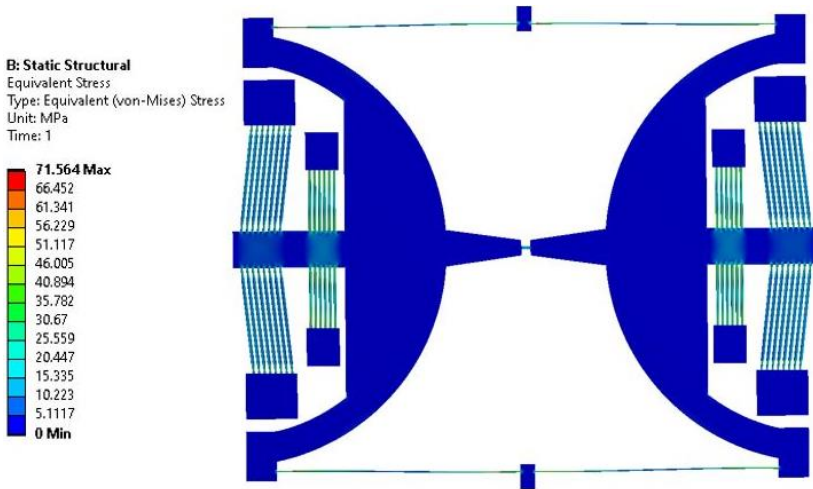


Figure 2.30. Maximum stress field resulting from the application of a 3V bias to the thermal actuators with sample included in the device.

A comprehensive modal analysis was conducted on the entire MEMS device with the primary objectives of predicting the device's natural frequencies, mode shapes, and gaining insight into its dynamic response when subjected to external excitation (Figure 2.31). The modal analysis was carried out using ANSYS Workbench software, a powerful tool for such investigations. It was revealed that the device exhibited a characteristic frequency associated with oscillation in the y-direction, which was precisely determined to be approximately 14.82 kHz. This modal analysis sheds light on the fundamental mechanical behavior of the MEMS device.

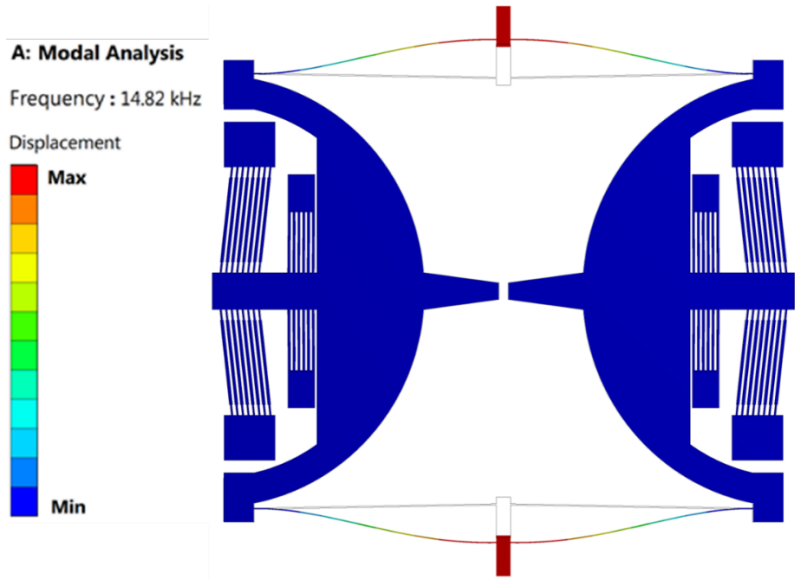


Figure 2.31. Modal analysis results and corresponding mode shape of mems device.

In consideration of the anticipated operational environment, characterized by a vacuum condition, it was determined that the impact of squeeze-film damping on the device's sensitivity is negligible. This is due to the reduced air resistance in a vacuum, which minimizes the damping effect on the device's performance. Furthermore, parasitic capacitance, which could introduce unwanted interference in the proposed capacitive readout mechanism, was deliberately omitted from the design considerations. This decision ensures that the device operates with the highest precision and reliability within the specific working conditions it is intended for.

This chapter 3 provides the design and simulation analysis of a MEMS-based tensile testing device for measuring the stress-strain properties in 2D materials. In this context, two design approaches were considered: one emphasizing high device stiffness, and the other concentrating on large displacements at lower input voltage.

3.1 Introduction

The main purpose of the MEMS-based tensile testing platform is to accurately assess the stress-strain curves of 2D nanomaterials, especially at low temperatures. Its primary functionality involves the precise measurement of the applied force to the materials during a tensile test. This device incorporates a MEMS thermal actuators, and V-shaped structure which is responsible for exerting controlled displacement on the sample. This controlled displacement enables the application of tension forces and facilitates the accurate evaluation of the material's response to stress. The collected force data can be utilized to generate stress-strain curves, which offer valuable insights into the sample's behavior under tension. These curves provide crucial information about the material's mechanical properties, including elastic modulus, yield strength, and ultimate tensile strength. A significant benefit of this device is its effective operation even at low temperatures. It is designed to ensure the actuation and force measurement components function reliably in such conditions. This capability enables comprehensive testing and analysis of 2D material samples across a broad temperature range, enhancing the device's versatility for various research and experimental purposes.

In this particular research, the two MEMS based tensile testing platforms were developed with specific design objectives. The first design, referred to as design 1, incorporated stepped V-shaped beams to achieve a high level of stiffness. On the other hand, design 2 involved a combination of classical V-shaped beams and stepped V-shaped beam structures, aiming to provide higher displacement to the sample. By employing these MEMS devices, it is possible to conduct experiments and investigations on different 2D nanomaterial samples, allowing for systematic and comparative studies. This provides valuable insights

into the behavior and performance of the nanomaterials under different conditions, aiding in the advancement of 2D nanomaterials.

3.2 Design of MEMS Based Tensile Testing Platform-1

The MEMS-based tensile testing platform, as depicted in Figure 3.1. This platform incorporates cascaded thermal actuators, offering precise control and manipulation of 2D materials. The customized MEMS device design implements the motion amplification concept, capitalizing on the movement of two side actuators to compress a vertical stepped v-beam structure. This cascaded arrangement results in an amplified motion of the central structure, enabling enhanced control and manipulation capabilities. The structural configuration of the device comprises two horizontal thermal actuators positioned on the right and left sides. These thermal actuators employ a V-shaped stepped beam configuration at the center, thereby enhancing the overall performance of the system.

In conventional MEMS thermal actuators, temperature gradients often pose issues affecting the sample. However, the current design mitigates this problem by operating the actuators at low voltage, which keeps the temperature low and results in a small displacement. This small displacement is then amplified by the vertical actuator structure, overcoming the limitations of temperature effects. The cascaded MEMS system provides not only controlled displacement but also the ability to measure strain and stress in samples. By mounting a sample to the vertical actuator which serves as a load sensor, strain and stress can be accurately measured based on the relative motion of the thermal actuators. This measurement capability opens up opportunities for strain analysis and stress characterization in various applications.

The concept of cascaded thermal actuators has been previously proposed in the literature [98], [110]–[112]. The central chevrons mechanically amplify the motion of the side actuators, which is then transferred to the test specimen. This concept has shown promise in enhancing actuation and sensing capabilities in MEMS devices.

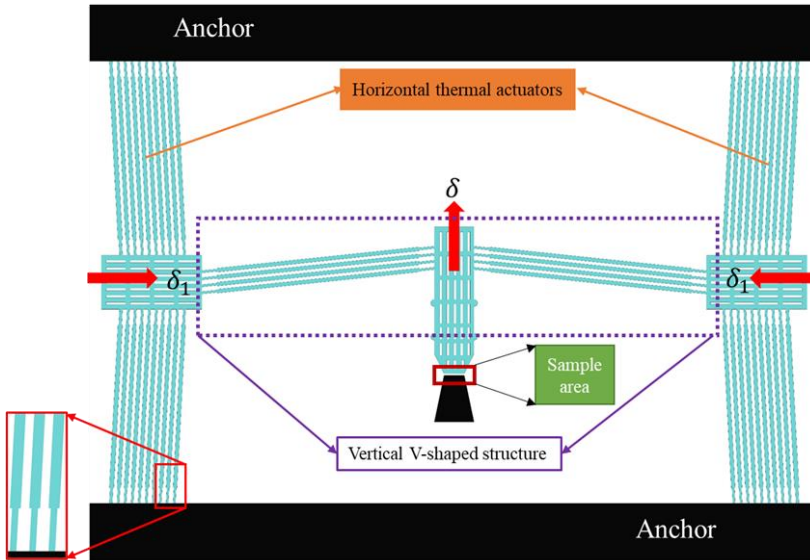


Figure 3.1: Schematic of MEMS based tensile testing platform 1.

3.3 Analytical Modelling

3.3.1 Horizontal Thermal Actuators

The horizontal actuators, positioned on both sides of the vertical actuator system, are integral components responsible for generating lateral force and displacement. These actuators play a crucial role in the overall mechanism. Their operation relies on the concept of thermal expansion caused by Joule heating. When an electric current passes through the horizontal actuators, Joule heating occurs. This phenomenon causes the chevrons, which are part of the actuator assembly, to undergo thermal expansion. As a result, the stepped V-shaped beams expand in size, exerting a lateral force and displacing the adjacent components.

They serve as the primary source of motion in the horizontal direction. By amplifying these effects, the vertical stepped V-shaped structure utilizes the force and displacement from the horizontal actuators to achieve the desired overall movement.

The actuator axial stiffness and displacement can be expressed as [111], [113]:

$$u = \alpha \Delta T \frac{\sin \theta}{\sin^2 \theta + \left(\frac{b}{L}\right)^2 \cos^2 \theta} \quad (3.1)$$

and

$$K_A = \frac{N \sin^2 \theta \times (w_1 + w_2) E t}{L_A} \quad (3.2)$$

where ΔT is the temperature gradient, N is the number of beams considered in vertical thermal actuators, w_1 is the width of the small beam and w_2 is width of the bigger beam, E is the young's modulus, t is the thickness of the beams. θ is the inclination angle with respect to the vertical axis.

Based on equation (3.2), the total calculated axial stiffness of the horizontal thermal actuator is 7381.92 N/m. The geometry of the actuator has to be chosen in order for its stiffness to be significantly higher than the expected stiffness of the sample (thus guaranteeing its displacement to not be affected by the sample).

Table 3.1: Geometrical parameters of the horizontal thermal actuator

Length of each thin beam	40 μm
Length of thick beam	420 μm
Width of thin beam	6 μm
Width of thick beam	10 μm
Angle ($^\circ$)	3
Thickness of the structure	25 μm
Number of beams	8 pair

3.3.2 Vertical V-Shaped Structure

The vertical actuator system is a system of chevrons connected to a common central shuttle and at its extents to a pair of horizontal actuators as depicted in figure 1. Based on equation (2), the total calculated stiffness of the vertical thermal actuator is 4921.2 N/m.

Vertical displacement of load sensor when there is no sample mounted can be calculated as [98]:

$$\delta_1 = \frac{\left(1 - \left(\frac{b}{L}\right)^2\right) \cos \theta \sin \theta}{\sin^2 \theta + \left(\frac{b}{L}\right)^2 \cos^2 \theta} \times u_1 \quad (3.3)$$

Where b is the width and L is the length of the load sensor beams, θ is the angle, and u_1 is the output displacement of the horizontal thermal actuators. The calculated displacement δ_1 is 4.61 when u_1 is considered as $0.5 \mu\text{m}$.

The amplification ration of the vertical thermal actuator can be calculated by:

$$A_m = \frac{\delta_1}{u_1} \quad (3.4)$$

When a sample is mounted onto the device, the force acting on the load sensor ($F \neq 0$) is half of the same needed to deform the sample.

$$F = K_A \times (\delta_1 - \delta_2) \quad (3.5)$$

Where K_A is the axial stiffness of the load sensor and δ_2 is displacement of load sensor when sample is mounted.

The vertical displacement of the load sensor when sample is mounted can be calculated as:

$$\delta_1 = \frac{2 K_A}{K_S + 2 K_A} \times \delta_2 \quad (3.6)$$

Thus, in order for the amplifier displacement v_2 to be significantly affected by the sample presence, it is necessary for K_A to be comparable with K_S . In this condition, the vertical thermal actuator can be efficiently used as load sensor, with the load being measured from the displacement difference produced by the sample presence (e.g $\delta_1 - \delta_2$). The maximum load which the amplifier can withstand, which is also half of the maximum load which can be applied to the sample, as:

$$F_{max} = \left(-\frac{EA}{L} \cos \theta \sin \theta + 12 \frac{EI}{L^3} \cos \theta \sin \theta\right) \times u_1 \quad (3.7)$$

Where E is the young's modulus and A is the cross-section area of beams, I is the moment of inertia, θ is the angle of beam.

Table 3.2: Geometrical parameters of the vertical V-beam structure.

Length of each thin beam	40 μm
Length of thick beam	520 μm
Width of thin beam	6 μm
Width of thick beam	10 μm
Angle ($^\circ$)	6
Thickness of the structure	25 μm

3.4 Numerical Analysis

To validate the accuracy of the analytical modeling, a finite element analysis (FEA) was performed using the ANSYS software. The FEA was employed to simulate the behavior of the unloaded devices, specifically focusing on static structural simulations to verify the structural integrity of the system in line with the analytical model. In the FEA simulations, specific mechanical boundary conditions were applied to replicate the experimental setup. The anchors of the device were fixed, meaning they were constrained from any movement.

When a displacement input of 0.5 μm was applied to the horizontal actuators, the vertical V-shaped structure produced the displacement of 4.69 μm and maximum stress of 86 MPa was observed at thin beams (as depicted in Figures 3.2 & 3.3). One of the critical aspects of the system was the vertical V-shaped structure, which played a role in amplifying the displacement. The FEA results demonstrated that the vertical V-shaped structure achieved a displacement amplification factor of 9.3 times the applied displacement. Remarkably, this FEA result closely matched the analytical results, exhibiting a deviation of merely 1.7% from the analytical predictions based on Equations 3.3 and 3.4. The comparison between the FEA and analytical results indicates strong agreement and validates the accuracy of the analytical modeling approach.

A: Static Structural

Total Deformation

Type: Total Deformation

Unit: μm

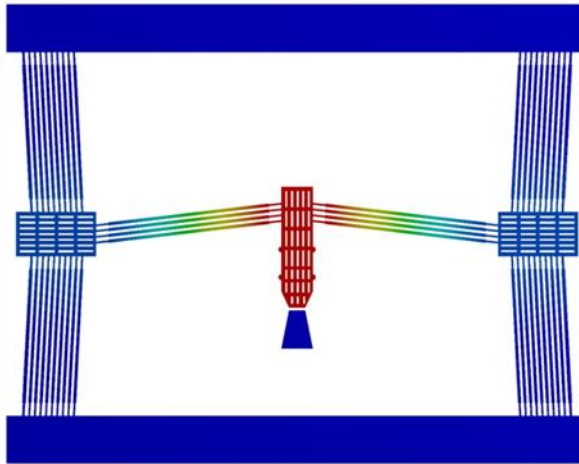
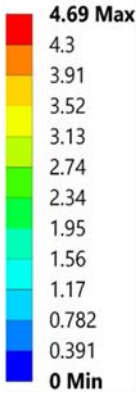


Figure 3.2: Displacement of vertical stepped v-beam structure with $0.5 \mu\text{m}$ horizontal actuators displacement.

B: Static Structural

Equivalent Stress

Unit: MPa

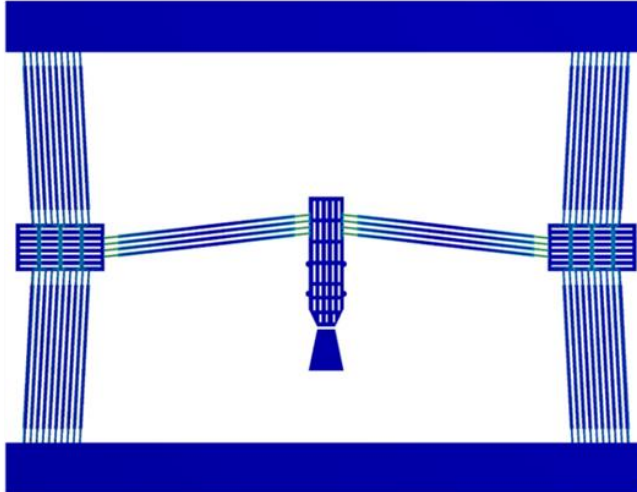
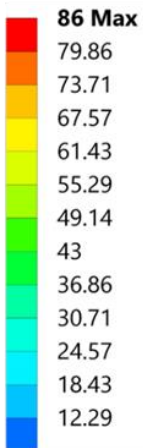


Figure 3.3: Maximum stress resulting from $0.5 \mu\text{m}$ displacement of the horizontal thermal actuator.

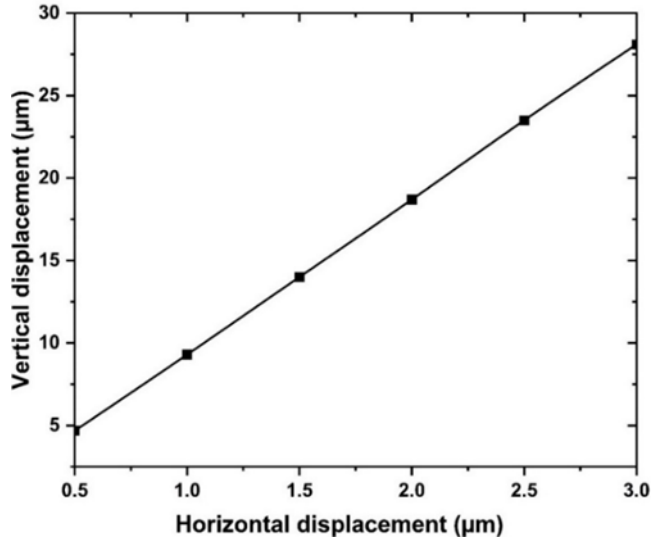


Figure 3.4: Horizontal thermal actuators displacement versus displacement of vertical stepped v-beam structure.

Figure 3.4 demonstrates the relationship between the input horizontal displacement and the corresponding vertical displacement. It reveals that as the input horizontal displacement applied to the thermal actuators increases, the vertical displacement of the V-shaped structure also increases approximately 9.3 times. The relationship between the two variables is described as linear. This indicates that for each incremental unit of horizontal displacement, the vertical displacement also increases by a consistent amount.

In order to comprehensively capture the behavior of the MEMS cascaded thermal actuator system with the real time conditions, a Multiphysics finite element analysis (FEA) was conducted. This coupled model accounted for the interaction of electric, thermal, and mechanical fields within the device. The input parameter for this analysis was the applied voltage, which served as the electrical boundary condition. The electrical boundary condition was set at the anchors of the device, representing the points where the electrical connections were made. To account for the mechanical behavior, fixed displacements were set as the mechanical boundary conditions at the anchors. This ensured that the anchors were firmly held in place and prevented any unintended movement or deformation during the

analysis. By incorporating these boundary conditions, the FEA accurately represented the mechanical response of the device under the applied voltage. A thermal boundary condition was implemented by fixing the temperature at the anchors to a constant value as a room temperature. The FEA results allowed for visualization of the thermal and displacement fields within the MEMS cascaded system. Figure 3.5 depicted the thermal field, showing the temperature distribution across the device, while Figure 3.6 presented the displacement field, illustrating the resulting displacements within the system. These visual representations provided insights into the temperature variations and the displacement magnitudes across different regions of the device.

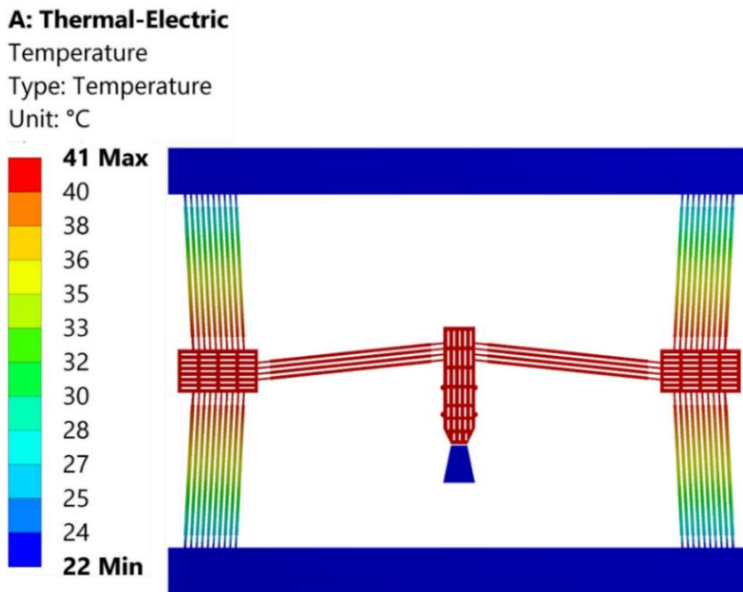


Figure 3.5. Maximum temperature when the thermal actuators biased with 1 V.

Figure 3.7 presents the Multiphysics simulation results, which demonstrate the relationship between displacement and temperature changes in response to the applied voltage. Both fields consistently exhibit a linear increase, allowing for the evaluation of a MEMS-based tensile testing device's performance across various input voltages and its specific application's safe operation.

The vertical V-shaped structure easily achieves the intended displacement, and in such structures, addressing thermal fluctuations to

attain substantial displacement can be effectively mitigated by utilizing this design. The investigation of the relationship between applied voltage and the output displacement of the MEMS-based tensile platform at the vertical stepped V-shaped structure revealed a clear correlation. Increasing the voltage leads to a proportional increase in the displacement, illustrating the precise control of the thermal actuators over the platform's displacement.

Furthermore, the figure provides insights into the effect of the applied voltage on the temperature in the testing platform. As voltage increases, the temperature of the structure also rises, crucial for understanding the device's thermal behavior and its implications for applications requiring specific temperature ranges or thermal stability.

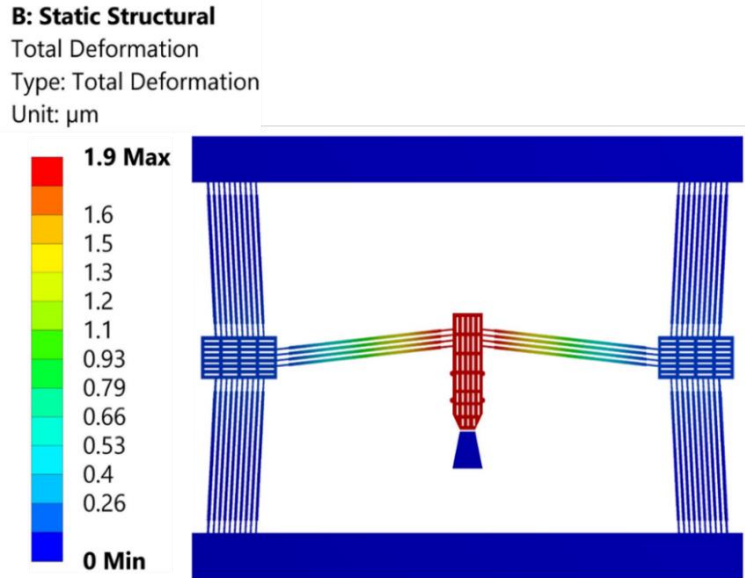


Figure 3.6: Maximum displacement when the thermal actuators biased with 1 V.

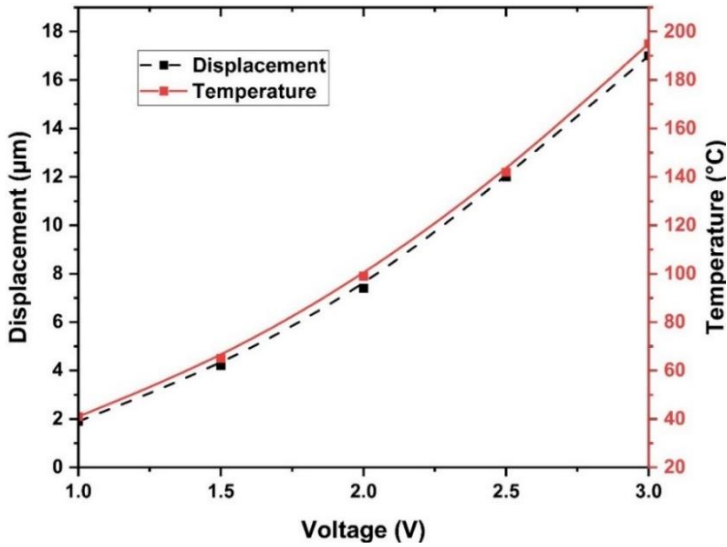


Figure 3.7: Voltage-displacement – temperature relationship of mems-based tensile platform at vertical stepped V-shaped structure.

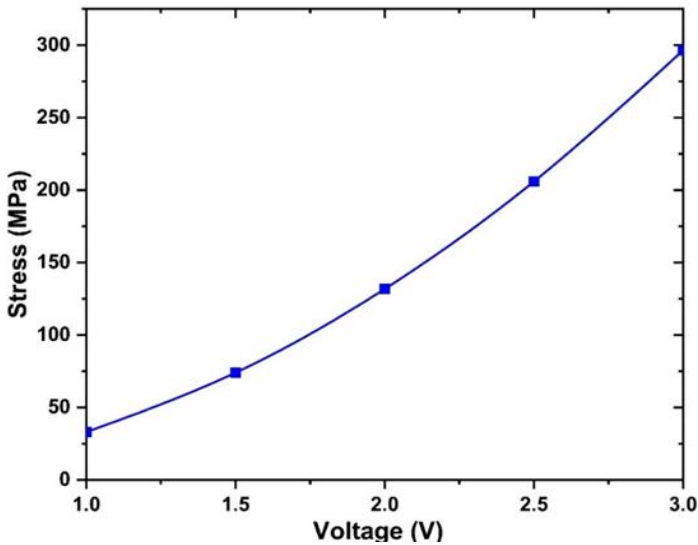


Figure 3.8. Relationship between the applied voltage and maximum stress in the MEMS based tensile testing platform design 1.

In Figure 3.8, the relationship between the applied voltage and the maximum stress observed in a MEMS-based tensile testing platform is depicted. Maximum stress values are measured at various voltage levels, revealing an intriguing trend. Initially, as the applied voltage

increases, the maximum stress also rises. However, beyond a certain threshold, the maximum stress levels off and does not significantly increase with further voltage increments. Notably, at 3V, the maximum stress remains below 300 MPa, which is lower than the yield strength of silicon material. This finding is significant as it implies that the MEMS-based tensile testing platform can operate safely within stress limits without surpassing the material's yield strength. Careful control of the applied voltage allows for the regulation and limitation of stress levels experienced by the device and the specimens being tested.

3.5 Design of MEMS Based Tensile Testing Platform-2

MEMS based tensile testing platform design-2, a concept known as motion amplification is incorporated, similar to testing platform-1. This concept utilizes the movement of two side actuators to compress a vertical stepped V-shaped structure, resulting in amplified motion. The device's structural configuration combines a classical V-beam thermal actuator, consisting of two horizontal thermal actuators, with a V-shaped stepped beam configuration for the vertical structure. This combination enables enhanced performance in terms of control and manipulation capabilities.

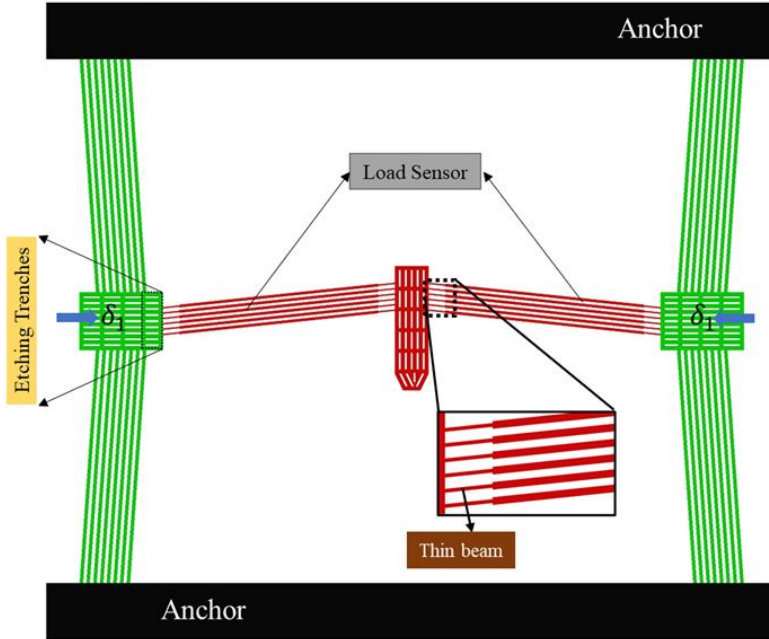


Figure 3.9: Schematic of mems based tensile testing platform design 2.

Table 3.3. Geometrical parameters of MEMS based tensile testing platform design 2.

Horizontal Thermal actuators		Vertical thermal actuator	
Number of beams	8 pair	Number of beams	6 pair
Angle	4°	Angle	6°
Length of the beam	700 μm	Total length of the beam	600 μm
		Each thin beam length	50 μm
Width of the beam	10 μm	Thick beam	8 μm
		Thin beam width	4 μm
Thickness		25 μm	

3.5.1 Analytical Modelling and Numerical Analysis

The thermal actuators have a classical V-beam configuration with a freestanding shuttle, anchored to the substrate through a series of V-shaped beams. When a voltage is applied across the V-shaped beams, the corresponding current flow generates heat by Joule effect. The dissipated heat causes thermal expansion of the beams, which results in a horizontal movement.

According to the analysis reported in [95], the actuator displacement can be calculated by using equation (3.1) and axial stiffness be expressed as:

$$k_A = 2N \left(\frac{EA}{L} \sin^2\theta + 12 \frac{EI}{L^3} \cos^2\theta \right) \quad (3.8)$$

Where E is the Young modulus, I is the moment of inertia, A is the transversal area, b is the width, L is the length, t is the thickness, θ is the inclination angle with respect to the vertical axis, and n is the number of V-shaped beams. The total axial stiffness of the horizontal thermal actuators is 4889.5 N/m.

Based on the equation (3.3), the vertical V-shaped structure displacement calculated as $4.7 \mu\text{m}$ at $0.5 \mu\text{m}$ of input displacement (u_1) and the amplification ratio is 9.4 (Figure 3.10). The axial stiffness of (K_A) is calculated as 3163.68 N/m by using equation (3.4). The stiffness of the actuator is varies based on the number beams used, it is inversely professional to the output displacement by the actuator. So, it is very important to optimize the structure based on the intended performance.

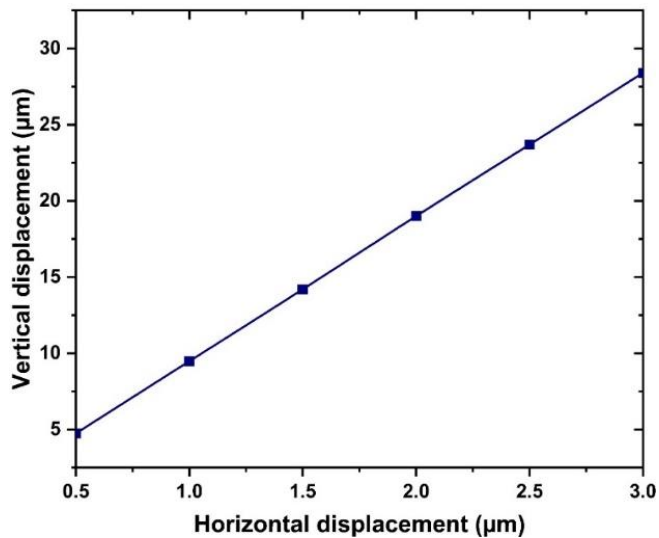


Figure 3.10: Analytical modeling results for the displacement of a vertical V-shaped structure in response to applied horizontal displacement at thermal actuators on both sides.

The Multiphysics simulations were carried out with the same boundary conditions as mentioned in the case of cascade MEMS device design 1. When a voltage is applied across the V-shaped beams, the corresponding current flow generates heat by Joule effect. The dissipated heat causes thermal expansion of the beams, which results in a horizontal movement.

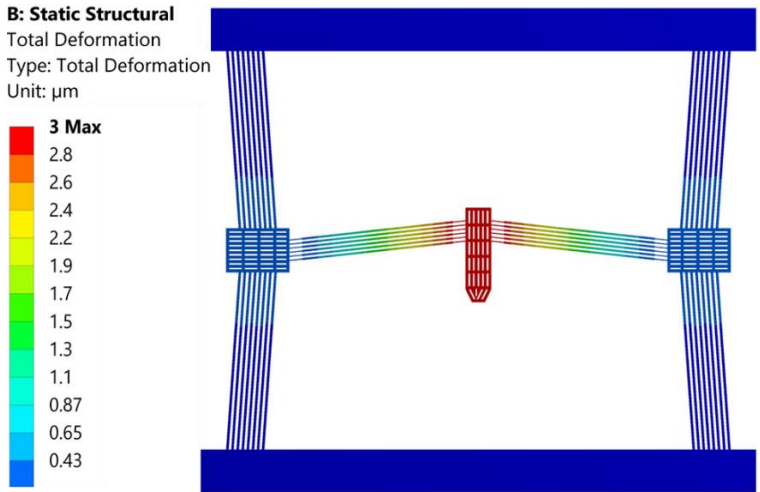


Figure 3.11: Maximum displacement when the thermal actuators biased with 1 V.

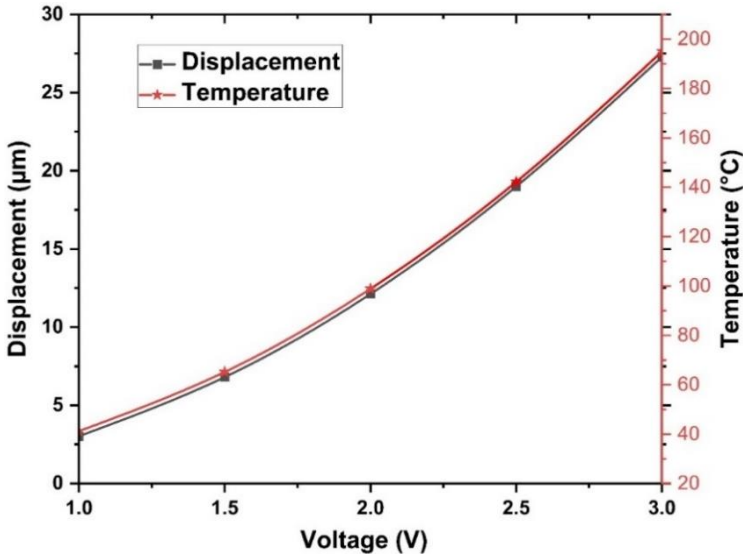


Figure 3.12: The relationship between displacement and temperature at a vertical V-shaped structure in response to applied voltages at thermal actuators.

In Figure 3.11, the Multiphysics simulations reveal a maximum displacement of $3\ \mu\text{m}$ at an input voltage of 1V, representing a nearly 60% increase compared to testing platform design 1. This increase is primarily due to the reduced stiffness of the thermal actuators.

Figure 3.12 displays Multiphysics simulation results demonstrating the consistent linear relationship between displacement and temperature changes in response to applied voltage. The maximum temperature and displacement observed are 195°C and approximately $26\ \mu\text{m}$, respectively, at 3V.

In Figure 3.13, the relationship between applied voltage and maximum stress in a MEMS-based tensile testing platform is depicted. The maximum stress initially increases with rising voltage but levels off beyond a certain threshold. Notably, at 3V, the maximum stress remains below 250 MPa, which is lower than the 7 GPa yield strength of silicon material.

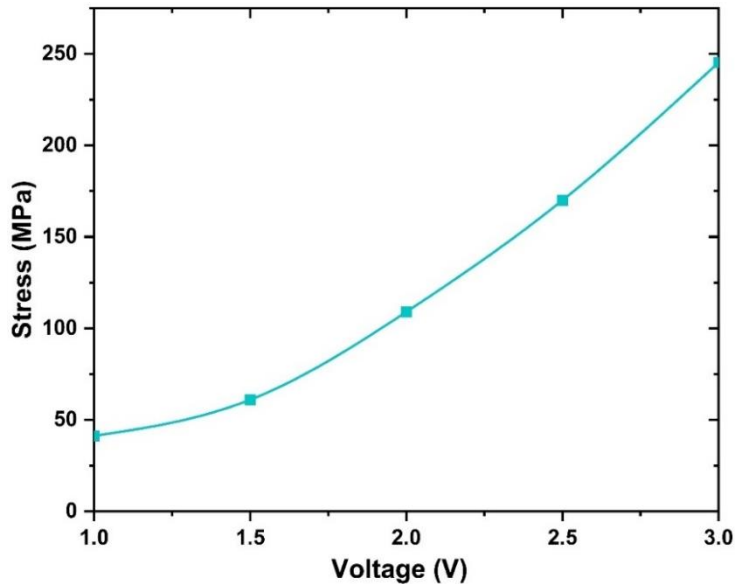


Figure 3.13: The maximum stress with respect to the applied voltages in MEMS-based tensile testing platform 2.

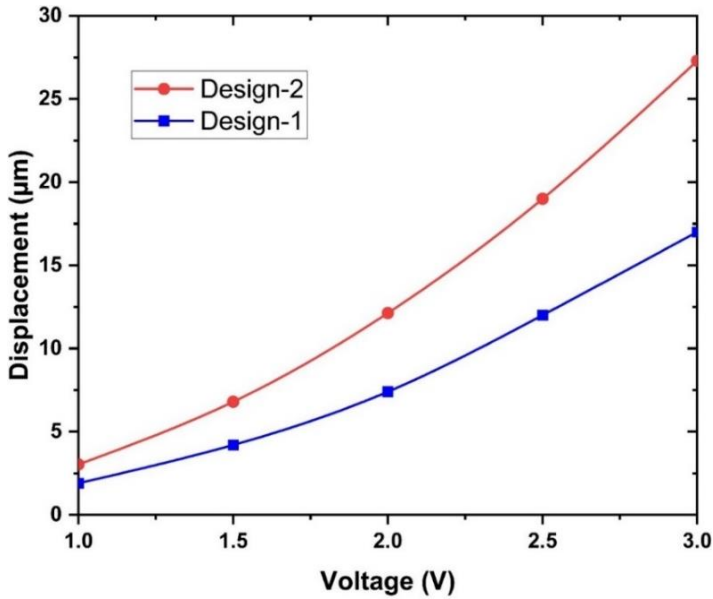


Figure 3.14: A comparison of Multiphysics simulation results for output displacement with applied voltages.

In Figure 3.14, we compare the Multiphysics results between design-1 and design-2. At lower voltages, the displacements are quite similar, with 58%. However, as the applied voltage increases to 3V, the difference increases to maximum of 73%.

Both devices are designed for the 2D nanomaterial tensile testing application. Design-1 is characterized by higher stiffness, whereas design-2 offers substantial output displacement while minimizing temperature increment within the system.

In this chapter 4, there are different MEMS based test structures that were developed based on the use of intended applications. For example, the electrostatic actuator was designed to characterize the mechanical properties of silicon material at low temperatures. On other hand the MEMS based rotational structure was developed to amplify the displacements in MEMS devices.

4.1 Introduction

Electrostatic Micro-Electro-Mechanical Systems (MEMS) actuators play a pivotal role in the world of microsystems due to their remarkable simplicity, ease of fabrication, and low power consumption. These actuating devices are often the first choice when designing MEMS systems, primarily because of their inherent advantages, one of which is their dual functionality as both sensors and actuators. This multifunctionality is made possible through Coulomb's law, which states that when a voltage is applied across two plates, the resulting charge imbalance generates a force inversely proportional to the distance between these plates. The equilibrium between electrostatic and external forces is maintained by a spring force that seeks to keep the movable plate at its undisturbed position [114]–[116].

However, as voltage levels change, an imbalance emerges between these forces, compelling the mobile plate to move either closer or farther from the static plate, thereby restoring equilibrium. In an ideal scenario, this motion could extend to the limits of the initial gap between the plates. Nevertheless, reality introduces the intricacies of instability between the spring and electrostatic forces. During actuation, the electrostatic force tends to increase faster than the spring force, leading to a phenomenon known as "pull-in instability," where at approximately one-third of the initial gap distance, the mobile conductor snaps into the fixed conductor, causing device failure. To address this issue and enhance the displacement range, ongoing research efforts are dedicated to improving these actuators [117].

Electrostatic actuators manifest in five principal configurations: cantilevers, clamped beams, parallel plates, torsional plates, and comb drives. The cantilever design involves a suspended beam with a parallel

plate beneath it, while clamped beams are anchored at both ends. In contrast, parallel plates feature suspended plates anchored at their four corners and operate similarly to cantilevers. Torsional actuators, on the other hand, differ in that they are suspended along the midline of parallel plates, relying on two pads to induce rotational motion about the arms' axis. These four designs predominantly exhibit motion in the vertical direction [118].

In contrast, comb drives differ significantly by moving in the horizontal direction parallel to the wafer's surface. Comprising two interdigitated finger structures—one fixed and one movable—comb drives leverage increased overlapping areas and the generation of stronger electrostatic forces in the horizontal direction. Additionally, these actuators overcome the pull-in effect, as the electrostatic force becomes inversely related to displacement rather than being squared with displacement. Comb drive actuators are commonly employed in various applications, including resonators, electro-mechanical filters, optical shutters, micro-grippers, and voltmeters [119]. Apart from their actuation applications, electrostatic sensors are integral to MEMS technology, employing identical structures to their actuating counterparts. However, instead of mechanically responding to electrical stimuli, they electrically detect external mechanical stimuli by measuring changes in capacitance. Capacitive sensors, a prominent type of electrostatic MEMS sensor, offer numerous advantages, including high sensitivity, low power consumption, simple design, minimal drift, and low temperature dependence. These attributes are attributed to the relationship between capacitance and structural geometry, dielectric properties, and gap distances [120].

The study of electrostatic comb drives, in particular, reveals their significant role in MEMS technology. These actuators, marked by their straightforward design and fabrication processes, generate strong electrostatic forces, especially at reduced dimensions. The comb drives consist of two interlocked comb-shaped structures, which, when charged oppositely through the application of an external voltage, are attracted to one another. However, these devices may require multiple fingers to produce sufficient force, reducing their areal efficiency. While other electrostatic actuators, such as the dipole surface drive and shuffle drive, can produce more force, they tend to be more complex to

fabricate and control. The electrostatic comb drive's force is directly proportional to increasing capacitance and its direction, which means the device operates in a non-linear manner. Springs are often employed to limit transverse motion and prevent side snap-in as the force increases with decreasing finger gap, ensuring the reliable operation of electrostatic comb drives in MEMS applications.

4.2. Design and Analytical Modelling

In order to conduct low temperature bending tests on silicon materials, an electrostatic actuator was designed. This actuator utilizes one of the folded spring's beams (depicted in Figure 4.1) as a silicon test sample within a specific testing environment, as shown in Figure 4.2. The device features six sets of comb-drives and is suspended by folded springs. When an actuation voltage is applied to the comb-drive electrodes, it induces an electrostatic force, driving the electrostatic actuator in the direction where the sample undergoes bending tests. The maximum displacement of the actuator depends on the stiffness of the device structure and the actuation force generated by the comb-drive actuators. Two types of folded springs are employed as suspension structures. These folded springs are designed with high compliance in the actuation direction to allow substantial displacements while maintaining high stiffness in the lateral direction to prevent lateral instabilities. Beam deflection theory is used to describe the stiffness of a doubly clamped beam in both the motion and lateral directions.

4.2.1 Spring Design

Springs are pivotal components in MEMS electrostatic actuators, supplying the necessary force for actuation and movement. Various spring designs are employed, including clamped-clamped beams, crab-leg flexures, and folded flexures [121]. The clamped-clamped beam spring is a straightforward and commonly used design, where a beam is anchored at both ends, and voltage is applied between the electrodes to create an electrostatic force, deflecting the beam. However, this design has limited deflection and typically requires high voltage to achieve the desired displacement. The crab-leg flexure spring, on the other hand, is a more intricate design, utilizing interconnected beams arranged in a

crab-leg-like structure, offering greater deflections compared to clamped-clamped beam springs. Nevertheless, it is more challenging to fabricate and can be sensitive to fabrication tolerances. In contrast, folded springs exhibit high compliance in the actuation direction for substantial displacements and greater stiffness in the lateral direction, effectively preventing lateral instabilities.

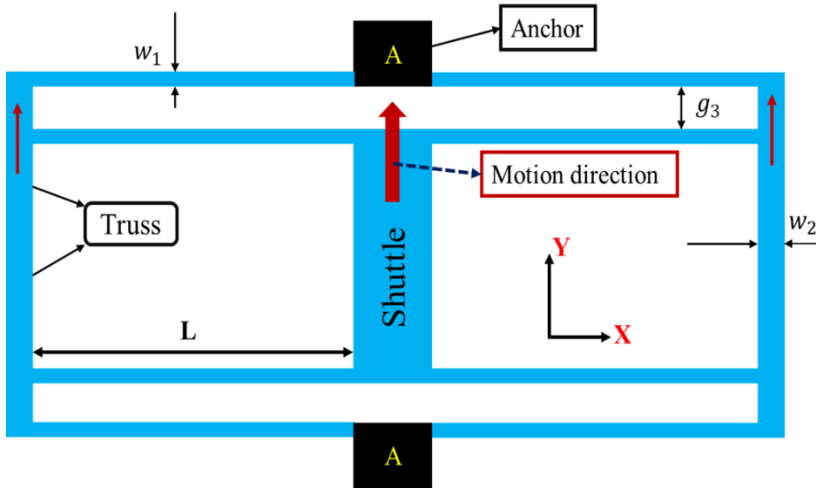


Figure 4.1: Schematic of folded spring configuration

The linear spring constant is established by subjecting the spring to a concentrated load. It can be represented as follows:

$$K_i = \frac{F_i}{\delta_i} \quad (4.1)$$

Here, F_i signifies the force, and δ_i denotes the deflection in the i direction.

The folded beam design, features beams anchored at the center and interconnected by trusses that facilitate expansion along the x -axis. Assuming rigid trusses, the spring constant for the folded flexure design can be determined in both the axial and lateral directions, resulting in the following equations:

$$K_x = \frac{2Eht}{L} \quad (4.2)$$

$$K_y = \frac{2Eht^3}{L} \quad (4.3)$$

Where E represents Young's modulus of the beam material, while h, t, and L correspond to the height, thickness, and length of the beam, respectively. For this specific design, the stiffness in the X direction is 69033 N/m, while in the Y direction, it amounts to 4.60 N/m.

To avoid side instabilities, it is crucial to maintain a significantly high stiffness ratio in the designed folded spring. The folded flexure design effectively diminishes the development of axial forces and extends the linear deflection range substantially. The stiffness ratio for small deflections equals that of a clamped-clamped beam.

The stiffness ratio, which represents the relationship between the stiffness in the lateral K_x and motion K_y directions, can be computed as follows:

$$\frac{K_x}{K_y} = \left(\frac{L}{t}\right)^2 \quad (4.4)$$

Maintaining a high stiffness ratio is essential to prevent lateral instabilities in the designed folded spring. Compared to other spring designs, the folded flexure design significantly reduces the generation of axial forces and provides a much larger linear deflection range for small displacements, equaling that of a clamped-clamped beam.

By combining the forces and deflections of the beam segments, the spring constant for the folded beam flexure due to lateral deflections can be calculated with the following equation:

$$K_x = \frac{200EI}{3L\delta_y^2} \quad (4.5)$$

This equation demonstrates that as the beam displacement in the y-direction increases, the spring constant in the x-direction diminishes. Consequently, the stiffness ratio also decreases with the increasing lateral beam deflection. The total spring constant comprises the series

connection of the lateral displacement-dependent spring constant from Equation (4.5) and the axial spring constant governed by Hooke's law.

4.2.2 Comb Drive Actuator

The actuation force necessary to deflect the folded springs is generated using a comb drive actuator. This actuator comprises two interdigitated comb-like structures that are charged with opposing voltages. However, due to the generation of a relatively small force, multiple fingers are employed to achieve the required force levels. The actuation force applied to deform the folded springs can be likened to a bending test for the silicon material. The electrostatic force produced by the comb drive under the influence of an actuation voltage (V) can be quantified using the following equation [122]:

$$F = n \frac{\epsilon_0 h}{g} \times V^2 \quad (4.6)$$

Where n is the number of fingers in the actuation comb drive, ϵ_0 is the permittivity of free space, h is the height of the comb drive fingers, and g is the gap between two neighboring fingers. For this design, the actuation comb drive has 240 fingers with a gap of $2 \mu\text{m}$, resulting in a force of $16.60 \mu\text{N}$ under an actuation voltage of 25 V .

The same comb drives used for actuation are also utilized for displacement and external force sensing via capacitive sensing. Neglecting parasitic capacitance, the change in capacitance (ΔC) in the sensing comb structures due to displacement of the probe stage (Δd) can be expressed as:

$$\Delta C = n \frac{\epsilon_0 h}{g} \times \Delta d \quad (4.7)$$

Where n is the number of fingers in the comb, ϵ_0 is the permittivity of free space, h is the height of the comb, and g is the gap between two neighboring fingers. For this design, n is 240 and g is $2 \mu\text{m}$, resulting in a capacitance change of 26.6 fF for a displacement of $1 \mu\text{m}$. The displacement (Δd) caused by the combs can be obtained by using the force-displacement relationship, which can be expressed as:

$$F = K_y \times \Delta d \tag{4.8}$$

Rearranged above equation:

$$\Delta d = \frac{F}{K_y} \tag{4.9}$$

Calculations based on equation 4.9, the comb drive is capable of generating a displacement of 3.608 μm when operated at 25 V.

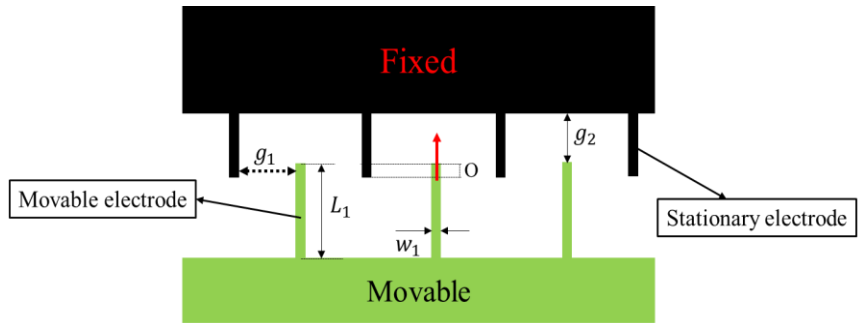


Figure 4.2: Schematic of parallel plate comb drive configuration.

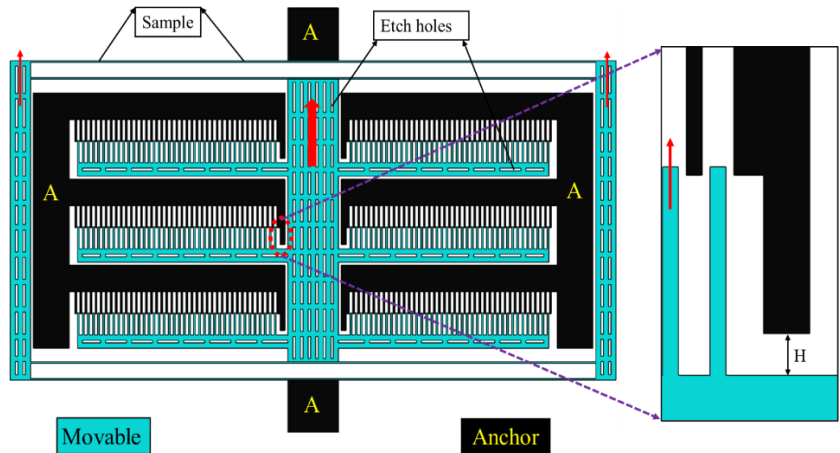


Figure 4.3: Schematic diagram of the MEMS electrostatic actuator.

Table .4.1: Geometrical parameters of the electrostatic actuator

Length of the spring beam (L)	612 μm
Width of the spring beam (w)	5 μm

Gap between the spring beams (g_3)	31.5 μm
Width of truss beam (w_2)	48 μm
Total number of combs (n)	240
Length of the comb (L_1)	50 μm
Width of the comb (w_1)	4 μm
Gap between movable and stator comb (g_1)	2 μm
Vertical gap (g_2)	48 μm
Hard limit space (H)	10 μm
Thickness (t)	25 μm

4.2.3 Static Structural Simulations

The finite element software Ansys® was used to perform 3D linear static structural simulations in order to verify the design of the electrostatic actuator device. The simulations were conducted with the aim of determining the maximum displacement and stress that the device could deliver motions at low operating voltages. The boundary conditions were set such that all the anchor points were mechanically fixed during the simulations while all other boundaries remained free to move. The simulations were conducted using silicon material parameters, with a Young's modulus of $E = 169 \text{ GPa}$ and a Poisson's ratio of $(\nu) = 0.28$, density $(\rho) = 2330 \text{ kg/m}^3$ [97]. A calculated force of $16.6 \mu\text{N}$ was applied to the movable combs at 25 V and resulted in a displacement of $3.65 \mu\text{m}$. The maximum stress observed in the simulation was 13.1 MPa , which was found to be in agreement with the analytical model with a difference of 2.2% , as shown in Figures 4.4-4.6. These results indicate that the designed electrostatic actuator device is capable of performing as intended and can withstand the maximum stress that it may encounter during operation. The simulation results also demonstrate that the analytical model used to design the device was accurate, making it reliable for experiments under in-situ microscopes.

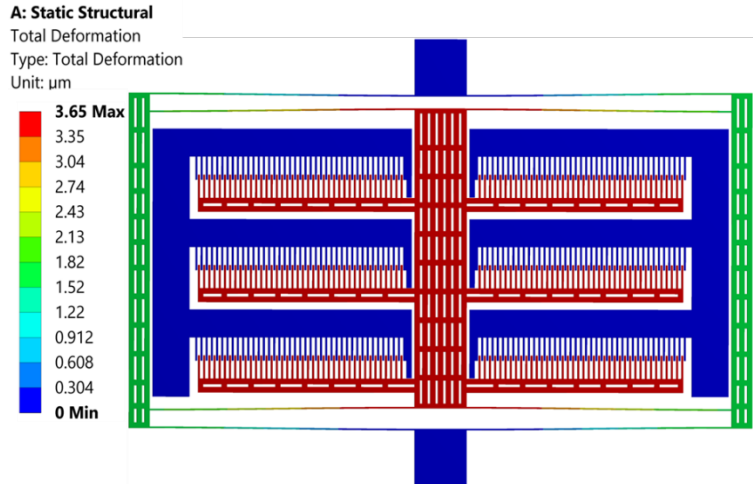


Figure 4.4 The maximum displacement achieved when a force of $16.6 \mu\text{N}$ is applied.

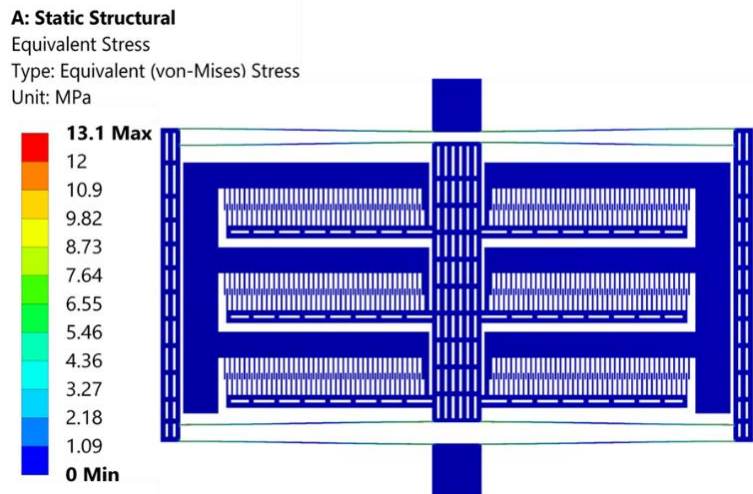


Figure 4.5: The maximum stress observed when a force of $16.6 \mu\text{N}$ is applied.

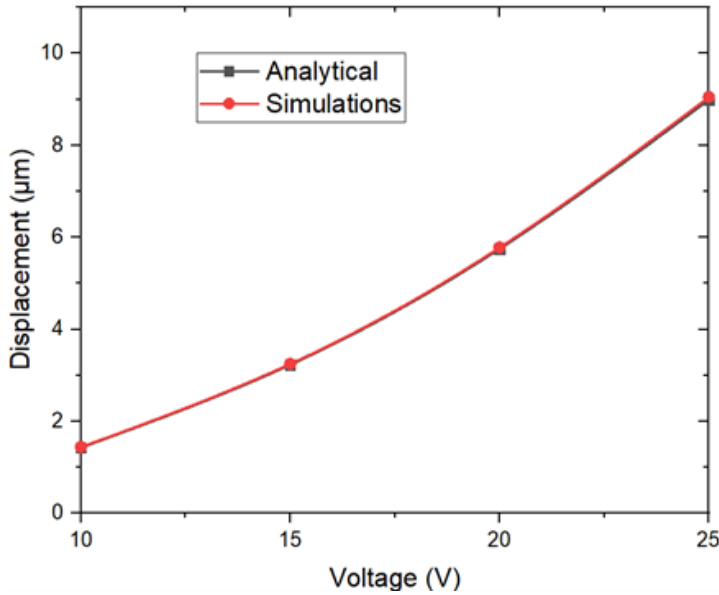


Figure 4.6: Comparison of analytical and simulation results.

4.3 MEMS Based Rotational Structures

Microelectromechanical Systems (MEMS) have revolutionized the field of sensors, actuators, energy harvesters, switches, and microgrippers by enabling the integration of mechanical and electrical components on a microscale [123]. Over the years, researchers have made significant strides in improving the precision and size of MEMS devices. In common MEMS actuators, electrical signals are converted into mechanical displacement leading to a change in capacitance or resistance. However, these changes are often small and require amplification mechanisms to improve the sensitivity of the device [97], [124]. Amplifying the displacement is a critical aspect of MEMS technology, especially in applications where a large movement or change in capacitance is necessary [125]. Different mechanisms have been proposed in [97], [123], [126] to amplify displacements for sensors and stress diagnosis applications. For example, the measurement of stress is a crucial factor in optimizing residual stresses left by microfabrication processes. In this regard, several measurement techniques have been developed, including traditional array structures and MEMS-based rotational structures [126]–[129]. The rotational structures, in particular, have been widely utilized in stress

measurements due to their several advantages over other measurement techniques. One of the main advantages of rotational structures is their ability to measure both tensile and compressive stresses with a continuous readout. This feature is important as it enables the characterization of the stress distribution in real-time. Moreover, rotational structures provide higher resolution measurements compared to traditional array structures such as buckling beams [126]. Additionally, the MEMS-based fabrication technology used in rotational structures enables them to occupy limited area on the wafer, which makes them more suitable for high-density integration. Furthermore, rotational structures have the ability to directly amplify displacement with consequent sensitivity enhancement, making them more suitable for stress measurements in small devices [127], [128]. However, despite their advantages, rotational structures also have certain limitations. For instance, they may not achieve a large displacement with a smaller input force, and they are more vulnerable to breakage due to localized stress [126].

Rotational structures have been developed using two main fabrication techniques: surface micromachining and bulk micromachining [126]–[130]. Surface micromachining is a well-established process for the fabrication of MEMS structures using thin films by low-pressure chemical vapor deposition. The films are etched and patterned to form the desired device structure. However, the residual stress in these thin films can be high, leading to buckling or cracking of the structures when released. To mitigate this issue, various stress-reducing techniques have been developed, such as the use of multilayer thin films, post-deposition annealing, and the introduction of stress-relief structures [130]. On the other hand, bulk micromachining involves the deep etching of substrate material (usually silicon) to form the desired device structure. This process provides a more rigid and stable structure compared to surface micromachining, as the mechanical properties of single-crystal silicon are superior. In bulk micromachining, the deep etching process can be anisotropic, allowing for the creation of vertical structures with precise control over the dimensions and shapes. The choice between surface and bulk micromachining for the fabrication of MEMS rotational structures depends on the requirements of the specific application. Surface micromachining is a versatile and cost-effective method, while

bulk micromachining offers better mechanical properties and reduced residual stress issues [131], [132].

There are some limitations to surface micromachining fabrication process that can lead to device failure. For example, limited displacements and residual stresses make devices more prone to breakage. However, in our research, a novel mechanism has been proposed that overcomes these limitations. To achieve this, we turned to bulk micromachining process with silicon on insulator (SOI) wafers. SOI wafers consist of a single crystal silicon layer on the top, an insulating layer, and a handle layer on the bottom [133]. The use of SOI wafers has several advantages over traditional silicon bulk substrates. Firstly, SOI wafers exhibit lower residual stresses in the structural layer, resulting in higher quality and reliability. Secondly, the insulating layer provides an excellent etch stop, simplifying the fabrication process. Thirdly, the isolation of the single crystal layer from the bulk substrate leads to lower parasitic capacitances, enabling high-speed devices with lower power consumption. Finally, the complete isolation of n-well and p-well devices in the SOI wafers provides protection against latch-up effects and enhances the radiation hardness [134], [135].

In the current research, a novel MEMS-based rotational structure is introduced, capable of providing amplified output displacement compared to traditional designs. The proposed mechanism leverages the advantages of SOI wafers, offering a high-quality, reliable, and efficient solution to overcome the limitations of conventional rotational structures.

4.3.1 Mechanical Design of the C-Shaped Rotational Structure

This study considers two distinct MEMS rotational structures: the symmetric lancet design, resembling previously published structures in the literature, and the original C-shaped rotational structure. Both structures, as depicted in Figure 4.7, consist of interconnected components collaborating to generate rotational motion. These components encompass a double set of opposed thermal actuators (chevron beams), a rotational mechanism, a straight beam, and a tilted arm. The straight beam and rotational mechanism facilitate smooth and efficient rotation of the tilted arm.

Both MEMS rotational structures employ thermal actuators as the input source for force and displacement. The literature offers various driving devices capable of generating displacements, including electrostatic, piezoelectric, electromagnetic, and electrothermal actuators, each with their unique advantages and disadvantages. The selection of the optimal driving mechanism hinges on specific application requirements such as force output, displacement range, cost, and size. For instance, electrostatic actuators deliver high force but limited displacement, whereas piezoelectric actuators provide high force density and substantial displacement but tend to be relatively costly. Electromagnetic actuators can generate significant forces and displacements but may require magnetic fields and can be bulky. In contrast, electrothermal actuators utilize thermal expansion due to electrical current flow, resulting in substantial force generation and multi-directional actuation. Their advantages include fast response times, high force-to-volume ratios, and low power consumption.

In the MEMS rotational structures, activating a thermal actuator initiates linear motion transferred to the central shuttle and straight beam. The rotational mechanisms then convert this linear motion into rotational motion, suitable for various microelectromechanical applications. Integration of thermal actuators on both sides of the central shuttle and straight beam enables precise control over the rotational displacement, making MEMS rotational structures ideal for microscale systems requiring precise motion control.

The design of the rotational mechanism significantly influences the overall performance of the rotating MEMS structure. The design parameters for the symmetric lancet MEMS rotational structure were drawn from existing literature, while the C-shaped MEMS rotational structure was optimized using the design of experiments (DOE) method and analytical modeling. The optimization process involved systematic testing of various design combinations to determine the optimal configuration for the C-shaped structure, considering specific application requirements and fabrication constraints.

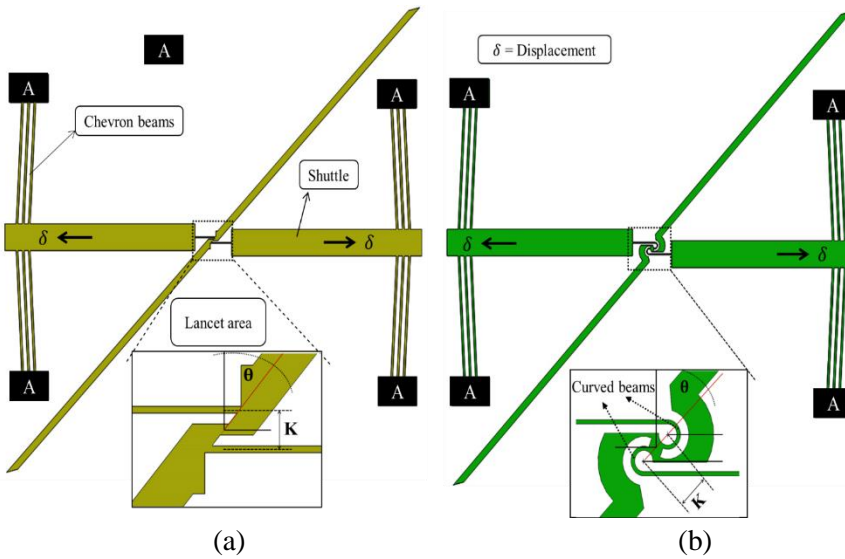


Figure 4.7: Schematics of two investigated MEMS rotational structures: (a) symmetric lancet and (b) symmetrical C-shape.

To optimize the C-shaped structure's parameters, Design of Experiments (DOE) served as a valuable statistical tool for analyzing and enhancing complex designs. DOE facilitates the identification of relationships between independent variables (factors) and dependent variables (responses). It aids in identifying the most influential factors affecting system performance and interactions while maximizing efficiency and effectiveness. Various methods, including one-factor, factorial design, robust parameter design, and reliability design, offer diverse approaches and levels of detail for improving system output responses.

For the novel MEMS rotational structure, the Response Surface Method (RSM) in combination with Central Composite Design (CCD) through JMP® statistical software was employed to optimize the design parameters. RSM is a widely adopted technique for modeling the relationship between a response and multiple independent variables. This study concentrated on two vital independent variables: curved beam width (W) and the gap (K) between the upper and lower curved beam centers of rotation. Three levels were considered to identify optimal values for these variables: low (-1), medium (0), and high (+1). Based on fabrication constraints, the low and high levels for W were set

at 2.3 μm and 6 μm , respectively, with an intermediate level at 4.5 μm . Similarly, the low and high levels for K were 15 μm and 30 μm , with an intermediate level at 22.5 μm (Table 4.2). The combination of RSM and CCD enabled a comprehensive exploration of how independent variables influenced the response and facilitated the determination of optimal design parameters for the structures.

DOE results established the model's statistical significance, with a p-value less than 0.05. Notably, the minimal gap between the two curved beam centers of rotation and a narrower hinge width had the most significant impact on output displacements, as evidenced in Table 4.3. Specifically, variations in curved beam width (W), while keeping other parameters constant, had the most substantial influence on output displacement. Additionally, it was observed that the combination of curved beam width (W) and hinge gaps (K) had a secondary influence on the output performance, highlighting the significance of these specific design factors in determining the device's overall performance.

Table 4.2: Design (CCD) matrix and signs with input variables and output response.

Observations	Treatments	Factor W (μm)	Factor K (μm)	Displacement (μm) at 1 V
1	--	2.3	15	6.2
2	+-	6	15	2
3	-+	2.3	30	5.3
4	++	6	30	2.6
5	0 a	4.5	15	3.5
6	0 A	4.5	30	3.8
7	a 0	2.3	22.5	6
8	A 0	6	22.5	2.5

Table 4.3: Effect test results from JMP® statistical software.

Factor	Degree of freedom	Sum of squares	F-ratio	P-Value (<0.05)	Significance
W	1	17.6	814	0.001	Yes

K	1	0.007	0.34	0.62	No
W, K	1	0.497	22.9	0.04	Yes
W, W	1	0.232	10.7	0.08	No
K* K	1	0.023	1	0.4	No

Figure 4.8 presents a performance analysis of an symmetrical C-shape rotational structure, examining the effects of variations in curved beam width (Figure 4.9a) and the gap between the curved beam's center of rotation (Figure 4.9b). These findings are consistent with the observations made from the DOE analysis presented in Table 4.3. As it can be observed, both parameters have an influence of the system response, with the displacement increasing when both the width of the curved beam and the gap between the centers of rotation are reduced. In particular, the best performance is achieved when $W=2.3 \mu\text{m}$ and $K=14.6 \mu\text{m}$, which correspond the values used for the device fabrication. However, these two parameters are also subject to fabrication limitations, which must be considered when determining the desired displacement specifications. As a result, a tradeoff must be made between the desired displacement specifications and the fabrication limitations, to ensure that the final output meets the desired specifications within the constraints of the fabrication process.

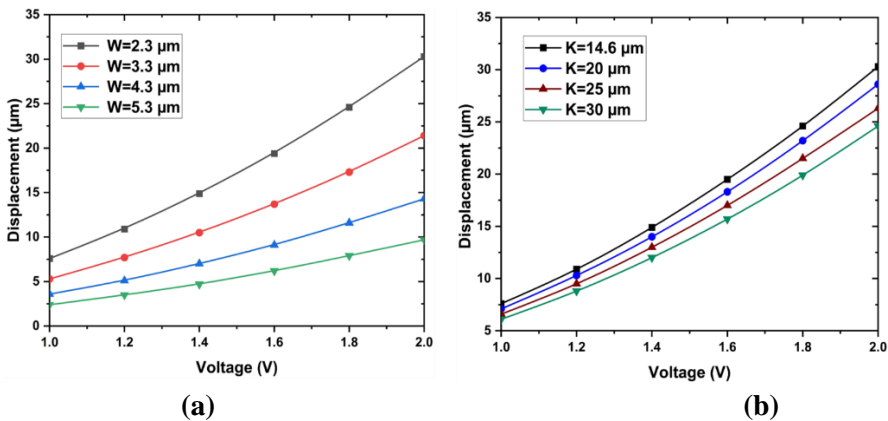


Figure 4.8. Performance analysis of symmetrical C-shape rotational structure: dependence of the output displacement on (a) the curved beam width and (b) the gap between hinges center of rotations.

4.3.1 Analytical and Numerical Modelling

To model the behavior of the C-shaped rotational structure, considered a simplified version due to its inherent symmetry, as depicted in Figure 4.9b. This simplified structure comprises a straight beam (AB) with a length (x_s), connected to a curved beam (BC) with a radius (R). The curved beam is further connected to a rigid element (DC) of a specific length. We can assume specific boundary conditions, such as a slider at point A, representing the presence of the thermal actuator responsible for horizontal displacement and force. At point D, a hinge allows free rotation of the structure. The rigid beam (DC) plays a crucial role in precisely locating the center of rotation for the simplified model in relation to the overall structure.

Table 4.4 provides an overview of all the geometric parameters utilized in the analytical modeling of the curved beam. The selection of the curved beam width (W) was informed by fabrication constraints and the findings from the DOE analysis, ensuring optimal performance. Meanwhile, the straight beam length (x_s), curved beam angle (θ_1), and rigid beam length (x_r) were determined through analytical calculations.

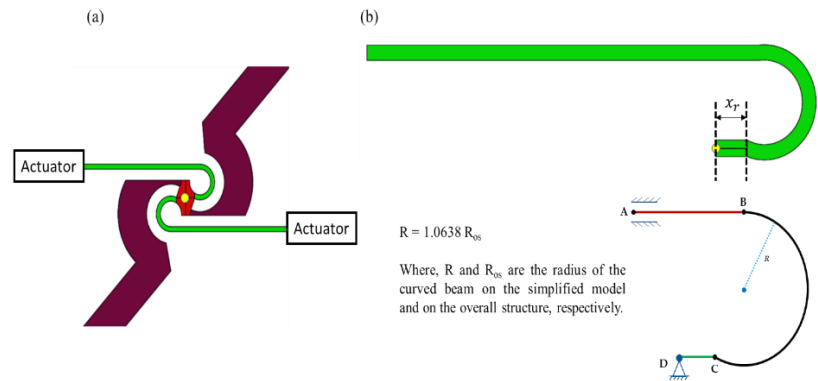


Figure 4.9: Schematic diagram of symmetrical C-shape structure (a) and simplified curved beam structure for analytical model (b).

Table 4.4: Geometrical parameters of curved beam.

Angle (θ_1)	34°
$\alpha = \pi + \theta_1$	214°

<i>Radius</i>	7.5 μm
<i>Width</i>	2.3 μm
Straight beam length (x_s)	65.5 μm
Rigid beam length (x_r)	5.3 μm

Castigliano's second theorem was applied to compute the horizontal displacement of the straight beam, which serves as the input to the system, based on the force exerted by the thermal actuator. This theorem establishes that for linearly elastic structures, if the strain energy of such a structure can be represented as a function of the generalized force, F_i , then the generalized displacement, δ_i , in the direction of F_i can be determined as the partial derivative of the strain energy, U , concerning the generalized force, F_i [136]:

$$\delta_i = \frac{\partial U}{\partial F_i} \quad (4.10)$$

Considering Figure 4.9, the moments along the straight ($M(x)$) and curved ($M(\alpha)$) beams can be expressed as follows:

$$M(x) = R_A^{(0)} x_s + Y \left(-R_A^{(1)} x_s + 1 \right) \quad (4.11)$$

$$M(\alpha) = -F_A R (1 - \cos \alpha) + R_A^{(0)} x_s + R_A^{(0)} R \sin \alpha Y \left(-R_A^{(1)} R \sin \alpha - R_A^{(1)} x_s + 1 \right) \quad (4.12)$$

The strain energy can be obtained as follows [137]:

$$U = \int_0^{x_s} \frac{M(x)^2}{2EI} dx + \int_0^\alpha \frac{M(\theta)^2}{2EI} R d\theta \quad (4.13)$$

Substituting equations (4.11) and (4.12) into equation (4.13) and considering the geometric values from Table 4.4, the strain energy simplifies to:

$$U = \left(\frac{8520.1727 F_A^2}{2EI} \right) = 0.0009944 F^2$$

Ultimately, the displacement at point A can be computed using equation (4.10):

$$\delta_A = \frac{\partial U}{\partial F_A} \tag{4.14}$$

This results in $\delta_A = 0.001989 F_A$.

Working through the integrals outlined in equation (4.13) and computing the derivative with respect to force (equation 4.14) allows the derivation of an analytical expression illustrating how δ_A varies in relation to different geometric parameters, including the width and radius of the curved beam, straight beam length, and curved beam angle. For instance, Figure 4.10(a) illustrates the correlation between the curved and straight beam widths and the horizontal displacement at the straight beam's tip. The findings reveal that as the beam width increases, the displacement decreases, reaching its maximum value at a beam width of 2.3 μm , consistent with the results from the previous section on DOE analysis.

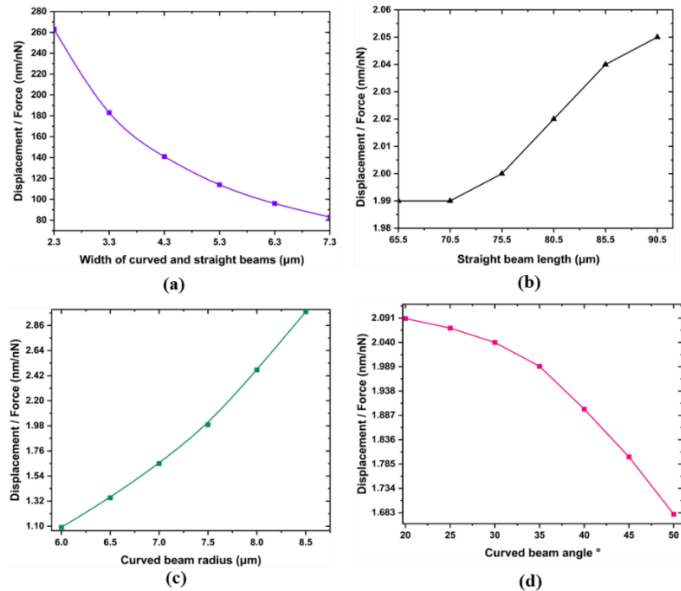


Figure 4.10: Investigating the impact of symmetrical C-shape geometry on the displacement at the beginning of the straight beam determined from the analytical model based on Castigliano’s theorem: (a) curved and straight beams width study of (a) Widths, (b) Length, (c) Radius, and (d) Angle.

In Figure 4.10(b)-(d), the horizontal displacement at the straight beam's tip is presented as a function of the straight beam length, as well as the radius and angle of the curved beam. These plots reveal that, as the straight beam length increases (especially beyond 70.5 μm) and the radius of the curved beam expands, the displacement exhibits a nearly linear rise. Conversely, an increase in the angle of the curved beam leads to a notable reduction in displacement.

The selection of an optimum angle, curved beam radius, and curved beam width is crucial as it can significantly enhance the displacement of symmetrical C-shape structures for specific applications. A wider beam has higher stiffness and smaller deflection than a narrower beam under the same loading conditions, improving overall stability. This study provides valuable information on the relationship between “angle, radius, width of curved beams and displacement”, which can serve as a benchmark for prospective designs. Therefore, it is imperative to consider the optimal selection of these parameters when designing a symmetrical C-shape structure.

Figure 4.11 showcases the results of Ansys® finite element analysis, using equation (4.13) and static structural simulations to predict the behavior of the symmetrical C-shaped structure. The maximum difference between the analytical and simulation results was found to be 2.3% at 5 μN load, which is relatively small and suggests that both approaches are accurate in predicting the behavior of the structure. However, it should be noted that the accuracy of both approaches depends on the assumptions made and the level of detail included in the model. Therefore, a combination of both approaches may be necessary to achieve the most accurate predictions of complex systems.

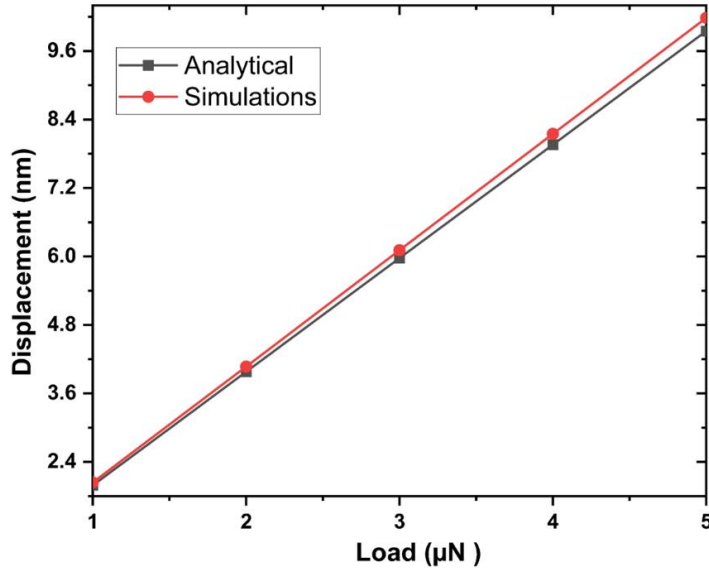


Figure 4.11: Comparison between the horizontal displacement at the beginning of straight beam obtained from analytical modeling and numerical simulations as a function of the force delivered by thermal actuators.

A coupled linear Multiphysics simulations were conducted on two distinct rotational structures: the novel C-shaped design and the symmetrical lancet design (used for comparison). These simulations were performed using Ansys® finite element software in thermal-electric-structural interaction mode.

For structural boundary conditions, the actuator anchors were kept mechanically fixed, allowing all other boundaries to remain free to move. In terms of thermal boundary conditions, a constant temperature (22 °C) was maintained on the faces in contact with the substrate. In the electrical domain, a DC voltage was applied between the actuator anchors (contact pads). These simulations produced output data for both temperature and displacement fields of the MEMS rotational structures.

The application of voltage across the anchors generated heat due to joule heating, which dissipated until it reached a steady state of heat balance. Because of the heat dissipation path through the anchors within a vacuum, the highest temperatures were observed in the shuttle area, farthest from the anchors, resulting in non-uniform temperatures.

Consequently, this non-uniform temperature distribution also led to non-uniform displacement within the device, as depicted in Figure 4.12.

The specific dimensions used in the simulations are detailed in Table 4.5, while Table 4.6 provides the silicon material properties employed in the simulations. Notably, the lancet and symmetrical C-shape MEMS-based rotational structures shared identical characteristics, including width, thickness, length, number of chevron beams in the thermal actuators, straight beam and tilted arm geometry, shuttle lengths, and rotational hinge angles.

Table 4.5. Geometrical parameters of MEMS rotational structures.

Actuator beam length	300 μm
Actuator beam width	4.7 μm
Actuator beam angle θ°	3
Total number of beams	6
Device Thickness	25 μm
Straight beam length	49 μm
Straight beam width	2.3 μm
Curved beam width	2.3 μm
Curved beam radius	3.3 μm
Curved beam angle (θ)	34 $^\circ$
Gap (K)	14.6 μm
Tilted arm lengths	780, 787 μm
Tilted arm Width	16.7 μm

Tale 4.6. Silicon properties [96].

Youngs Modulus (E)	169 GPa
Poisson's ratio (ν)	0.28
Density (ρ)	2330 kg/m^3

Thermal conductivity (K)	130 [W/(mK)]
Coefficient of thermal expansion (α)	$2.6 \times 10^{-6} \text{ K}^{-1}$
Resistivity	0.005 $\Omega \text{ cm}$

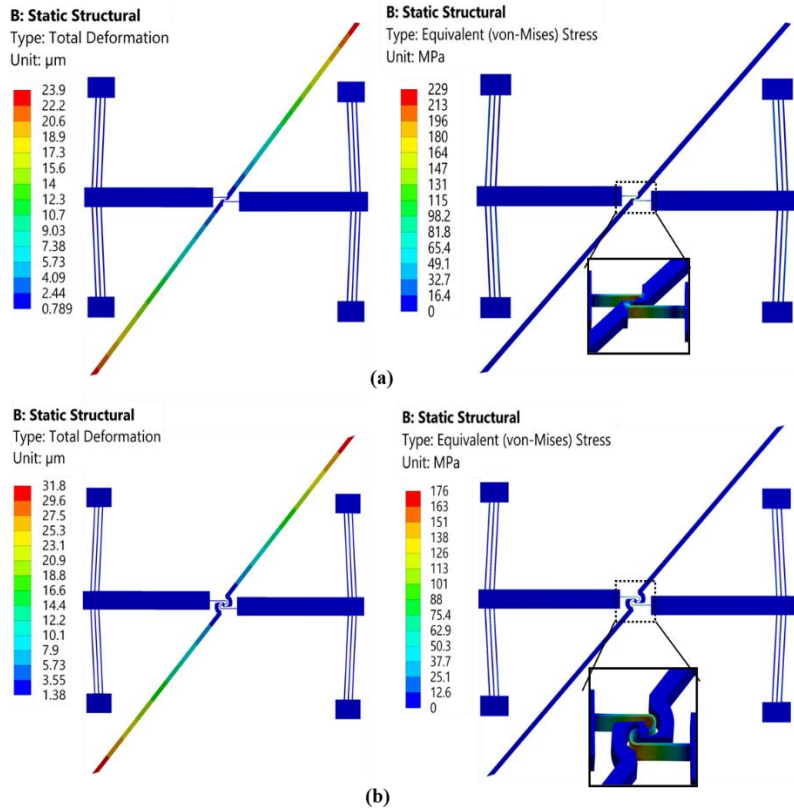


Figure 4.12. The maximum displacement and stress when the actuators are biased with 2V in symmetrical C-shape (a) and symmetrical lancet structure (b).

The results, shown in Figure 4.12, provide insights into the stress distribution and displacement of both MEMS rotational structures when subjected to a 2 V applied voltage.

The symmetric lancet structure, as demonstrated in Figure 4.12 (a), showcased a maximum displacement of 23.9 μm along with a stress value of 229 MPa under the same conditions. In contrast, the

symmetrical C-shape structure, presented in Figure 4.12 (b), outperformed with a higher output displacement of 31.8 μm and a lower stress level of 176 MPa under the same actuation voltage.

The chapter 5 provides an introduction to the various fabrication technologies employed in the fabrication of silicon micromechanical devices. It begins with a comprehensive overview of microfabrication and its associated processes. Special emphasis is placed on the specific microfabrication methods used in the present research. The chapter further delves into the intricate details of the fabrication process involved, particularly in the context of generating complex structures. The chapter goes into much more information about the fabrication process followed in the current research.

5.1 Introduction

Microfabrication is the process of fabricating tiny devices or structures on a micrometer or nanometer scale. Silicon has become one of the most commonly used materials in microfabrication due to its availability, well-characterized properties, and compatibility with mature and easily accessible processing techniques. It can be integrated with control and signal processing circuitry, making it a suitable material for mechanical sensors and other MEMS devices. Crystalline silicon has a face-centered cubic lattice with two atoms associated with each lattice point, and the $\{100\}$ and $\{111\}$ planes are the most commonly used orientations for microfabrication. The orientation of the silicon needs to be considered in the design of any mechanical sensor, and wafers are typically cut to form a primary flat in a $\{110\}$ plane and a secondary flat to identify the wafer orientation and doping type. The properties of crystalline silicon can vary depending on its orientation, and this needs to be considered in the design and fabrication of microdevices. For example, the piezo resistance coefficient of single crystal silicon depends on the orientation of the resistor with respect to the crystal orientation, and Young's modulus is also orientation dependent. Cracks initiated through mechanical loading will tend to propagate along certain crystal planes. However, these properties make silicon an ideal material for fabricating MEMS devices. The high Young's modulus, low coefficient of thermal expansion, and excellent thermal conductivity of silicon make it suitable for MEMS applications such as accelerometers, pressure sensors, gyroscopes, and micro actuators [138], [139].

Furthermore, silicon is a well-established material in the integrated circuit industry, which has led to the development of a large number and variety of mature, easily accessible processing techniques for silicon-based MEMS fabrication. Surface micromachining and bulk micromachining techniques can be used to create complex three-dimensional structures on a micron or nanometer scale. The combination of silicon's properties and the available processing techniques make it the most widely used material in MEMS fabrication [140].

5.1.1 Surface and Bulk Micromechanics

When it comes to silicon micromechanics, two main categories, surface micromechanics and bulk micromachining, have been developed to leverage the material's properties for MEMS fabrication. Surface micromechanics involves the creation of thin films, often of LPCVD (Low-Pressure Chemical Vapor Deposition) polycrystalline silicon, on a silicon wafer's surface. Silicon dioxide frequently serves as the sacrificial layer, with the overall thickness of the film stack typically not exceeding a few micrometers. This process sequence involves depositing and patterning a sacrificial oxide layer, followed by the deposition and patterning of the structural polysilicon layer. Upon completion of these steps, the structure is freed by etching away the sacrificial layer underneath. Despite the inherent challenges, such as the control of internal film stress, polysilicon surface micromachining has proven useful for creating various MEMS devices, including motors, resonators, and varactors.

In contrast, bulk micromachining utilizes the silicon wafer material itself to create devices, typically through etching techniques. The thickness of the structures can match the wafer's thickness, with anisotropic wet etching, typically using KOH (Potassium Hydroxide), EDP (Ethylene Diamine Pyrocatechol), or TMAH (Tetramethylammonium Hydroxide) solutions, being the method of choice. However, design constraints from inclined sidewalls and excessive silicon surface consumption often result in pyramidal shapes or V-grooves on a <100>-oriented silicon wafer.

5.1.2 SOI Micromechanics

Silicon on Insulator (SOI) technology provides a unique avenue for microfabrication, catering primarily to high voltage, latch-up free, and radiation-hard integrated circuits. This technology is implemented using SIMOX (Separation by Implantation of Oxygen) or newer layer transfer methodologies, which result in relatively thin oxide and structure layers. The fabrication advantages of SOI are plentiful, thanks to the buried oxide layer's function as a selective stop layer and the ability to structure the top and bottom silicon independently. SOI micromachining offers the capability of fabricating structures with standard lithography and deep reactive ion etching (DRIE). Compared to traditional bulk micromachining, SOI provides effective electrical isolation, good availability of the etch stop layer, and a broader range of achievable shapes through dry etching. An added advantage is that the thickness of the structure can be tuned by selecting an appropriate top silicon thickness. Silicon fusion bonding (SFB), a method for creating SOI wafers, involves bonding two wafers together without external pressure, followed by a high-temperature annealing process. Subsequently, one of the wafers is ground or etched down to the desired thickness and polished. SFB has proven beneficial for a wide range of applications, including accelerometers, pressure sensors, and other MEMS devices, due to the high aspect ratio structures it can produce, the flexibility of the oxide layer, and the ability to fabricate MEMS devices requiring flat, stiff surfaces.

5.2 Fabrication Technologies

The fabrication of microelectronic devices necessitates the systematic repetition of several fundamental processing steps. Each step must be followed by rigorous cleaning of the wafers to eliminate potential contaminants that might impact subsequent procedures. Such contaminants could include residual organic and inorganic particles, as well as solvents. A conventional cleaning technique known as RCA (Radio Corporation of America) is generally employed. This technique cycles between surface oxidation, oxide stripping, rinsing, and drying phases to effectively clean the wafers. Cleanroom environments are classified according to the permissible number of particles ($0.5\mu\text{m}$ or

larger) per cubic foot. For instance, a Class 100 cleanroom permits a maximum of only 100 particles smaller than 0.5 micrometers per square foot. The cleanliness grade required depends on the specific type of devices under production and their smallest feature size. Following the cleaning phase, the primary processing steps are executed in the order of deposition, patterning, photolithography, and etching. During the deposition step, a thin layer of material is applied to the wafer. Various techniques like chemical vapor deposition (CVD), sputtering, or evaporation can be utilized for this purpose. In the patterning phase, a specific design is created on the surface of the deposited material. This design is typically made using a mask, generally constructed from a material such as chrome. Photolithography, which uses a photo-sensitive resist material, is then employed to transfer this pattern onto the wafer. Etching represents the next stage, which involves the removal of material from the wafer using chemical or plasma methods. Dry etching techniques, such as reactive ion etching (RIE), utilize plasma to remove material, while wet etching employs chemicals to dissolve the material. Upon completion of etching, the wafer is subjected to another cleaning process to eradicate any remaining residues, paving the way for the next processing step. The required cleanliness class is determined by the kind of devices being produced and their smallest feature size. This sequence of fundamental processing steps is reiterated multiple times until the desired device structure on the wafer is achieved.

5.2.1 Deposition Technology

The deposition process is a fundamental stage in the fabrication of MEMS or NEMS (Nano-Electro-Mechanical Systems) devices. It involves forming a thin layer of solid-state material on the substrate, imparting it with certain structural or functional attributes. A range of deposition methods exists, including Physical Vapor Deposition (PVD), Chemical Vapor Deposition (CVD), electrochemical deposition, and Plasma-Enhanced Chemical Vapor Deposition (PECVD). Both PVD and CVD are dry deposition processes conducted in vacuum conditions. In PVD, the source atoms are coerced into a gaseous phase via physical processes such as thermal evaporation or ion sputtering. In contrast, CVD forms a thin film via chemical reactions among gaseous precursors. Hybrid deposition procedures can also be

employed, which amalgamate the physical and chemically reactive effects. Thermal PVD, typically achieved through thermal evaporation, entails transitioning a solid or molten source material into a gaseous state and condensing it onto a substrate within a vacuum chamber. Ensuring film thickness uniformity is vital in this process and hinges on factors like the properties of the evaporation source and the substrate's position and orientation within the vacuum chamber. Plasma PVD, or sputtering, is an alternative technique for thin film deposition. It involves the bombardment of a target with energetic ions, leading to the ejection of atoms from the solid, which then condense onto a substrate, as depicted in Figure 5.1. Typical conductive layer materials include Au, Cu, and Al, while TaN serves as a resistive layer. Barrier and adhesion layers commonly utilize TiW, Pt, Mo, NiCu, Cr, Ti, and TiW. Electrochemical or chemical deposition, on the other hand, immerses the substrate in an electrically conductive fluid to form a conductive metal film. Electrochemical deposition, also known as electroplating, necessitates an external current source and is often applied in photolithography micromolds for through-mask deposition.

PECVD is a process that encompasses the collision of precursor species with plasma-generated charged particles, resulting in the electron impact dissociation and excitation of the precursor species, thus producing highly reactive species. The first commercially available PECVD reactor, introduced in 1974, employs a parallel-plate design, as illustrated in Figure 2. In comparison to thermal activation, the activation energy required for a plasma process is lower, translating into a higher deposition rate. Nevertheless, a certain amount of heat is essential to overcome the activation energy, which also aids surface reactions, reduces film contamination and absorption, and improves surface migration. The deposition process plays a significant role in defining the ultimate properties of MEMS or NEMS devices. Consequently, the choice of deposition techniques should consider the aspired characteristics of the film, including its composition, thickness, uniformity, adhesion, as well as mechanical and electrical properties. It's also important to ensure the compatibility of the deposited layer with the subsequent processing steps such as patterning and etching.

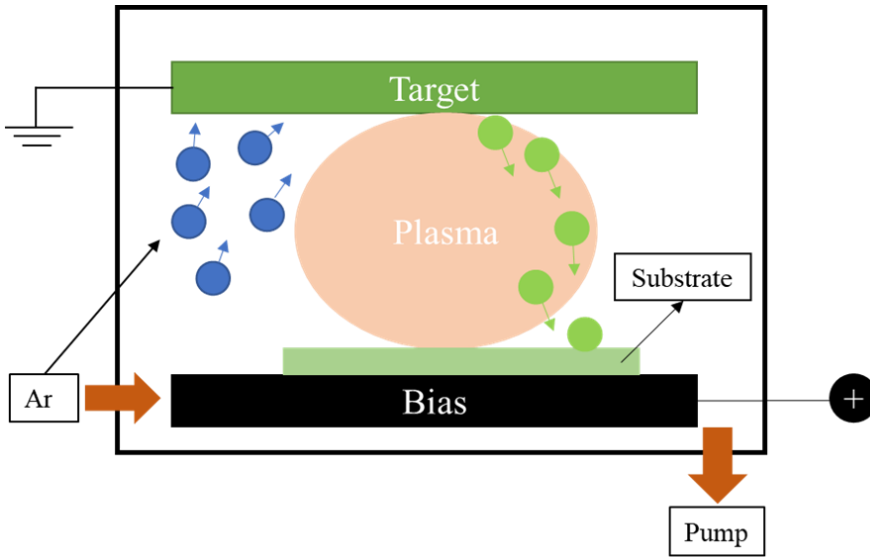


Figure 5.1. A schematic representation showing the standard sputtering technique [138].

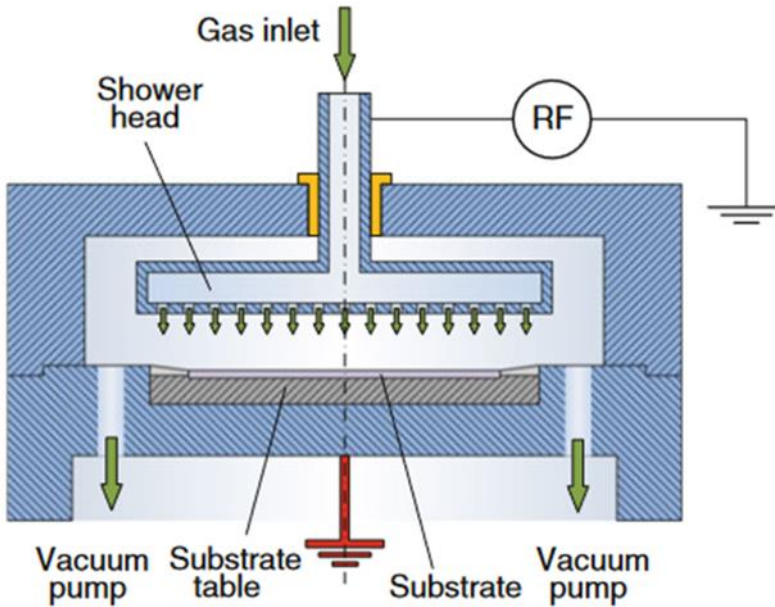


Figure 5.2. Schematic representation of a parallel plate PECVD reactor [141].

5.2.2 Patterning Technology

In microfabrication of MEMS devices, patterning is one of the crucial step in the cleanroom, and it is predominantly conducted by photolithography. This process is essential for precise patterning of deposited layers and is widely used in microelectronics and MEMS fabrication. The most commonly used method for lithography is photolithography, which involves transferring a pattern onto a wafer coated with a photosensitive material or photoresist using a mask. The photolithographic process consists of four main components: photomask, optical projection system, photoresist, and substrate. The photomask is a physical mask with a defined pattern that is used to create the desired shape on the substrate. The optical projection system is used to transfer the pattern from the mask to the photoresist-coated substrate. Photoresist is a photosensitive material that changes its chemical properties when exposed to light. The substrate is the material onto which the pattern is transferred. The photolithographic process typically involves several steps, including depositing photoresist, exposing the photoresist to light through the mask, developing the photoresist to remove the unexposed regions, transferring the pattern to the substrate, and removing the photoresist to define the feature accurately. Each step is crucial and requires attention to detail to ensure the desired pattern is achieved. The deposition of the photoresist involves placing a small amount of liquid photoresist on the substrate and spinning it to create a thin, uniform layer. The photoresist is then exposed to light through the mask in a process known as photomasking. The exposed regions of the photoresist become more soluble in the developer solution, which allows for the removal of the unexposed regions of the photoresist during the developing process. After the photoresist is developed, the pattern is transferred to the substrate using an etching process, which involves removing the exposed or unexposed regions of the substrate material. In the end, the remaining photoresist is removed from the substrate, leaving behind the patterned features [142].

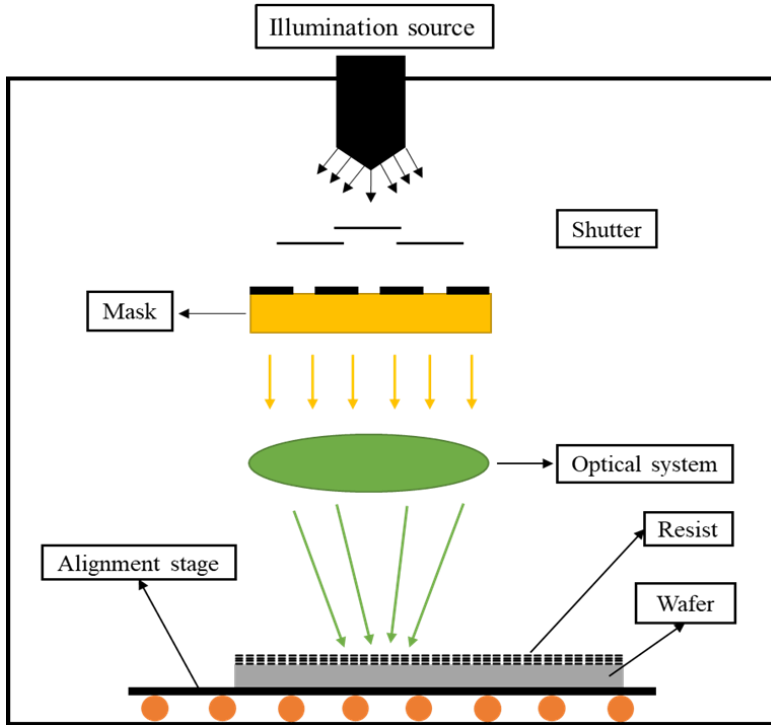


Figure 5.3: Schematic of lithography system [142].

The performance of lithographic processing is measured using three key metrics: resolution, registration, and processing throughput. Resolution, which is the ability of the lithographic system to distinguish between closely spaced features, is closely tied to the wavelength of the illumination source. As lithography equipment has evolved, the wavelength of the illumination source has decreased from the visible spectrum to ultraviolet (UV) and, more recently, to extreme ultraviolet (EUV).

The design of the optical system of the lithographic equipment is complex and involves several key parameters. One of these parameters is the minimum line width (W_{\min}), which is the smallest feature size that can be accurately patterned. The equation for W_{\min} is similar to the Raleigh criteria for optical resolution and depends on several factors, including the intensity of the illumination source, the ability of the photoresist to distinguish changes in width (K), and the numerical aperture (NA) of the optical system [143].

$$W_{min} = K \frac{\lambda}{NA} \quad (5.1)$$

Equation 5.2 defines the numerical aperture as a relationship between the refractive index, represented by "n," of the medium situated between the objective and wafer, and the half angle of the image, denoted by " α ." This means that the numerical aperture is influenced by both the refractive index and the angle of the image. Mathematically, this can be expressed as:

$$NA = n \sin \alpha \quad (5.2)$$

Another important parameter in the design of the lithographic system is the depth of focus (σ), which is the range of heights at which the lithographic process can accurately expose the photoresist. The depth of focus is critical in MEMS fabrication due to the thickness of the films involved and the possible warpage of the wafer due to residual stress. The equation for σ depends on the wavelength of the illumination source and the numerical aperture of the optical system:

$$\sigma = \frac{\lambda}{NA^2} \quad (5.3)$$

Masks are another important component of the lithography process, as they contain the patterns that need to be etched into the material to implement the MEMS design. Masks can be the same size (1:1) as the patterns to be transferred or larger (1 \times , 5 \times , or 10 \times) depending on the lithographic system. Masks are typically made of materials that are transparent at the illumination wavelength, with the patterns defined by an opaque material. Masks need to be very flat and insensitive to changes in temperature to prevent degradation of the lithographic image. Contamination control is also an important issue in the lithography process. For example, masks may have a pellicle membrane held above the patterned area to keep particles off the mask surface and out of the image plane of the mask. Photoresist consists of three components: a resin material, a photoactive compound, and a solvent. These components affect the durability, sensitivity, and viscosity of the photoresist, respectively, and must be carefully controlled to ensure high-quality patterning.

These masks are made up of areas that either allow light to pass through or block it. They're typically created from materials that are transparent to ultraviolet (UV) light but have specific patterned designs made of a metal film, like chromium. Photomasks can be used in two ways, either to allow light to pass through (light field) or to block it (dark field). There are different types of photolithography masks, including contact, soft-contact, and proximity masks, which create a 1:1 image. However, these masks can get easily worn or contaminated. On the other hand, projection lithography masks, also known as reticles, are designed to create smaller images (1:4, 1:5, or 1:10) on the photoresist layer. They're more durable and are great for large-scale production.

Standard projection masks are diffraction-limited, but optical interference effects can be engineered into the mask to overcome diffraction limitations. This can be done by changing the thickness of a transparent region of the mask (alternating phase-shift) or increasing the transmittance of the originally opaque region of the mask (attenuated phase-shift). Pixelating an originally opaque region of the mask is another way to modify a standard projection photomask, and these styles of masks are used for grayscale lithography. The typical thickness of a chromium film used in a photomask is 800 Å. In photolithography, the key component is the photomask, a patterned device made of transparent and light-blocking areas. Photomasks can be designed for different patterning methods, such as contact, soft-contact, and proximity lithography, all aiming for a 1:1 pattern in the photoresist layer. However, these methods can be vulnerable to wear and contamination. Alternatively, projection lithography masks (reticles) create 1:4, 1:5, or 1:10 reduced images in the photoresist layer, making them more resilient and suitable for high-volume production facilities.

Standard projection masks have diffraction limitations, but we can overcome them. This is achieved by altering the thickness of transparent areas or increasing the light transmission of the initially opaque regions. Another option is pixelating the original opaque areas, particularly for grayscale lithography. The typical chromium film thickness on a mask is 800 Å, and photomasks with 30–40 μm resolution can be produced with high-quality printers. Photomasks are usually made from soda-lime glass, borosilicate glass, or fused quartz, with considerations like

thermal expansion and optical transmission influencing the choice. For UV lithography at wavelengths shorter than 350 nm and for high-resolution applications, quartz masks are essential due to their thermal and optical properties.

Projection lithography masks (reticles) are designed to create 1:4, 1:5, or 1:10 reduced images in the photoresist layer. Modifying a standard projection photomask by pixelating opaque regions can control light intensity without creating individual pixels in the photoresist.

In microelectromechanical systems (MEMS) fabrication, optical projection tools project photomask images onto photoresist layers. These systems typically employ UV light emitted by a mercury arc lamp, which emits light in the UV spectrum, including g, h, and i-lines crucial for optical projection tools. There are two primary types of optical projection tools: contact aligners, used with contact and proximity masks, and steppers, used with projection photomasks or reticles. Contact aligners provide a 1:1 image of the photomask on the photoresist, making them suitable for large area patterns but with limitations related to mask damage and contamination. Steppers use reduced-scale images and require precise alignment and environmental control, offering higher precision but at a larger scale.

Photoresist is a vital material in microfabrication due to its sensitivity to UV light, enabling precise structure definition. Photoresist contains organic polymers and photosensitive additives dissolved in a solvent. Two primary photoresist chemistries exist: positive and negative. Positive photoresists increase solubility upon UV exposure, while negative photoresists decrease solubility. These chemistries offer distinct properties for specific applications in MEMS fabrication, allowing for high contrast and sharply defined features with steep sidewalls. The choice between positive and negative resists depends on specific photolithographic requirements and desired MEMS device properties.

5.2.3 Etching Technology

Etching is a crucial step in MEMS microfabrication, involving the precise removal of material from a substrate surface through chemical reactions to create specific patterns. Typically, a mask layer is applied to protect certain areas of the substrate from the etching process. Etching techniques can be broadly classified into two main groups: wet etching and dry etching. Wet etching, historically the dominant method, employs liquid-based etchants. In this process, the substrate is immersed in a liquid etchant, and the exposed areas of the substrate react with the etchant to dissolve, forming the intended pattern. Wet etching is appreciated for its simplicity, high selectivity, cost-effectiveness, and high throughput. However, it has limitations such as low aspect ratio, undercutting, and isotropic etching, which can hinder precise microfabrication. In contrast, dry etching provides an alternative approach to etching and has gained prominence due to its ability to address the limitations of wet etching. Dry etching uses a plasma chamber and reactive gas to remove material from the substrate, offering a more precise and controlled etching process. It comes with several advantages, including anisotropic etching, high aspect ratio, and precise control over etch depth. However, it requires more sophisticated equipment and is costlier than wet etching [140].

Common dry etching techniques in MEMS device fabrication include fluorine-based plasma etching and Deep Reactive Ion Etching (DRIE). Fluorine-based plasma etching is used to remove the oxide layer from Silicon-On-Insulator (SOI) wafers, creating openings for subsequent etching steps. DRIE is then used to etch through the silicon layer to shape the desired microstructure. These techniques offer superior control, precision, and repeatability, making them suitable for MEMS fabrication [2], [3], [6]–[8].

The Bosch process (Figure 5.5), a variation of DRIE, is a significant microfabrication technique that allows the creation of high-aspect-ratio structures in silicon. This process alternates between etching and passivation steps to produce vertical sidewalls, which are crucial for high aspect ratio structures. It is adaptable to different applications, offering high-rate and low etch rate processes. One challenge associated with the Bosch process is the loading effect, which can cause non-

uniform etch depth. This effect arises from the depletion of etchant species and involves parameters such as mean lifetime, the generation rate of active species in plasma, etchable area, and plasma volume. The formula for the loading effect on etch rate, as proposed by Mogab, is as follows[144]:

$$Etch\ rate = \frac{\beta\tau G}{1 + \beta\tau \frac{A_w d}{V}} \quad (5.4)$$

Where:

β represents the proportionality factor describing the affinity of the material being etched (silicon) to active species (fluorine).

τ stands for the mean lifetime.

G indicates the generation rate of active species in plasma.

d is a constant containing parameters of chemical reactions and materials being etched.

A_w is the etchable area.

V signifies the plasma volume.

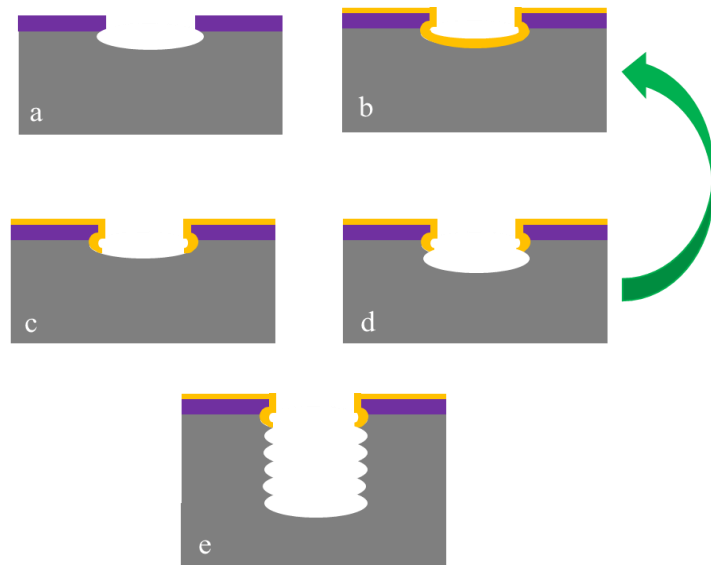


Figure 5.5 depicts the process of deep silicon etching using the Bosch technique, with distinct stages: a) isotropic etch step, b) passivation layer deposition, c) removal of the passivation layer, d) etching step, and e) the resulting trench after the iterative execution of steps b, c, and d [145].

5.3 Mask Designing

Successful and accurate production of complex microstructures in MEMS technology has a considerable impact on the critical mask design process. MEMS devices are intricate and precise, often composed of numerous components and structures, each serving specific functions and integration requirements. Specialized software tools are essential for designing layout masks to ensure the desired precision. Mask design plays a pivotal role in microfabrication, serving as the foundation for successful MEMS device fabrication. These complex structures, coupled with the need for precision, place significant demands on the design process. In the context of ongoing research, mask design must meet specific requirements, including:

Connection of device components: Mask design ensures that essential MEMS components are interconnected through conductive lines to separate pads. These components include actuator inclined beams, fixed fingers of the capacitive sensor, fixed fingers of the electrostatic actuator, and the shuttle of the electro-capacitive element. These pads establish connections between MEMS features and external instrumentation, facilitating the device's functionality and interaction with the surrounding environment.

Fabrication tolerances: Achieving fine fabrication tolerances necessitates early definition of all pads and conductive lines, particularly during the initial metal deposition stages of the SOI process. This is critical for attaining the desired precision and reproducibility in the final MEMS product. Precise conductive paths and interconnections are vital for ensuring the reliability and performance of MEMS devices.

In this research context, L-edit software, a specialized tool within the Tanner Tool suite, was used to define various features tailored to specific requirements, facilitating the creation of intricate MEMS structures:

Trench: This feature delineates the region of the silicon substrate that requires removal, a crucial step in defining the overall structure of the MEMS device.

Substrate: Although not applicable in the current design, this level allows researchers to define the substrate boundary, which is significant in specific MEMS applications.

Underpass: This step integrates underpasses, crucial for achieving electrical isolation while preserving mechanical connections between structures.

Electrical Pads: This level defines metal features with high tolerance, ensuring precise connections and structural integrity.

Chip Frame: This feature enables the creation of the chip's outer frame, often used in HF vapor etching processes to maintain the device's structural integrity during fabrication.

Oxide: While not utilized in the present design, this level permits the definition of features on the oxide layer, which may be crucial in other MEMS applications requiring insulation or specific material properties. Efficient and precise mask design is paramount for producing MEMS devices that meet stringent requirements for high precision, reproducibility, and reliability. The effectiveness of the microfabrication process relies on the efficient and precise design of these masks, especially in applications where MEMS devices play a critical role in sensing, actuation, and microfluidics. Therefore, the intricate process of mask design, supported by advanced software tools like L-edit, plays a pivotal role in the microfabrication of MEMS devices, ensuring their efficacy across various technological and scientific domains.

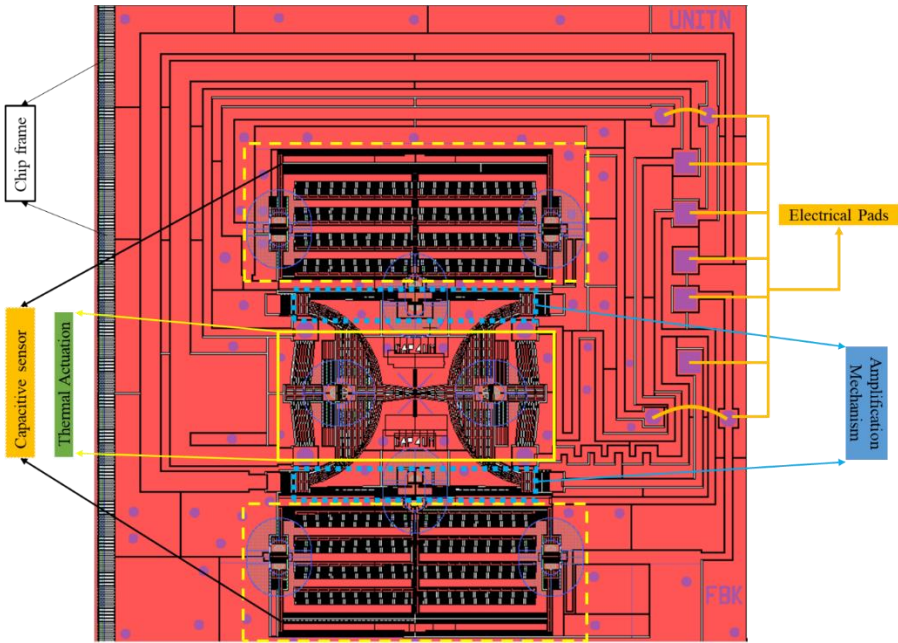


Figure 5.6: Mask design of MEMS based testing platform for investigating strain engineering characterization.

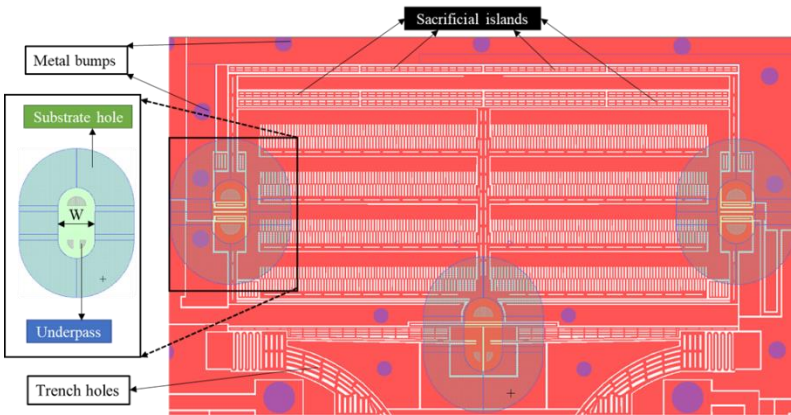


Figure 5.7: Mask design of underpasses on the capacitive sensor.

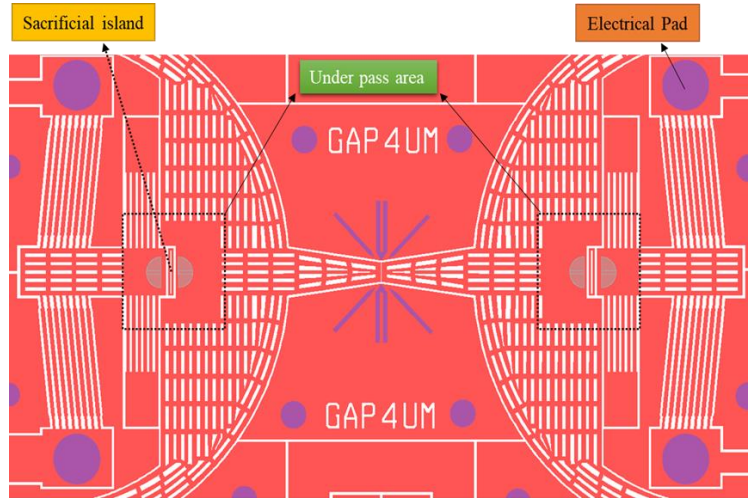


Figure 5.8: Mask design of thermal actuators which highlights the underpass areas.

Table 5.1: Underpass dimensions.

Underpasses on thermal actuator-length	210 μm
Underpasses on thermal actuator - width	160 μm
Underpasses on capacitive sensors-length	266 μm
Underpasses on capacitive sensors -width	160 μm

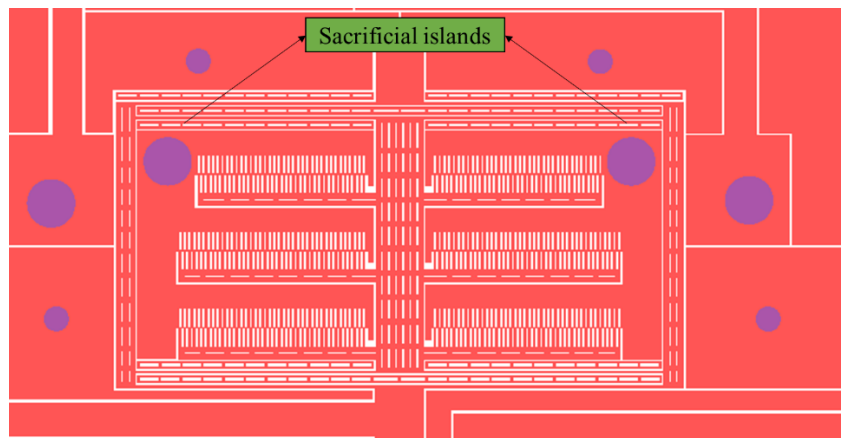


Figure 5.9: Mask design of MEMS electrostatic actuator.

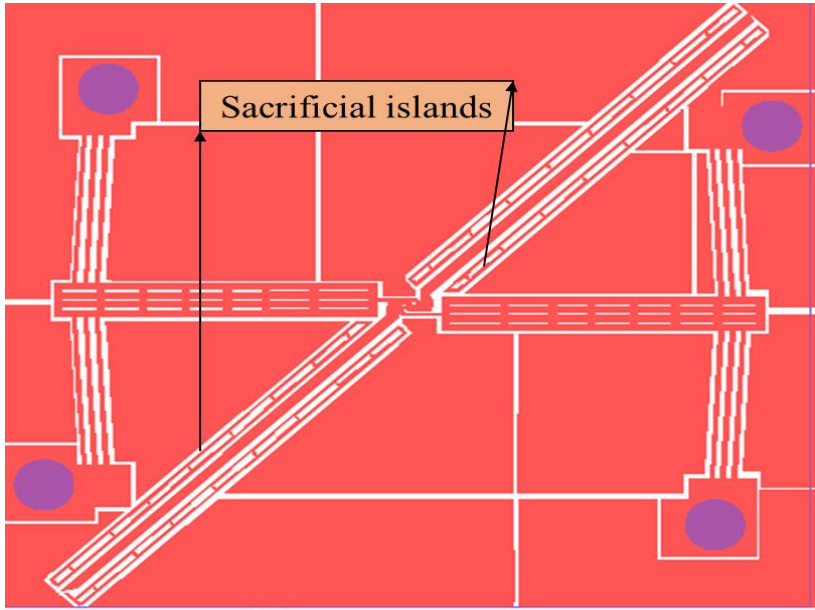


Figure 5.10: Mask design of MEMS based rotational structure.

For ease of handling and design, the wafer is typically divided into multiple units or chips. In current research, all the designed devices are placed on two separate chips. The first chip, measuring $5 \times 5 \text{ mm}^2$, serves as a MEMS-based testing platform for investigating strain engineering characterization (Figure 5.6). The second chip includes other devices (Figures 5.9-5.11), such as an electrostatic actuator ($1.7 \times 1 \text{ mm}^2$), a MEMS-based tensile testing device ($1.8 \times 1.4 \text{ mm}^2$), and a MEMS-based rotational structures (each of $1.3 \times 1.4 \text{ mm}^2$).

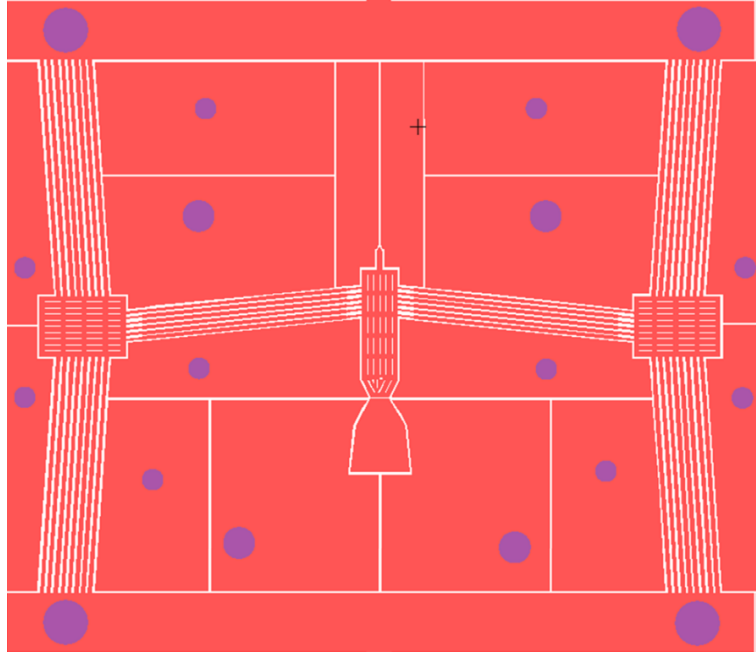


Figure 5.11: Mask design of MEMS based tensile testing device.

5.4 Fabrication Sequence

The journey of MEMS fabrication begins with the critical decision of material selection, a choice that profoundly impacts the performance and functionality of the resulting devices. Thorough materials research and analysis ensure that the chosen substrates are well-matched to their intended applications. The subsequent labeling of materials serves practical purposes and plays an integral role in quality control throughout the fabrication process. For instance, the selection of materials such as silicon, silicon dioxide, and aluminum for MEMS devices is guided by their mechanical, thermal, and electrical properties, as well as their compatibility with the fabrication processes. As part of this process, 6-inch SOI wafers with a substrate thickness of $525\ \mu\text{m}$, a buried oxide layer thickness of $2\ \mu\text{m}$, and a structural layer thickness of $25\ \mu\text{m}$ have been considered for the fabrication of MEMS devices.

The process then proceeds with rigorous cleaning and surface preparation, which are critical for the success of MEMS fabrication.

The integrity of MEMS devices hinges upon the cleanliness of the substrates. Even minute contaminants or particles can have detrimental effects on device performance. Cleaning is carried out through a meticulously orchestrated sequence of ultrasonic baths and chemical treatments, following established cleanroom procedures [1]. The cleanliness standards are such that even a small number of particles larger than 0.5 micrometers per square centimeter can significantly affect device yield and functionality.

5.4.1 Metal Deposition and Patterning

Within the realm of MEMS fabrication, magnetron sputtering is employed to achieve sputter deposition, ensuring the uniform application of a 1200 nm thick aluminum (Al) layer to the substrate's front side (Figure 5.11 a-c). The choice of aluminum is not arbitrary; it is fundamental to the functionality of MEMS devices, serving as a critical component for electrical interconnections. The deposition process occurs within a controlled vacuum environment, allowing for meticulous control over the resultant layer thickness. This choice is motivated by aluminum's exceptional electrical conductivity, ease of deposition, and compatibility with downstream processing steps. Following the aluminum deposition, a pivotal phase involves conducting a preliminary rinse, in adherence to established semiconductor fabrication methodologies. The primary objective of this rinse is to safeguard the cleanliness and integrity of the substrate, ensuring the removal of any residual contaminants that might have inadvertently infiltrated during the deposition process [138]. Following this critical step, the front side of the substrate undergoes coating with a protective layer, typically involving the use of AZ4562 photoresist. This practice is grounded in well-documented semiconductor manufacturing procedures and serves as a preparatory measure for subsequent lithographic patterning. A mask aligner is employed for patterning the aluminum metal, maintaining precision and control over the process. Once the exposure is complete, chemical development of the photoresist ensues, resulting in a patterned mask that serves to protect the underlying metal. Quality control measures, such as optical inspection, are integral to this phase, facilitating the verification of the pattern's accuracy and integrity. This inspection process involves high-resolution imaging, where any deviations from the desired pattern

undergo thorough analysis. In order to secure the stability of the photoresist, a hardbake step is executed, a practice aligned with well-established semiconductor manufacturing protocols.

5.4.2 Metal Etching

Following the aluminum deposition, a pivotal stage in the fabrication process necessitates the precise removal of a 150 nm thick aluminum layer through the use of dry etching. The execution of metal dry etching was accomplished utilizing the Tegal 6510 IC processing tool, a facility where careful control over etching rates, selectivity, and etch chemistry is maintained to attain the desired aluminum patterning. The specific parameters employed included a pressure of 3 mTorr, a chlorine (Cl) flow rate of 23 sccm, a hydrogen bromide (HBr) flow rate of 20 sccm, and a power setting of 500W.

In this particular case, dry etching is the preferred method due to its ability to eliminate under etching of the metal, which is a common concern associated with wet etching techniques. Under etching refers to the lateral removal of material during the etching process, which can result in imprecise patterning and, in the case of aluminum, may lead to undesirable shorts or electrical connections between adjacent components. Dry etching offers a more controlled and anisotropic etching process, ensuring that the aluminum patterning is precisely aligned with the intended design, without the lateral side effects typically observed in wet etching. This choice underscores the significance of dry etching in achieving the high precision and quality demanded in MEMS fabrication. Optionally, a Defreckeling step may be employed to eliminate any remaining residues or particles, following established microfabrication techniques [146]. Subsequently, resist ashing is removes the remaining photoresist. The inclusion of these optional steps hinges on the cleanliness requirements of the MEMS device and the observed substrate cleanliness.

5.4.3 Masking Layer Deposition

In silicon Deep Reactive Ion Etching (DRIE), masking layers play a crucial role, significantly influencing the success and quality of the

etching process. The choice of a masking material, often comprising substances like photoresist, is a pivotal decision. This material has the essential function of defining the areas to be etched while safeguarding the surrounding silicon substrate. The selection process is meticulous, involving stringent criteria. The selected masking material must exhibit high selectivity, effectively resisting etching while enabling the removal of the underlying silicon. Compatibility with etch chemistry, chemical resistance, mechanical properties, and precise pattern resolution are paramount considerations. Additionally, the masking material should be cost-effective, readily available, and compatible with the entire DRIE process, encompassing cleaning to post-etching steps. Careful selection is imperative to ensure the precision, quality, and integrity of the etched microstructures [140], [145], [147].

In deep silicon etching, aluminum frequently emerges as the preferred masking layer for DRIE due to its high selectivity to silicon, ease of patterning via lithography, excellent thermal conductivity for efficient heat dissipation, chemical compatibility with DRIE etchants, cost-effectiveness, and widespread availability. Aspect ratio, a pivotal parameter in deep etching, delineates the ratio between feature width and depth. The etching time limit plays a central role in achieving the maximum aspect ratio. Commonly used masking materials like photoresist and silicon oxide typically enable aspect ratios of less than 35 [147]. However, there is a desire for higher aspect ratios to enhance the performance of various MEMS devices. In this context, aluminum presents itself as a promising thin masking material, boasting extreme selectivity in DRIE plasma and compatibility with standard microfabrication processes. Its low etch rate allows for significantly extended etching times, which can be advantageous for the fabrication of high aspect ratio structures with sub-micron critical dimensions. Nevertheless, a challenge associated with aluminum masking in DRIE is the formation of micro masking, leading to a grass-like morphology and interruption of the etching process. This challenge requires further investigation and resolution. These attributes render aluminum a versatile and dependable choice for crafting intricate microstructures in silicon through the DRIE process. It's worth noting that DRIE etching with a bare aluminum mask can generate micro masking issues, which can be mitigated by applying a sufficient oxide layer atop the thin aluminum layer [147], [148].

The masking layers are sequentially deposited on both the front and back sides, following this order: a 600 nm thick PECVD silicon oxide layer, a 150 nm thick magnetron-sputtered aluminum layer, and a 200 nm thick PECVD silicon oxide layer serving as a protective barrier. The thickness of the SiO layer is pivotal in ensuring uniformity and electrical insulation from the underlying aluminum-patterned pads. Precise control over the SiO layer's thickness is critical for achieving electrical isolation, managing stress, and optimizing the dielectric properties of the MEMS device.

After the deposition of the masking layers, the next step involves exposing the front structural layer using a lithography stepper tool with the assistance of a reticle mask (as shown in Figure 5.16). It's important to note that during lithography exposure, one of the critical factors to consider is mask alignment to ensure precision and accuracy in the fabrication process. Proper mask alignment is essential for achieving the desired results in fabricating these intricate structures. The exposure of structural results shown in Figure

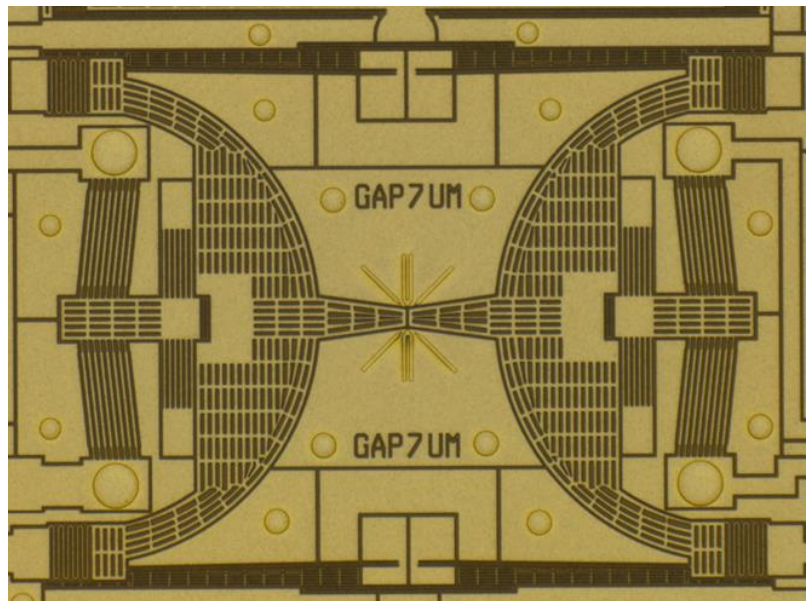


Figure 5.12: Illustrates the exposure results of the structural layer for silicon etching in a MEMS-based testing platform designed to accommodate a 7 μm sample length.

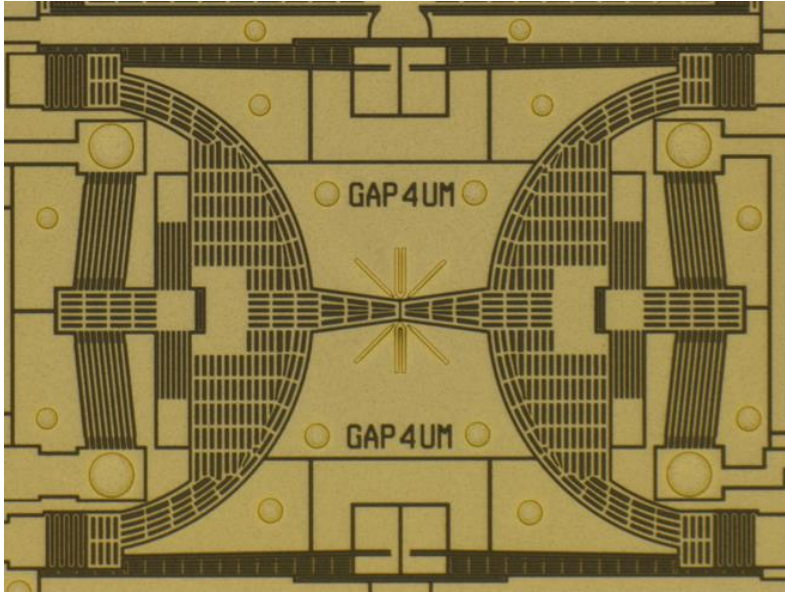


Figure 5.13: Exposure results of the structural layer in a MEMS-based testing platform designed for silicon etching with a sample length of 4 μm .

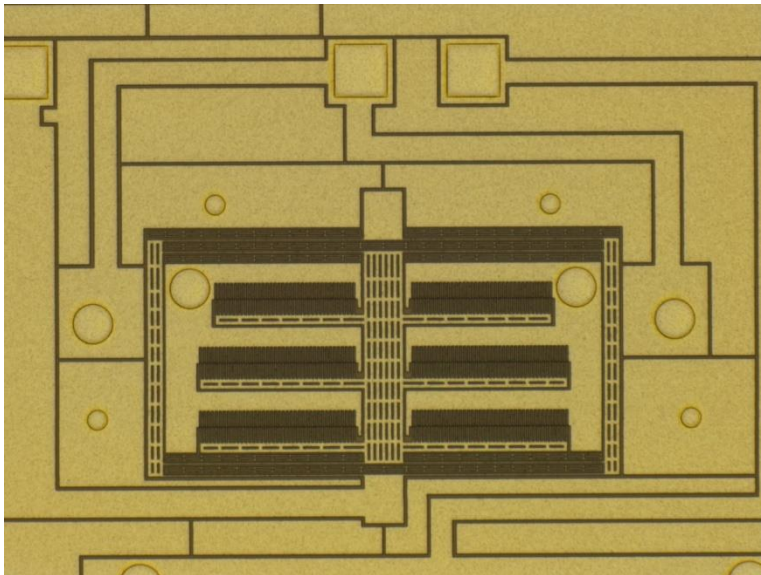


Figure 5.14: Exposure results of the structural layer in a MEMS electrostatic actuator.

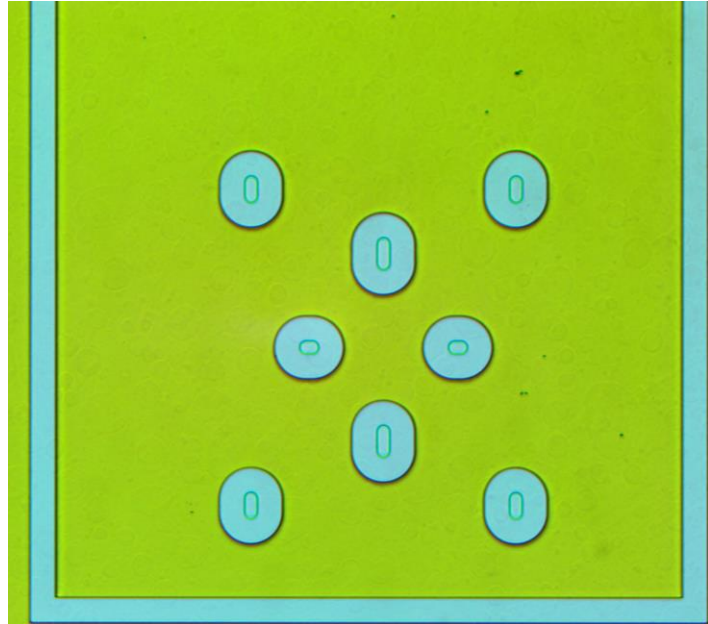


Figure 5.15: Depicts the backside wafer exposure used in the creation of underpass structures.

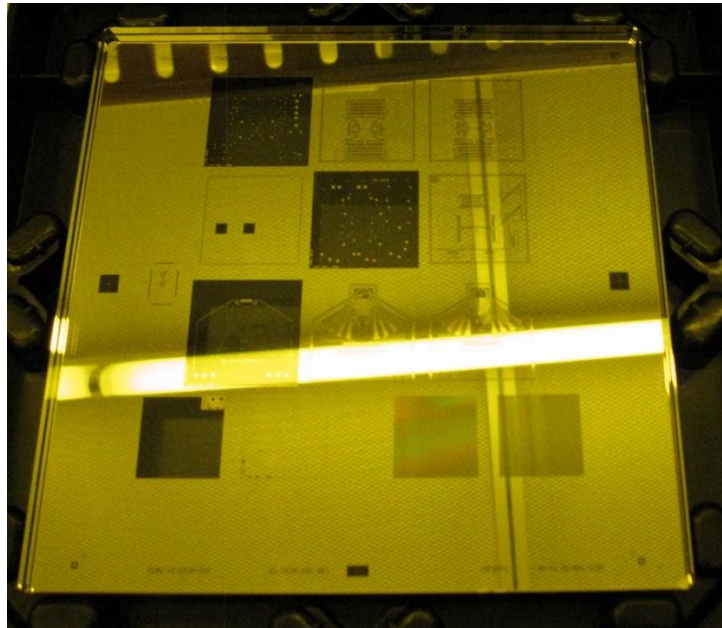


Figure 5.16: The Reticle masking layer for patterning structural layer.

5.4.4 Silicon Etching

The fabrication process involves intricate silicon etching steps that are crucial in shaping the MEMS device. To reveal the underlying silicon structures, layers are meticulously patterned using stepper photolithography tool. Subsequently, a plasma etching process is employed to etch these layers. The exposed silicon device layer is further etched down to the buried oxide layer, a critical stage that defines the device's main features. This is achieved through the utilization of the Alcatel AMS200 Deep Reactive Ion Etching (DRIE) process, recognized for its ability to provide anisotropic etching with higher selectivity and verticality (Figure 5.18f). Notably, in this research, three masking layers are employed, including the reticle, serving as the dark data mask for patterning the main device layer, and two light data masks, which are employed for back patterning to create underpass islands. The DRIE process stands as the ideal choice for achieving the complex geometric shape required for this MEMS devices. It boasts etching capabilities that result in a high ratio of etching gap to depth, a prerequisite for this application. Specifically, the device necessitates a minimum etching depth of 25 μm for the device layer and 525 μm for the handle layer. This is primarily due to the intricate nature of the device's structure, which comprises elements of varying dimensions. Among these, certain elements pose a constraint to functionality. From the perspective of capacitive electrostatic actuation, it is imperative that the comb-drive fingers and gaps between the stator and rotor finger arrays possess dimensions within the range of a few micrometers.

The etching process begins with the exposed silicon being etched from the front side using deep reactive ion etching (DRIE). Both front and back etchings proceed until they reach the buried silicon oxide layer, which is embedded in the SOI wafers and serves as an etch stop (Figure 5.18g). This multifaceted etching procedure plays a pivotal role in achieving the desired geometric shape and functionality of the MEMS device.



Figure 5.17: Stepper Lithography.

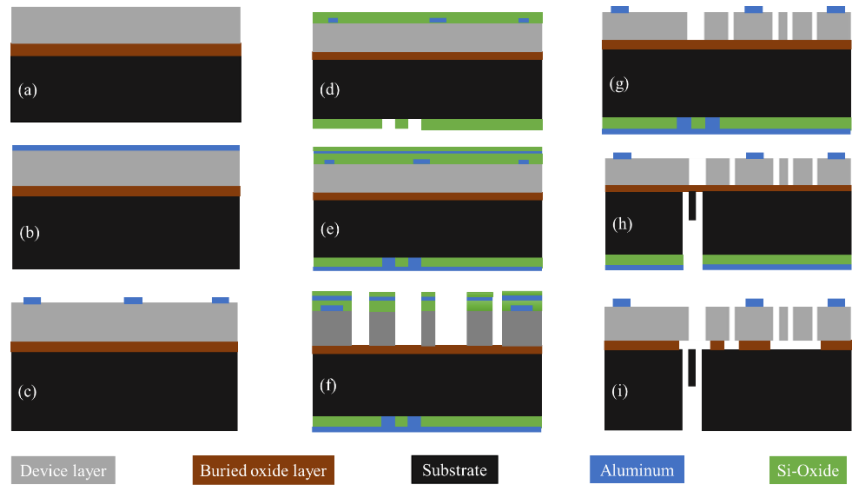


Figure 5.18. The main fabrication sequence steps.

Following the completion of the silicon etching steps, the subsequent phase involves the removal of the masking layer. To achieve this, the Tegal 900 IC processing tool is utilized for the silicon dioxide layer, while the Tegal 6510 IC processing tool is applied for metal etching (Figure 5.18g-h). These tools are instrumental in ensuring the precise removal of masking layers, leaving the desired structures intact.

Quality control is essential throughout the fabrication process to ensure precision, integrity, and overall quality of the structures. A crucial part of this quality assurance is Scanning Electron Microscope (SEM) inspection (Figure 5.19). SEM allows detailed examination, ensuring the structures meet MEMS quality standards. It verifies critical dimensions, assesses etch profiles, and detects defects that could affect device performance.

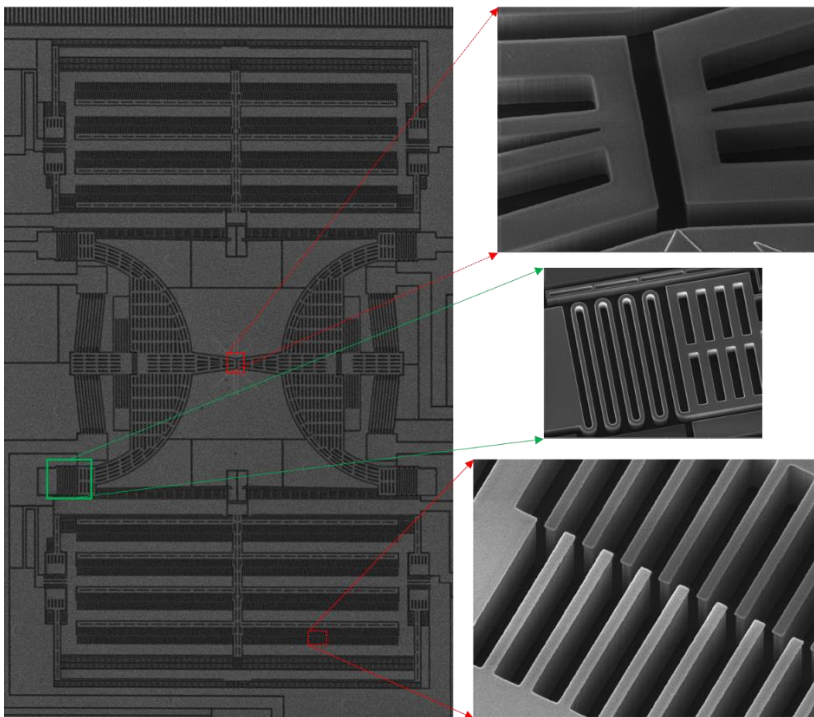


Figure 5.19: SEM inspection after deep silicon etching.

5.4.5 Final Processing with HF Vapor Etching

As the final step of the fabrication process, HF vapor steps play an important role in releasing the MEMS devices. The removal of the buried silicon oxide is achieved with the help of an HF vapor etching tool, by the SPTS Primaxx® uEtch, a product of SPTS Technologies Ltd. This step is of paramount significance in the current research as it serves the dual purpose of eliminating the sacrificial islands (Figures 5.20-5.22) and ensuring the devices are liberated from the substrate, a critical milestone in the MEMS microfabrication process.

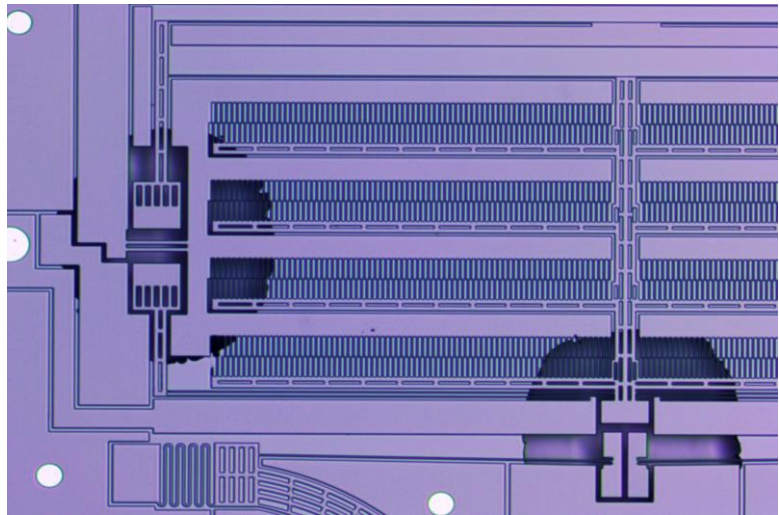


Figure 5.20: Sacrificial islands removed in a capacitive sensor within a MEMS-based testing platform.

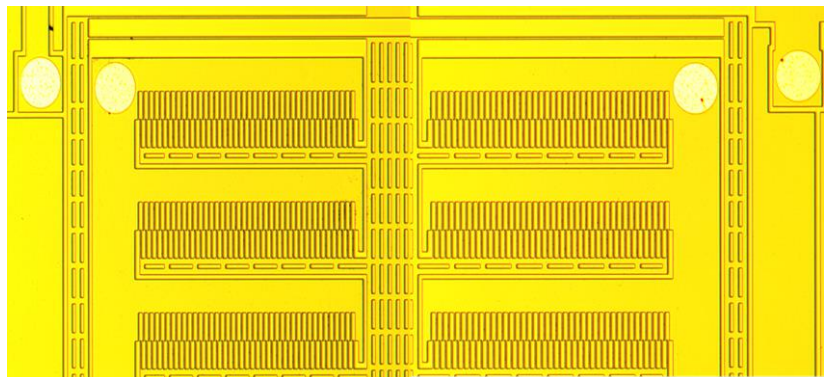


Figure 5.21: Sacrificial islands removed in electrostatic actuator.

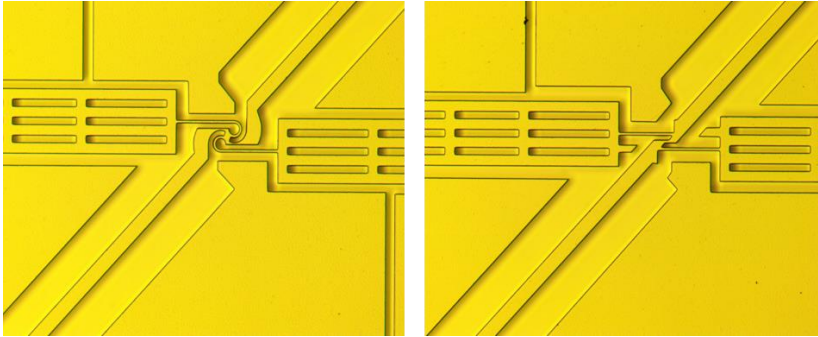


Figure 5.22: Sacrificial islands removed within MEMS-based rotational structures.

5.5 Wire Bonding Within the MEMS Device

Wire bonding plays a critical role in connecting microelectronic devices to printed circuit boards (PCBs) and establishing internal device connections. In the realm of wire bonding, two primary techniques, wedge bonding and ball bonding, have been the focus of the current research. The choice of the bonding method depends on the specific requirements of the application and the characteristics of the devices and PCBs involved [149]

In that context, wedge bonding is a wire bonding technology initially considered in this study for creating electrical connections within the electrostatic actuator (Figure 5.23). Wedge bonding was chosen as the method of choice due to its capability to bridge the electrical pads on the actuator, which separated by a side shuttle, effectively grounding the electrostatic actuator. Consequently, wire bonding was deemed necessary to establish a robust connection between the device and the PCB. Wedge bonding involves using a wedge-shaped tool to deform and attach a wire (aluminum used) to the contact points on the PCB and the device. This deformation creates a physical and electrical connection, ensuring the transmission of signals and power. The choice of wire material is determined by factors such as conductivity, corrosion resistance, and thermal properties, making it crucial to select the appropriate material for the specific application.

The wedge bonding method exhibits specific challenges and limitations, which become notably pronounced in the context of the electrostatic actuator designed in current research. These challenges arise from the limited gap (120 μm) between the electrical pads that necessitate electrical bridging (Figure 5.23). This constrained space restricts the formation of sufficient wire loops, which are crucial for preventing inadvertent wire contact with shuttles or internal obstructions within the device (shown in Figure 5.24). The absence of these loops poses a risk of unintentional wire contact, potentially resulting in electrical short circuits.

Moreover, the limited distance between the pads can impede the bonding process, especially in devices with closely spaced contact points. Notably, wedge bonding poses a risk of damage, particularly in devices with delicate or thin components. The application of mechanical force during bonding may result in handling-induced breakage or deformation of these fragile features (Figure 5.25). Material compatibility, process sensitivity, and potential interference with other components also add to the challenges and limitations of this method. Therefore, careful consideration of these factors is crucial when choosing wire bonding techniques, especially in cases where the constraints of the wedge bonding method may not align with the specific requirements of the microelectronic devices.

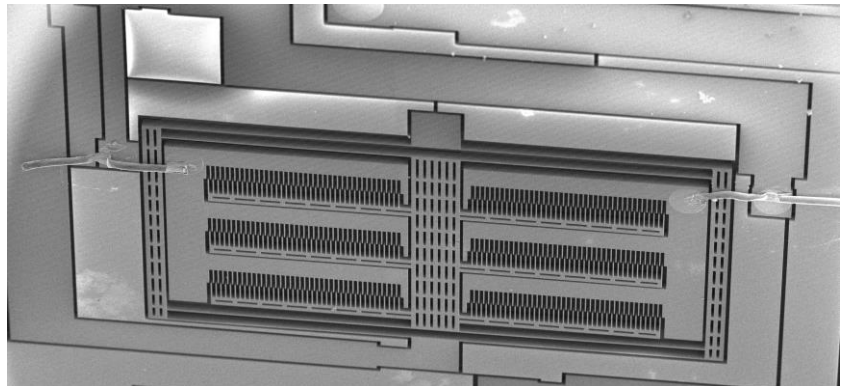


Figure 5.23: SEM image of wedge bonding in MEMS electrostatic actuator.

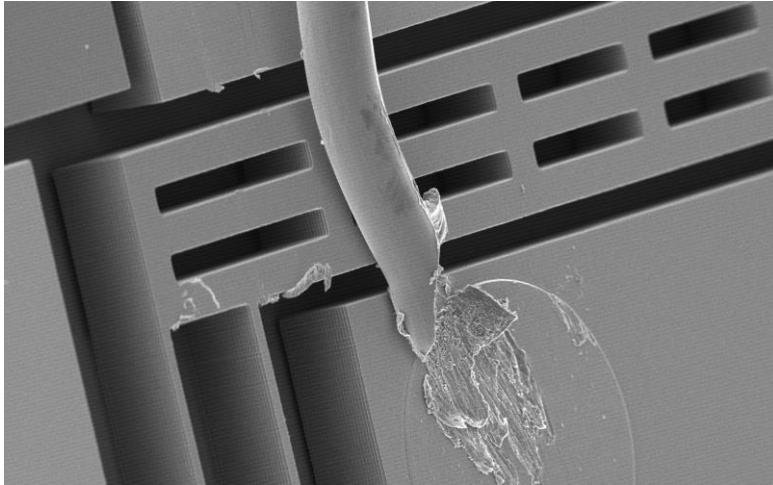


Figure 5.24: SEM image of wire interaction with movable shuttle in the electrostatic actuator.

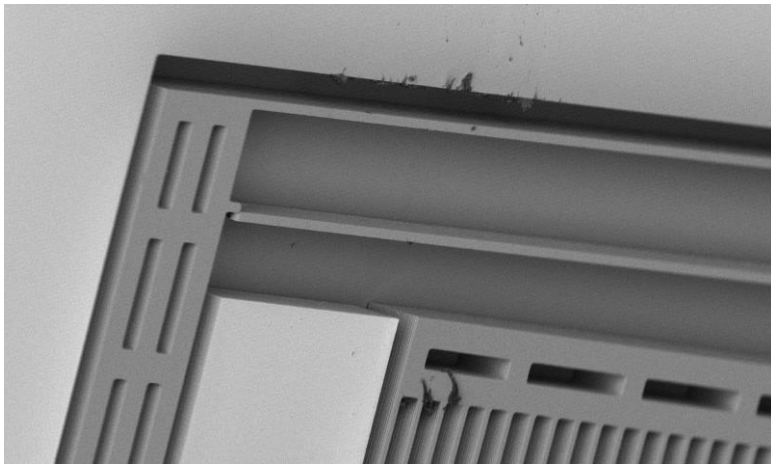


Figure 5.25: Structural fracture resulting from the wedge bonding process.

Following the initial trials with wedge bonding, it became apparent that further electrical connections were required within the MEMS device itself. Ball bonding, a distinct wire bonding technique, was subsequently employed to meet this need. Through multiple trials, succeeded in establishing reliable wire bonds within the device, thereby achieving the desired electrical connections.

Ball bonding is characterized by the formation of small, spherical balls at the ends of the wire, which are then thermosonically bonded to the

contact points on the device and the PCB. The process involves a combination of mechanical pressure and localized heating, ensuring a secure and low-resistance connection. The choice of parameters, such as bonding temperature, force, and duration, plays a crucial role in the quality and reliability of the bond. Gold was chosen as the material of preference for this process due to its exceptional electrical conductivity, which ensures minimal signal loss and efficient power transmission. Furthermore, gold's corrosion resistance and long-term stability make it an excellent choice to maintain the integrity and reliability of wire bonds in microelectronic devices. Following the careful optimization of bonding parameters, successful wire bonding, as depicted in Figure 5.26, was achieved.

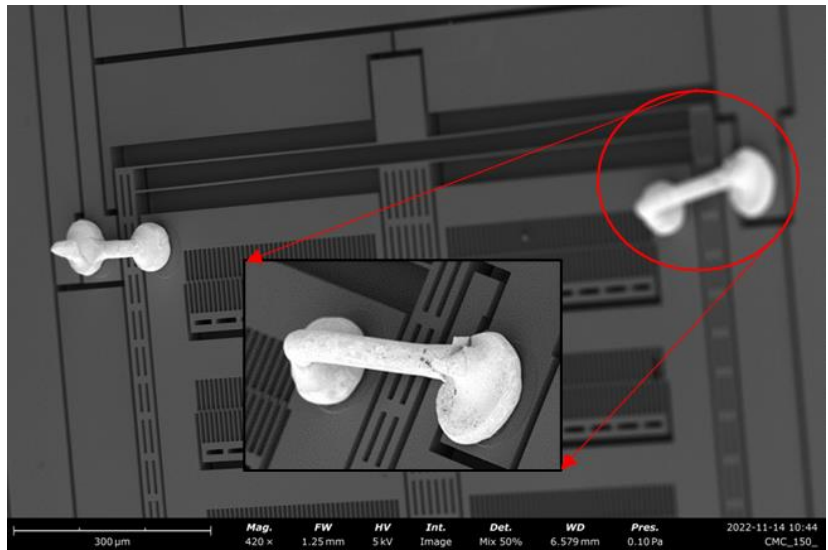


Figure 5.26: SEM image of electrical bridging using ball bonding technology.

Table 5.2: Ball bonding optimized parameters.

Positions	Spark size (μm)	Force (μN)	Power ($\mu\text{N}/\mu\text{m}^2$)	Time (sec)
1 st ball	1.2	2	2	3
2 nd ball	1.2	2	2	4

The challenges encountered during ball bonding are primarily linked to the size of the electrical pads. The larger size of the wire bonding ball

compared to the electrical pad presents difficulties in achieving precise bonding. In the current research, the selected ball size represents the minimum size that can be effectively utilized. Reducing the ball size below 1.2 μm radius, leads to significant adhesion issues and complicates the bonding process.

Another critical factor is the size of the electrical pads, which need to be sufficiently large to accommodate a buried oxide layer connecting to the substrate. This is essential to prevent the formation of a floating structure during bonding, which could potentially damage the pads in the process.

This chapter 6 concentrates on presenting the microfabrication results and characterizing MEMS devices at room temperature as part of the ongoing research. Additionally, preliminary findings at cryogenic temperatures in ultra-high vacuum STM chamber are discussed.

6.1 Fabrication Results

The primary aim of this research was to optimize the fabrication process for creating MEMS devices with underpass structures on silicon-on-insulator (SOI) wafers. These underpass structures serve the dual purpose of providing electrical isolation while maintaining mechanical connections between different components of the device. Achieving this delicate balance necessitated a systematic exploration of etching parameters and processes. In that context, we considered two batches of the fabrication process, with a total number of 9 wafers. The fabricated results are shown in Figures 6.1-6.2 for MEMS rotational structures, and Figures 6.3–6.8 depict the results for the underpass.

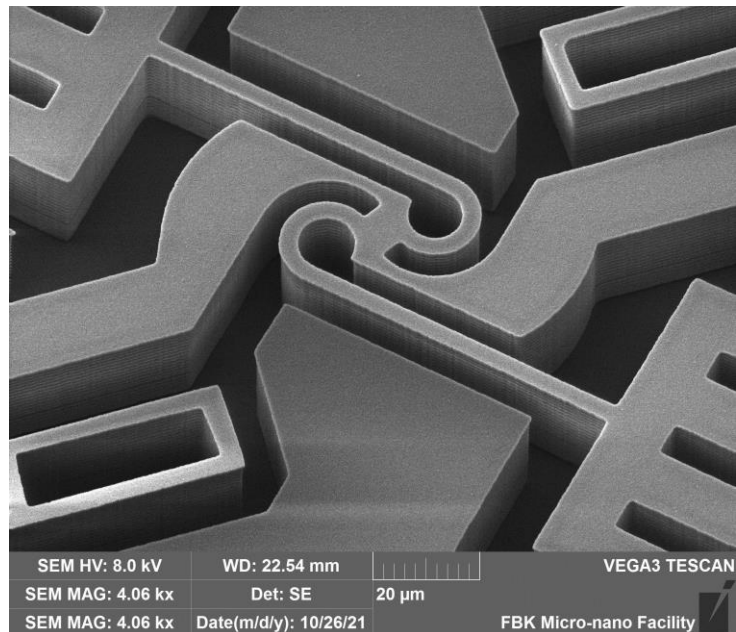


Figure 6.1: SEM image of the novel c-shaped structure in MEMS rotational device.

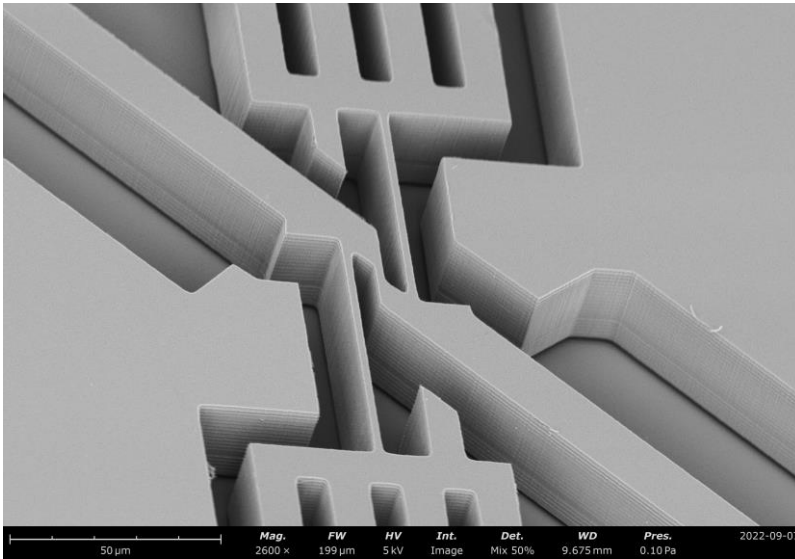


Figure 6.2: SEM Image of the Rotational Mechanism in the Symmetrical Lancet Structure.

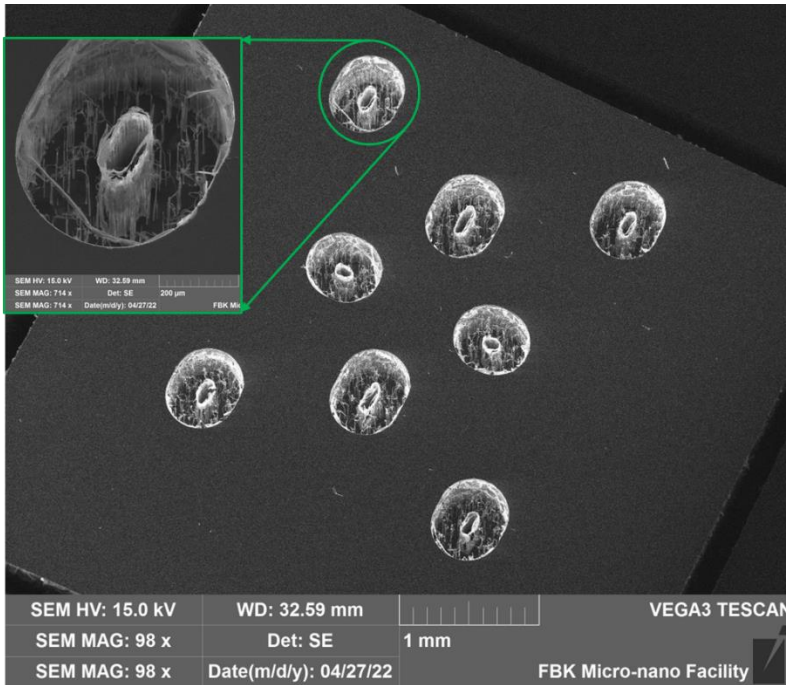


Figure 6.3: Underpass results for wafer-2 in batch 1 fabrication.

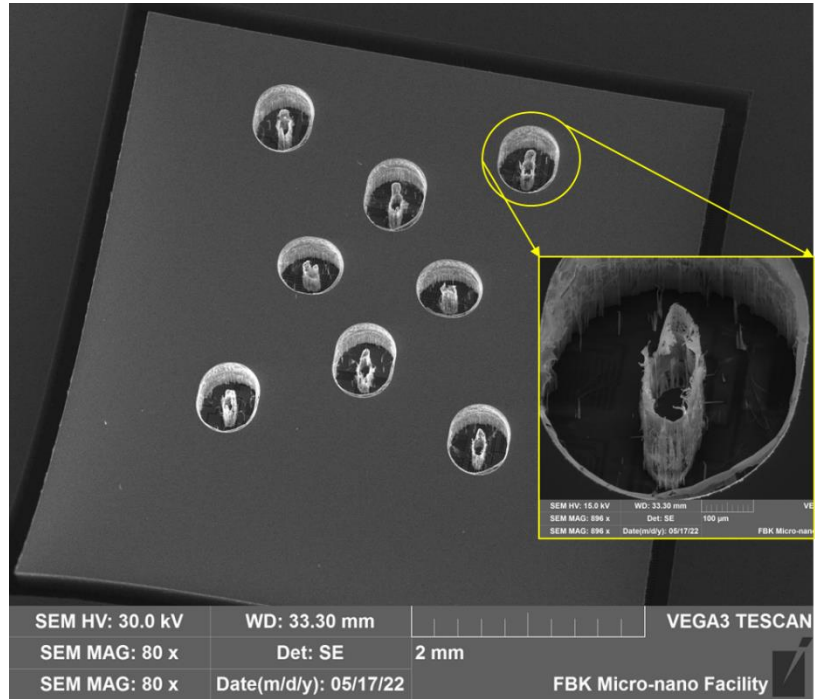


Figure 6.4: Underpass results for wafer-4 in batch 1 fabrication.

In the initial phase of experimentation, our focus was on the underpass island etching process, particularly achieving the desired geometry. The first experiments conducted on wafers 1-2 involved a sequence of steps, which included Surface Dielectric Etch (SDE) using 70 sccm of O_2 at $0^\circ C$ for 5 minutes, followed by an oxide etch of 103 seconds, a flash Deep Reactive Ion Etching (DRIE) step, and an extended SDE step of 70 sccm O_2 for 58 minutes. While this approach showed promise, it became evident that a longer initial SDE duration of approximately 15 minutes was needed to achieve the desired underpass geometry. Wafer 2 results shown in Figure 6.3.

Subsequent experiments, such as those conducted on wafer 3, involved adjustments to etching parameters. The introduction of a 15-minute initial SDE step, followed by additional processing, led to an improvement in underpass geometry. However, it was noted that remnants still existed. To further enhance the results, an additional 8-minute SDE step was incorporated.

Wafer 4 marked a significant breakthrough in the optimization process. It introduced a simplified, single-step approach. This involved an extended SDE step using 65 sccm of O₂ at 0 °C for 70 minutes. The extended duration aimed to both create underpasses and remove the oxide layer during the SDE step. This innovative approach successfully yielded high-quality underpasses with dimensions suitable for subsequent DRIE etching.

The results from wafer 4 (Figure 6.4) served as the optimized recipe for the underpass island fabrication process. The specific conditions for the SDE step, such as gas flow rates, temperature, and etching time, were adjusted in the experiments to achieve the desired underpass geometry and overall device performance. This optimized approach marked a significant advancement in the fabrication process and laid the groundwork for further MEMS device production, emphasizing electrical isolation in SOI MEMS devices.

However, as the final step in the fabrication sequence, HF vapor etching was employed to remove the buried oxide layer, allowing the separation of movable structures from the substrate and the removal of sacrificial islands. Unfortunately, despite the achievement of an optimized underpass geometry on wafer 4, it was found that the underpass geometry might not be sufficient to withstand the 24-minute HF vapor etching required for buried oxide removal, as optimized for devices fabricated in this research. The duration of HF vapor etching primarily depended on the dimensions of the square trenches used in the device design. It became evident that an increase in the size of the underpass structures within the device design was necessary to facilitate successful HF vapor etching.

In response to the challenges encountered during batch-1 fabrication, several design adjustments were made. Most notably, the underpass geometry was increased in the design to ensure it could withstand the required duration of HF vapor etching for buried oxide removal. This modification was critical to achieve the desired separation between the movable structures and the substrate.

Further adjustments were made to the etch holes (trenches) within the design. These changes aimed to improve the overall etching process and enhance control over feature sizes, which was crucial in achieving the desired geometries during the fabrication process. Additionally, the design adaptations included modifications to wire bonding for electrical connections within the MEMS device. These changes streamlined electrical connections and reduced wiring complexity, thereby simplifying the device's overall design and enhancing its performance and reliability.

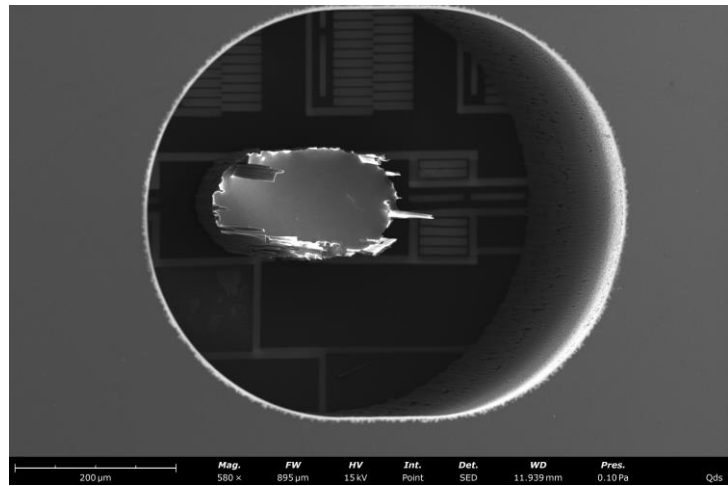


Figure 6.5: Fabricated underpass structure on wafer-1 in the capacitive sensor.

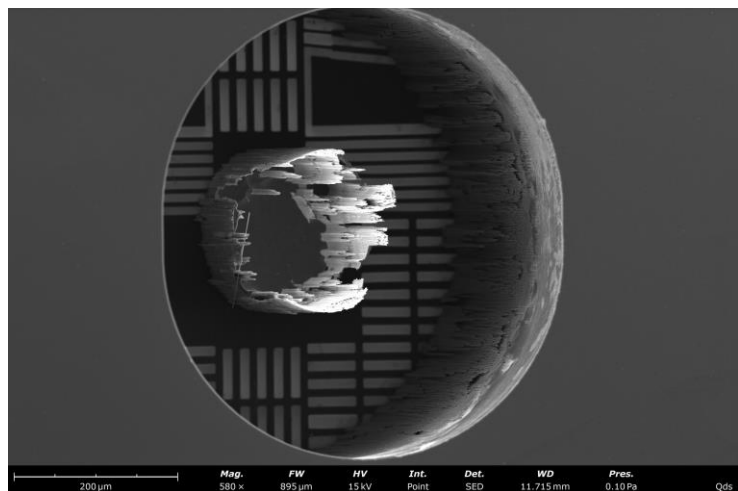


Figure 6.6: Underpass structure on wafer-1 in the thermal actuator.

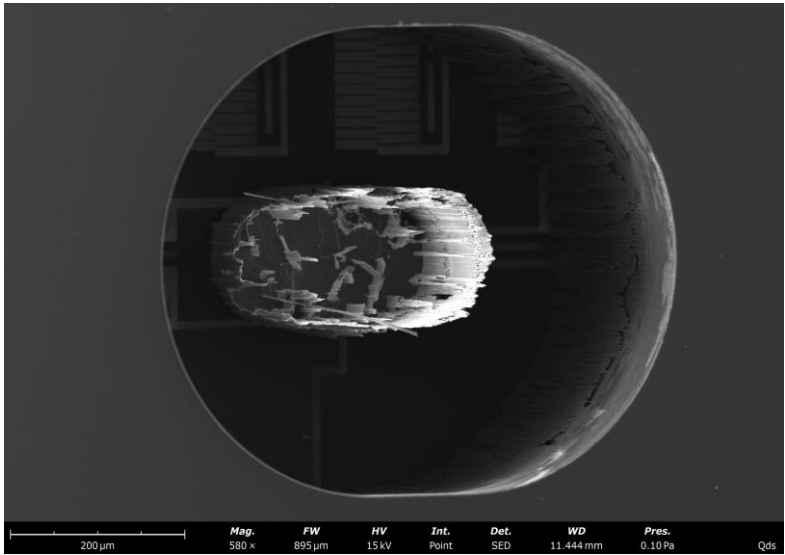


Figure 6.7: Underpass structure on wafer-2 in the capacitive sensor.

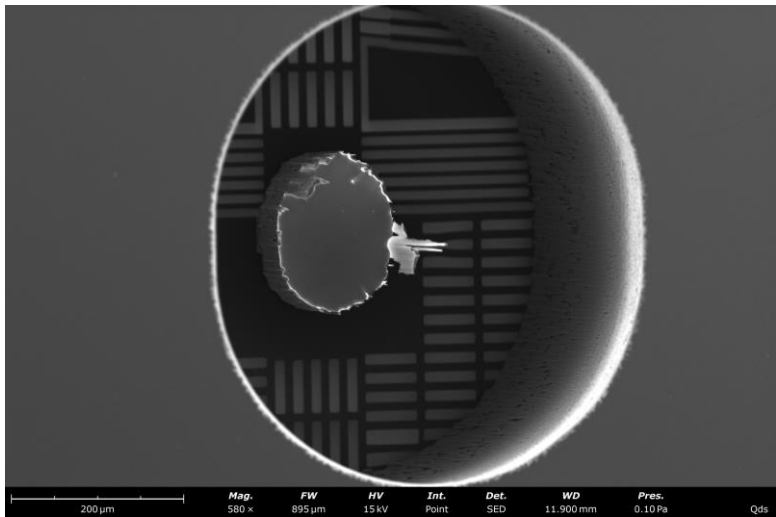


Figure 6.8: Wafer-2 one of the underpass structures on the thermal actuators.

In batch 2, the fabrication process continued with a total of 5 wafers, building upon the insights and limitations identified in batch 1. The entire fabrication process sequence was repeated, as depicted in Figure 5.18, with a continued focus on optimizing underpass structures and enhancing overall device performance. For underpass structures, the parameters optimized in batch 1 were retained. Wafer 1 in batch 2

employed a single-step approach with a 65-minute duration, achieving an average underpass thickness of approximately 20 μm (Figures 6.5-6.6). However, a discrepancy of around 16% was observed in the area of the underpasses when comparing the designed dimensions with the fabricated results.

Building on the insights from wafer 1, wafer 2 (Figures 6.7-6.8) in batch 2 followed a similar etching process with parameters, but with a reduced etching time of 10 minutes. This adjustment aimed to investigate the relationship between etching time and underpass dimensions. On this wafer, the average underpass thickness was noted to be around 25 μm , while the area difference between the designed underpasses and those fabricated increased to approximately 27%. These results offer valuable insights into the effects of etching time on underpass structures. It becomes evident that prolonged etching times lead to higher consumption of underpass thickness while increasing the overall underpass area. This trade-off underscores the importance of carefully optimizing etching times in the fabrication process to achieve a balance between desired underpass dimensions and minimizing area discrepancies, a crucial aspect in the effective integration of these structures into MEMS devices.

The feedback on the underpass geometry is crucial, and it is provided by the data from batch 2. Additionally, it is important to carefully consider the sizes of the underpass. Keeping a sufficiently large area of the underpass structure is important to maintain a stable connection between the two parts as a mechanical design rule.

In the MEMS device fabrication process, feature size reduction can occur due to misalignment during lithography, significantly impacting device performance. In the devices fabricated in this research, feature sizes were unintentionally reduced by approximately 1.73 μm from the original designs. Surprisingly, this reduction had a positive impact on device performance due to increased flexibility of the beams. These findings underscore the importance of considering fabrication tolerances and the potential benefits that may arise from unintentional changes in device dimensions. These impacts were taken into consideration when comparing simulation and experimental results.

6.2 Electrical Characterization at Room Temperature

DC Measurements for all the MEMS devices in this study were electromechanically characterized using a Keysight B1500A semiconductor device analyzer, and a semiconductor measurement probe station at the Bruno Kessler Institute. Four Source/Measure Units were employed to deliver the signal input, with probe tips connected to the aluminum pads on the devices (Figure 6.9). The Start Easy EXPERT software controlled the I/V sweep during the experiments.

To measure the displacement of MEMS devices, DC voltages were sourced to observe the displacement optically in an air medium. The process involved capturing sequences of microphotographs while applying various input voltages to the MEMS devices. Initially, a smaller range of voltages, determined by simulation results for each MEMS device, was used, gradually increasing in fixed voltage increments until a dedicated final voltage was reached. A camera was integrated into the system to capture magnified images of the structures, which were then stored on a computer. To ensure system stability, a 7-second delay and a 2-second hold were introduced between each voltage increment and image capture. For each trial, reference images taken at 0 voltage were used. The displacement was determined by analyzing the acquired microphotographs using the GNU Image Manipulation Program (GIMP).

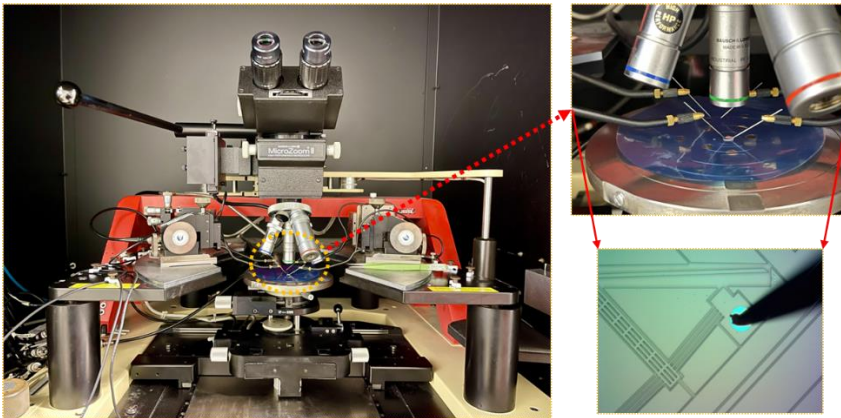


Figure 6.9: Room temperature electrical probe station setup (probe tip radius 20 μm).

6.2.1 MEMS Based Rotational Structures

DC voltage ranging from 1 to 2 volts, with incremental steps of 0.2 volts was applied for both symmetrical lancet and symmetrical C-shape MEMS-based rotational structures to compare their performance experimentally. The displacements were measured using the GIMP programme as mentioned above. The results showed that the displacement increased as the input voltage increased for both the symmetrical lancet and C-shape MEMS rotational structures.

Figure 6.10 shows the performance comparison of symmetric lancet and C-shape MEMS rotational structures using both simulation and experimental results. The symmetrical C-shape structure showed an improved performance of 22% compared to the symmetrical lancet model. The comparison of experimental and simulation curves for both MEMS rotational structures was conducted in this study. The experimental and simulation results showed a maximum error of 3.2%. However, at lower voltages, the curves started to diverge due to fabrication tolerances, which resulted in thinner structures and increased displacement. The error between the experimental and simulation results was larger (~12%) at smaller voltages and gradually decreased to a maximum error of 3.2% at higher voltages. This discrepancy could be attributed to environmental factors such as air resistance. The findings of the study emphasize the importance of considering fabrication tolerances and environmental factors when comparing simulation and experimental results. Such considerations are critical for obtaining accurate and reliable results in micro-electro-mechanical systems (MEMS) research and can inform the design and fabrication of more efficient and reliable MEMS structures.

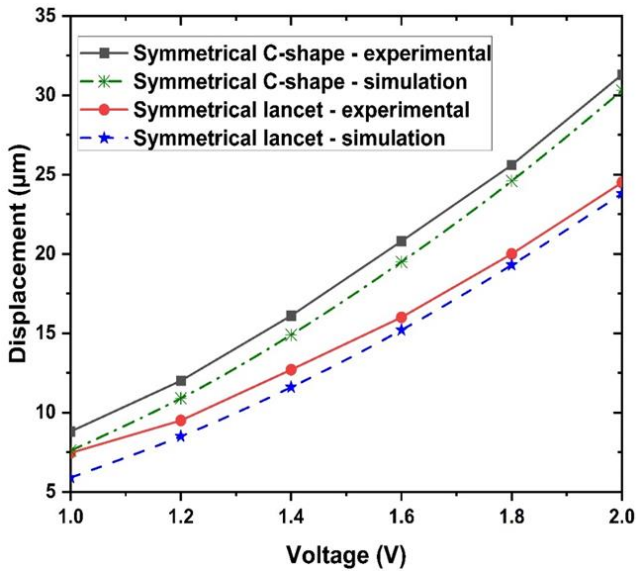


Figure 6.10: Comparative analysis of symmetrical lancet and C-shaped mems rotational structures: simulation and experimental results.

6.2.2 MEMS Electrostatic Actuator

In the fabricated electrostatic actuator (Figure 6.11). the actuation voltages were applied to the actuation comb drives, spanning from 0 V to 25 V in 5 V increments. At the maximum voltage of 25 V, the device exhibited a displacement of $\sim 9.5 \mu\text{m}$, as depicted in Figure 6.12. This limited range is attributed to a hard limit embedded in the design to prevent overextension. Beyond 25 volts, a critical phenomenon known as resistive welding becomes a concern in the current MEMS electrostatic actuator. Resistive welding occurs when high electrical current flows through the static and movable structures, generating extremely high temperatures at the contact point between the two plates, ultimately fusing them together. Therefore, it is imperative to carefully control and restrict the applied voltage range within this design, as illustrated in Figures 6.12-13.

The performance accuracy, as illustrated in Figure 6.13 has been rigorously validated through both analytical and numerical analyses. The results reveal a minimal disparity of only 0.6% between these two analytical approaches. When compared to the numerical analysis, the

experimental results closely aligned, demonstrating a slight difference of approximately 5%. Furthermore, the calculated capacitance change for the actuator was determined to be $18.5 \text{ fF}/\mu\text{m}$. These findings underscore the precision and reliability of the device's performance in the intended operational range.

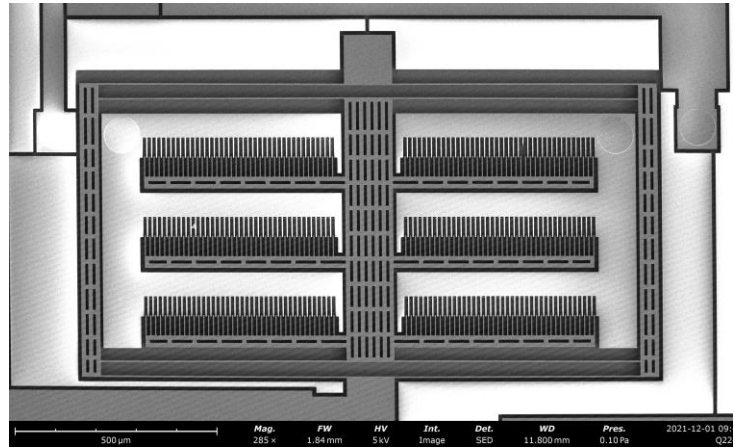


Figure 6.11: SEM image of MEMS electrostatic actuator.

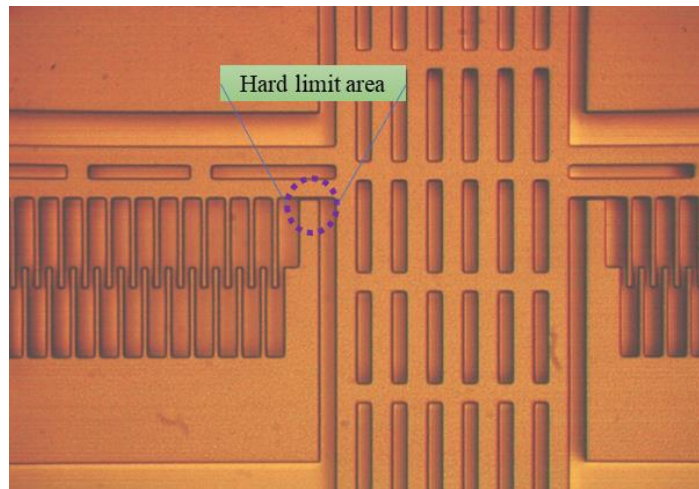


Figure 6.12: Electrostatic actuator when its applied maximum of 25 V.

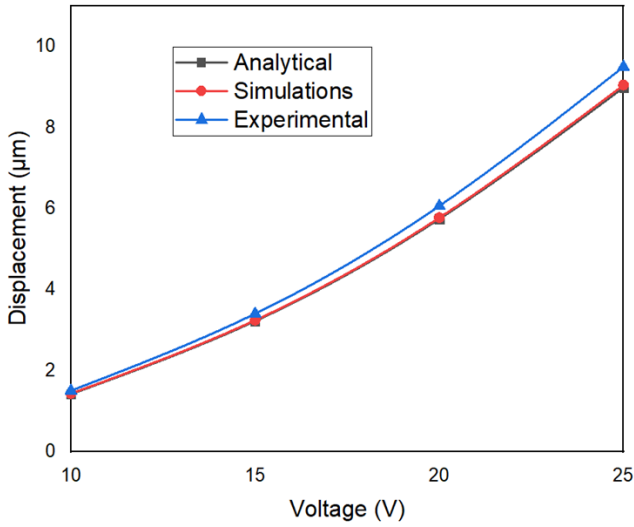


Figure 6.13: Electrostatic actuator performance comparison with analytically, numerically, and experimentally.

6.2.3 MEMS Based Tensile Testing Device

The MEMS-based tensile testing device was characterized at room temperature using the procedures mentioned above, with a voltage range of 1-5 volts (Figure 6.14). The results validate its suitability for characterizing diverse 2D materials.

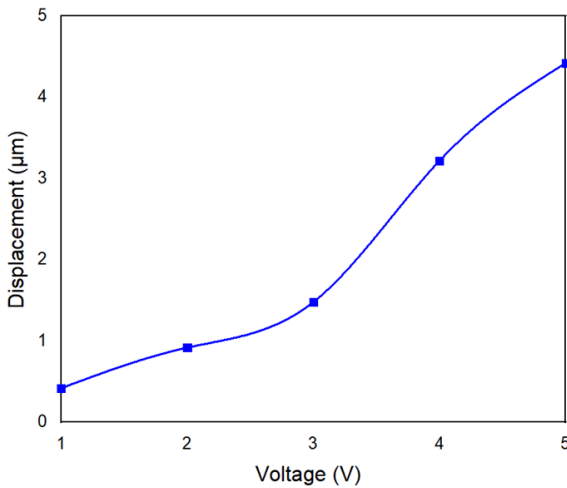


Figure 6.14: Experimental validation of MEMS based tensile testing device.

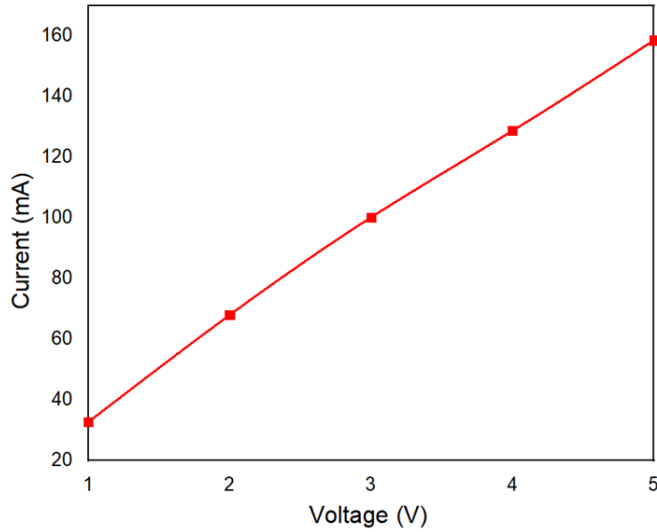


Figure 6.15: I-V curve (not linear fitting) measurements in MEMS based tensile testing device.

I-V measurements were conducted on the MEMS-based tensile testing device to characterize its electrical behavior. These measurements were essential for understanding how the actuator responds to varying electrical inputs, particularly in terms of its power consumption and heating capabilities. The I-V curve shows the relationship between the applied voltage (V) and the resulting current (I) passing through the thermal actuator. In these measurements, the I-V curve (Figure 6.15) exhibited a linear response, signifying a direct and proportional correlation between the applied voltage and the current passing through the actuator.

This linear I-V behavior is a desirable characteristic for thermal actuators, as it simplifies control and predictability. The linear relationship enables precise and straightforward modulation of the actuator's heating power by adjusting the applied voltage. As the voltage increases, the current passing through the V-beam thermal actuator also increases in a predictable manner.

6.3 Electrical Characterization in Low Temperature STM's vacuum chamber

The LT-STM ultra-high vacuum chamber (UHV) is hosted by the IMEM-CNR, Genova laboratory for conducting electrical characterization experiments. The objective of these experiments was to evaluate the performance of MEMS devices fabricated in the current research within the challenging conditions of a low-temperature, vacuum environment. In order to assess the functionality of the MEMS devices in a vacuum, initial tests were conducted to determine whether they exhibited similar performance characteristics to those observed in typical ambient air.

To gain a more comprehensive understanding of the behavior of these devices, multiple cooling cycles were employed within the vacuum chamber. The main goals of these cycles were: firstly, to evaluate the performance and functionality of the devices at low temperatures, which is crucial for their potential applications in low-temperature environments, and secondly, to closely examine the electrical connections and identify any issues related to the adhesion of the devices to the printed circuit board (PCB). Ensuring the stability of these connections and the overall reliability of the devices in a vacuum environment was of utmost importance.

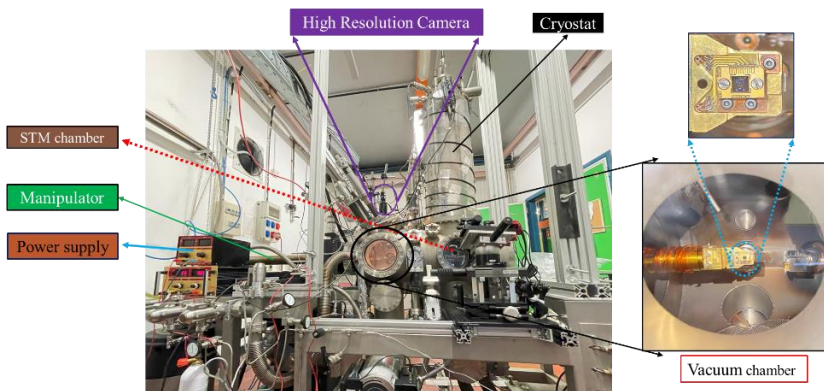


Figure. 6.16: Scanning tunneling microscopy tool setup overview.

Further investigations were carried out to verify whether silicon devices retained their mobility within the vacuum. Detailed observations were meticulously recorded in order to determine if the devices continued to function as intended inside the STM chamber. Figures 6.16 to 6.19 provide a comprehensive overview of the experimental setup used in the scanning tunneling microscope investigations. Figure 6.16 offers a detailed perspective of the scanning tunneling microscope (STM) that was utilized for the electrical characterization tests. The integration of a high-resolution camera that accessed the UHV chamber, which had a base pressure range of 10^{-7} mbar and 10^{-12} mbar, allowed for real-time monitoring of the experimental conditions. A cryostat that employed cryogenic coolant, such as liquid nitrogen, was used to establish controlled and low-temperature environments within the UHV chamber. Additionally, a power supply was employed to modulate the electrical parameters during the characterization tests. To ensure the secure and accurate handling of the samples, a manipulator was utilized to provide stability and reproducibility in positioning. This integrated setup, which consisted of an STM with visual monitoring, a cryostat for temperature control, a power supply for electrical modulation, and a manipulator with a PCB for precise sample handling, facilitated comprehensive electrical characterization tests under meticulously controlled conditions.

Figure 6.17 illustrates the changes in temperature over time during the controlled cooling process in the STM chamber. This visualization is essential for comprehending the behavior of the system's temperature, and the correlation between time and temperature provides significant insights. To achieve and maintain the desired low temperatures in the LT-STM chamber, the cooling process involves the addition of cryogenic coolant, such as liquid nitrogen. Initially, the system begins at a temperature of 290 K, and as the cryogenic coolant is gradually introduced, the temperature decreases. After 155 minutes, the system stabilizes at 178.93 K, indicating the successful establishment of the desired low-temperature environment.

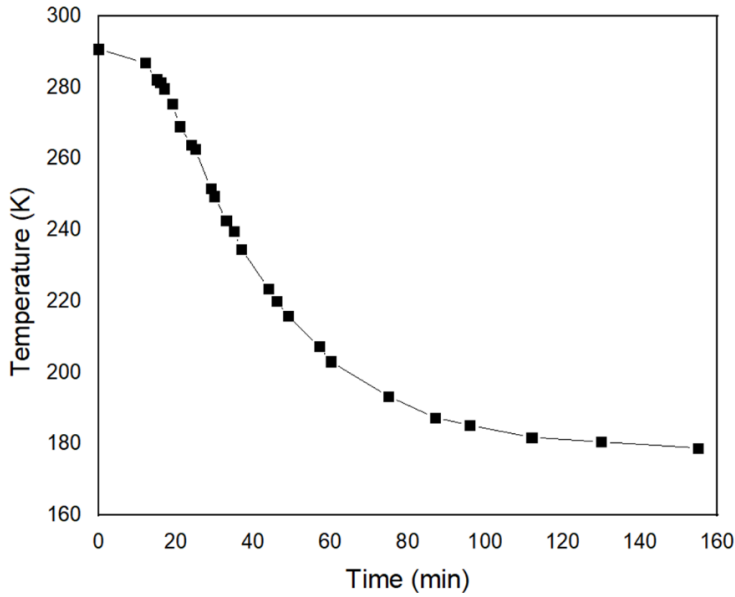


Figure 6.17: Temperatures vs time for chamber cooling.

In Figure 6.18, the focus is on the placement of Chip-1 within the vacuum environment of the STM chamber, particularly highlighting the specific device under investigation and its positioning. Finally, Figure 6.19 visually presents the configuration of Chip-2 within the vacuum environment of the STM chamber, providing a clear representation of the setup for the experiments conducted on the second device. The findings and insights obtained from these experiments on electrical characterization in the vacuum chamber of the STM are invaluable, as they play a crucial role in evaluating the feasibility of utilizing MEMS devices in low-temperature, vacuum conditions. These preliminary results offer valuable information regarding device performance, thermal behavior, and electrical connections under challenging environmental circumstances.

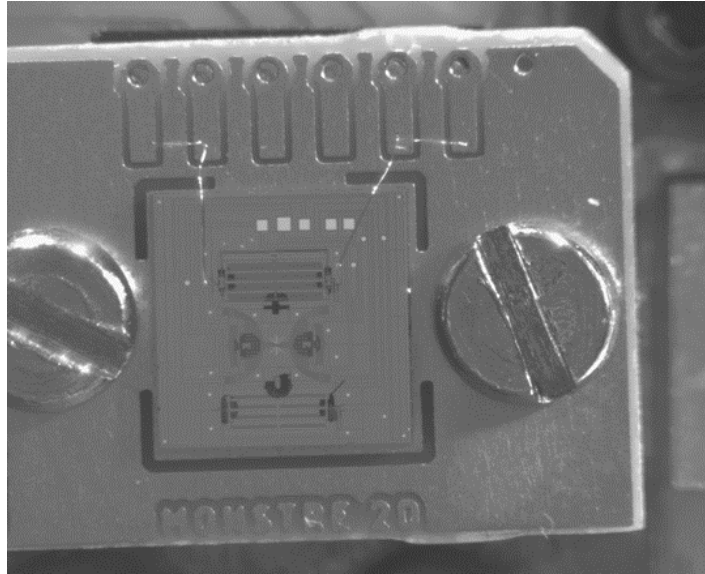


Figure 6.18: Chip-1 in STM's Vacuum Chamber.

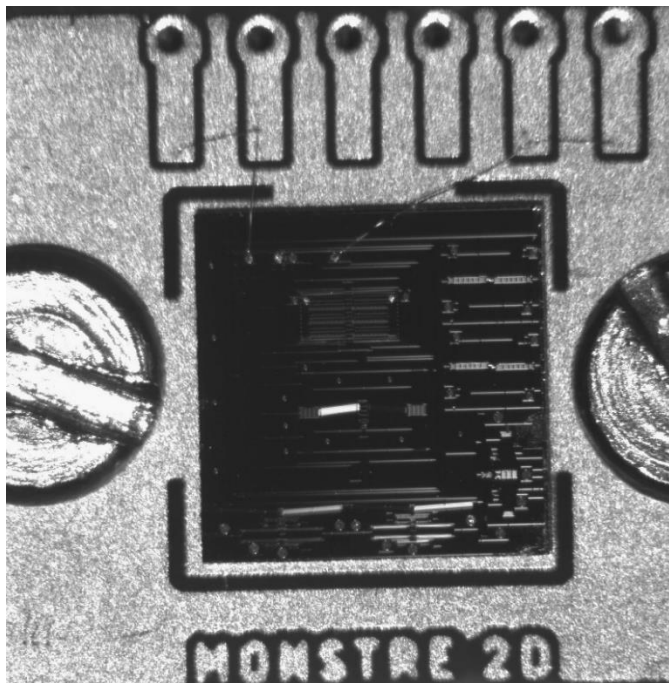


Figure 6.19: Chip-2 in Vacuum Environment.

Conclusions

Investigating the mechanical and electronic properties of 2D nanomaterials, such as graphene, under strain and at low temperatures is essential for comprehending their behavior and potential applications. This research addresses critical gaps in the existing literature, where high strain rates have not consistently been applied to these materials, and a lack of experimental data at low temperatures persists.

To bridge these gaps, four distinct MEMS-based devices have been successfully developed and characterized. The first device introduces on-chip actuation, sensing, and feedback control systems, allowing for controlled displacements of nanoscale specimens while minimizing temperature distribution. This integrated platform incorporates MEMS thermal actuators with an axial stiffness of 40253.6 N/m, which can induce a total displacement of 0.8 μm in the sample while maintaining a temperature increase of 80 $^{\circ}\text{C}$ within the sample area. Three capacitive sensors, featuring a calculated sensitivity of 5.2 fF/nm, are employed to measure the precise displacement delivered to the sample. Furthermore, various MEMS-based amplification mechanisms are designed and optimized, with the V-beam amplification mechanism amplifying displacement by a factor of approximately 50. The second device, termed the cascaded MEMS device, offers enhanced capabilities to measure stress-strain curves of 2D nanomaterials at low temperatures, aided by vertical V-shaped structures for displacement amplification. Analytical and numerical results exhibit a negligible difference of 1.7% between them. The third device, a MEMS electrostatic actuator, is specifically designed for conducting bending tests on silicon material properties at low temperatures. It allows for on-chip sample fabrication and provides accurate measurements of displacement delivery to the sample. When operated at 25 V, this electrostatic actuator is capable of generating a displacement of approximately 9 μm , with a calculated capacitance change of 18.5 fF/ μm . The accuracy of its performance is verified, revealing a minimal difference of 0.6% between analytical and numerical analyses, and the experimental results closely match the numerical analysis, with a difference of approximately 5%. Two MEMS rotational structures,

including a novel C-shaped structure, amplify movement and demonstrate superior displacement delivery. The geometric parameters of the C-shaped structure are optimized using the Design of Experiment (DOE) approach, and analytical modeling and simulations using the Finite Element Method predict its behavior with a 2.3% difference between them. Experimental characterization confirms that the novel C-shaped structure MEMS rotational structure exhibits a 28% improvement in delivered displacement compared to the symmetrical lancet structure.

All the designed MEMS devices are fabricated using bulk micromachining and deep reactive ion etching, and their underpass technology ensures electrical isolation within the platforms. The optimization of MEMS device fabrication for creating underpass structures on silicon-on-insulator (SOI) wafers is a critical aspect of this research. These underpasses serve the dual purpose of providing both electrical isolation and mechanical connections within MEMS devices. The fabrication process was systematically explored across two batches involving nine wafers.

Key findings emerged from the first batch, highlighting the need for an extended Surface Dielectric Etch (SDE) duration to achieve the desired underpass geometry. The optimized recipe on wafer 4 introduced a single-step SDE approach with a 70-minute duration. However, challenges arose during the subsequent HF vapor etching step due to the dimensions of the underpasses. This necessitated design adjustments to make the underpasses suitable for HF vapor etching. In the second batch of wafers, the optimization process continued, with a specific focus on understanding the relationship between etching time and underpass dimensions. The findings underscore the importance of iterative fine-tuning, revealing potential benefits stemming from unintentional feature size reductions, which were approximately 1.73 μm in the devices. Surprisingly, this reduction positively impacted device flexibility.

These discoveries contribute valuable insights into the fabrication process for MEMS devices, particularly in terms of underpass structures. Such structures are helpful for ensuring effective electrical

isolation and mechanical connections within SOI MEMS devices operating in low temperatures.

Future Work

The successful fabrication and initial findings of the MEMS devices mark a significant milestone in this research endeavor. In order to further advance our understanding and broaden the applicability of the developed MEMS technology, several key areas for future investigation have been identified. Firstly, future efforts will focus on subjecting the MEMS-based testing platform to low-temperature environments in order to validate its performance under extreme conditions and assess its compatibility with the intended specifications. These comprehensive tests will provide valuable insights into the robustness and functionality of the device in challenging thermal scenarios. Secondly, there is a need to extend the capabilities of the MEMS platform through the deposition of 2D nanomaterials. This presents a unique challenge due to the lack of anchored parts, where the materials deposition will take place. Overcoming this complexity will require innovative solutions for precise 2D material deposition. Once the integration of 2D nanomaterials is achieved, the next step involves thorough verification of the developed MEMS testing platforms. Once validated, these platforms can be utilized for diverse applications, particularly in the characterization of 2D material strain engineering. This represents a critical advancement in the field, providing researchers with a versatile tool to explore and manipulate the mechanical properties of 2D materials.

Lastly, the utilization of the MEMS electrostatic actuator in low-temperature experiments offers a unique opportunity to study the mechanical properties of silicon under such conditions. Future work should focus on leveraging this actuator in dedicated low-temperature experiments, which will provide valuable insights into the behavior of silicon.

Appendix

List of Publications associated with the current research work:

1. Design and simulation of a MEMS device to investigate the strain engineering properties of 2D nanomaterials. 2021 Symposium on Design, Test, Integration and Packaging of MEMS and MOEMS, DTIP 2021. <https://doi.org/10.1109/DTIP54218.2021.9568495>
2. Optimization of an amplification mechanism enabling large displacements in MEMS-based nanomaterial testing devices. Micro and Nano Engineering, 15. <https://doi.org/10.1016/j.mne.2022.100131>.
3. A C-shaped hinge for displacement magnification in MEMS rotational structures, Microsystems & Nanoengineering, Nature Journal. <https://doi.org/10.1038/s41378-023-00618-9> .

Bibliography

- [1] K. S. Novoselov *et al.*, ‘Electric field in atomically thin carbon films’, *Science (1979)*, vol. 306, no. 5696, pp. 666–669, Oct. 2004, doi: 10.1126/science.1102896.
- [2] K. S. Novoselov *et al.*, ‘Two-dimensional atomic crystals’, 2005. [Online]. Available: <https://www.pnas.org>
- [3] K. S. Novoselov, A. Mishchenko, A. Carvalho, and A. H. Castro Neto, ‘2D materials and van der Waals heterostructures’, *Science*, vol. 353, no. 6298. American Association for the Advancement of Science, Jul. 29, 2016. doi: 10.1126/science.aac9439.
- [4] K. F. Mak, C. Lee, J. Hone, J. Shan, and T. F. Heinz, ‘Atomically thin MoS₂: A new direct-gap semiconductor’, *Phys Rev Lett*, vol. 105, no. 13, Sep. 2010, doi: 10.1103/PhysRevLett.105.136805.
- [5] S. Singh, K. Verma, and C. Prakash, ‘Materials Horizons: From Nature to Nanomaterials Advanced Applications of 2D Nanostructures Emerging Research and Opportunities’. [Online]. Available: <http://www.springer.com/series/16122>
- [6] J. Kang, W. Cao, X. Xie, D. Sarkar, W. Liu, and K. Banerjee, ‘Graphene and beyond-graphene 2D crystals for next-generation green electronics’, in *Micro- and Nanotechnology Sensors, Systems, and Applications VI*, SPIE, Jun. 2014, p. 908305. doi: 10.1117/12.2051198.
- [7] C. Meng, P. Das, X. Shi, Q. Fu, K. Müllen, and Z.-S. Wu, ‘In Situ and Operando Characterizations of 2D Materials in Electrochemical Energy Storage Devices’, *Small Science*, vol. 1, no. 4, p. 2000076, Apr. 2021, doi: 10.1002/smsc.202000076.
- [8] A. K. Geim, ‘Graphene: Status and Prospects’. [Online]. Available: www.sciencemag.org
- [9] B. Aïssa, N. K. Memon, A. Ali, and M. K. Khraisheh, ‘Recent progress in the growth and applications of graphene as a smart material: A review’, *Frontiers in Materials*, vol. 2. Frontiers Media S.A., Sep. 22, 2015. doi: 10.3389/fmats.2015.00058.

- [10] S. K. Tiwari, V. Kumar, A. Huczko, R. Oraon, A. De Adhikari, and G. C. Nayak, 'Magical Allotropes of Carbon: Prospects and Applications', *Critical Reviews in Solid State and Materials Sciences*, vol. 41, no. 4. Taylor and Francis Inc., pp. 257–317, Jul. 03, 2016. doi: 10.1080/10408436.2015.1127206.
- [11] S. K. Tiwari, R. K. Mishra, S. K. Ha, and A. Huczko, 'Evolution of Graphene Oxide and Graphene: From Imagination to Industrialization', *ChemNanoMat*, vol. 4, no. 7. Wiley-VCH Verlag, pp. 598–620, Jul. 01, 2018. doi: 10.1002/cnma.201800089.
- [12] S. M. A. Aftab, R. B. Shaikh, B. Saifullah, M. Z. Hussein, and K. A. Ahmed, 'Aerospace applications of graphene nanomaterials', in *AIP Conference Proceedings*, American Institute of Physics Inc., Mar. 2019. doi: 10.1063/1.5094312.
- [13] Y. Fu *et al.*, 'Graphene related materials for thermal management', *2d Mater*, vol. 7, no. 1, 2020, doi: 10.1088/2053-1583/ab48d9.
- [14] K. Zeranska *et al.*, 'Graphene-Based Thermoplastic Composites as Extremely Broadband and Frequency-Dependent EMI Absorbers for Multifunctional Applications', *ACS Appl Electron Mater*, vol. 4, no. 9, pp. 4463–4470, Sep. 2022, doi: 10.1021/acsaelm.2c00722.
- [15] G. Jena and J. Philip, 'A review on recent advances in graphene oxide-based composite coatings for anticorrosion applications', *Prog Org Coat*, vol. 173, p. 107208, Dec. 2022, doi: 10.1016/J.PORGCOAT.2022.107208.
- [16] L. Li, M. Chakik, and R. Prakash, 'A review of corrosion in aircraft structures and graphene-based sensors for advanced corrosion monitoring', *Sensors*, vol. 21, no. 9. MDPI AG, May 01, 2021. doi: 10.3390/s21092908.
- [17] A. Chakraborty, S. Nuthalapati, A. Nag, N. Afsarimanesh, M. E. E. Alahi, and M. E. Altinsoy, 'A Critical Review of the Use of Graphene-Based Gas Sensors', *Chemosensors*, vol. 10, no. 9. MDPI, Sep. 01, 2022. doi: 10.3390/chemosensors10090355.
- [18] J. H. Choi, J. Lee, M. Byeon, T. E. Hong, H. Park, and C. Y. Lee, 'Graphene-Based Gas Sensors with High Sensitivity and

- Minimal Sensor-to-Sensor Variation’, *ACS Appl Nano Mater*, vol. 3, no. 3, pp. 2257–2265, Mar. 2020, doi: 10.1021/acsanm.9b02378.
- [19] M. Hernaez, ‘Applications of graphene-based materials in sensors’, *Sensors (Switzerland)*, vol. 20, no. 11. MDPI AG, Jun. 01, 2020. doi: 10.3390/s20113196.
- [20] J. Zhu, D. Yang, Z. Yin, Q. Yan, and H. Zhang, ‘Graphene and graphene-based materials for energy storage applications’, *Small*, vol. 10, no. 17. Wiley-VCH Verlag, pp. 3480–3498, Sep. 10, 2014. doi: 10.1002/smll.201303202.
- [21] Y. Yang, A. M. Asiri, Z. Tang, D. Du, and Y. Lin, ‘Graphene based materials for biomedical applications’, *Materials Today*, vol. 16, no. 10, pp. 365–373, Oct. 2013, doi: 10.1016/J.MATTOD.2013.09.004.
- [22] T. Das, B. K. Sharma, A. K. Katiyar, and J. H. Ahn, ‘Graphene-based flexible and wearable electronics’, *Journal of Semiconductors*, vol. 39, no. 1, Jan. 2018, doi: 10.1088/1674-4926/39/1/011007.
- [23] O. Alnoor *et al.*, ‘Graphene oxide-based membranes for water purification applications: Effect of plasma treatment on the adhesion and stability of the synthesized membranes’, *Membranes (Basel)*, vol. 10, no. 10, pp. 1–15, Oct. 2020, doi: 10.3390/membranes10100292.
- [24] S. Roy *et al.*, ‘Structure, Properties and Applications of Two-Dimensional Hexagonal Boron Nitride’, *Advanced Materials*, vol. 33, no. 44. John Wiley and Sons Inc, Nov. 01, 2021. doi: 10.1002/adma.202101589.
- [25] G. R. Bhimanapati, N. R. Glavin, and J. A. Robinson, ‘2D Boron Nitride: Synthesis and Applications’, *Semiconductors and Semimetals*, vol. 95, pp. 101–147, Jan. 2016, doi: 10.1016/BS.SEMSEM.2016.04.004.
- [26] Z. Zhang, S. Hu, J. Chen, and B. Li, ‘Hexagonal boron nitride: A promising substrate for graphene with high heat dissipation’, *Nanotechnology*, vol. 28, no. 22, May 2017, doi: 10.1088/1361-6528/aa6e49.

- [27] S. Ogawa, S. Fukushima, and M. Shimatani, 'Hexagonal Boron Nitride for Photonic Device Applications: A Review', *Materials*, vol. 16, no. 5. MDPI, Mar. 01, 2023. doi: 10.3390/ma16052005.
- [28] J. Wang, F. Ma, and M. Sun, 'Graphene, hexagonal boron nitride, and their heterostructures: properties and applications', *RSC Advances*, vol. 7, no. 27. Royal Society of Chemistry, pp. 16801–16822, 2017. doi: 10.1039/c7ra00260b.
- [29] Q. Peng, W. Ji, and S. De, 'Mechanical properties of the hexagonal boron nitride monolayer: Ab initio study', *Comput Mater Sci*, vol. 56, pp. 11–17, Apr. 2012, doi: 10.1016/J.COMMATSCI.2011.12.029.
- [30] H. Yanar, G. Purcek, M. Demirtas, and H. H. Ayar, 'Effect of hexagonal boron nitride (h-BN) addition on friction behavior of low-steel composite brake pad material for railway applications', *Tribol Int*, vol. 165, p. 107274, Jan. 2022, doi: 10.1016/J.TRIBOINT.2021.107274.
- [31] S. Manzeli, D. Ovchinnikov, D. Pasquier, O. V. Yazyev, and A. Kis, '2D transition metal dichalcogenides', *Nature Reviews Materials*, vol. 2. Nature Publishing Group, Jun. 13, 2017. doi: 10.1038/natrevmats.2017.33.
- [32] B. Radisavljevic, A. Radenovic, J. Brivio, V. Giacometti, and A. Kis, 'Single-layer MoS₂ transistors', *Nat Nanotechnol*, vol. 6, no. 3, pp. 147–150, 2011, doi: 10.1038/nnano.2010.279.
- [33] V. P. Kumar and D. K. Panda, 'Review—Next Generation 2D Material Molybdenum Disulfide (MoS₂): Properties, Applications and Challenges', *ECS Journal of Solid State Science and Technology*, vol. 11, no. 3, p. 033012, Mar. 2022, doi: 10.1149/2162-8777/ac5a6f.
- [34] A. Kumar, A. Sood, and S. S. Han, 'Molybdenum disulfide (MoS₂)-based nanostructures for tissue engineering applications: prospects and challenges', *Journal of Materials Chemistry B*, vol. 10, no. 15. Royal Society of Chemistry, pp. 2761–2780, Mar. 08, 2022. doi: 10.1039/d2tb00131d.
- [35] Z. Gu *et al.*, 'The molecular mechanism of robust macrophage immune responses induced by PEGylated molybdenum

- disulfide’, *Nanoscale*, vol. 11, no. 46, pp. 22293–22304, Dec. 2019, doi: 10.1039/c9nr04358f.
- [36] H. Iwai, K. Kakushima’, and H. Wong, ‘CHALLENGES FOR FUTURE SEMICONDUCTOR MANUFACTURING’, 2006. [Online]. Available: www.worldscientific.com
- [37] G. Y. Zhao *et al.*, ‘Recent progress on irradiation-induced defect engineering of two-dimensional 2H-MoS₂ few layers’, *Applied Sciences (Switzerland)*, vol. 9, no. 4, Feb. 2019, doi: 10.3390/app9040678.
- [38] O. Samy, S. Zeng, M. D. Birowosuto, and A. El Moutaouakil, ‘A review on MoS₂ properties, synthesis, sensing applications and challenges’, *Crystals (Basel)*, vol. 11, no. 4, 2021, doi: 10.3390/cryst11040355.
- [39] Y. Zhao, Y. Chen, Y. H. Zhang, and S. F. Liu, ‘Recent advance in black phosphorus: Properties and applications’, *Mater Chem Phys*, vol. 189, pp. 215–229, Mar. 2017, doi: 10.1016/J.MATCHEMPHYS.2016.12.014.
- [40] J. R. Choi *et al.*, ‘Black phosphorus and its biomedical applications’, *Theranostics*, vol. 8, no. 4. Ivyspring International Publisher, pp. 1005–1026, 2018. doi: 10.7150/thno.22573.
- [41] J. Mei, T. Liao, and Z. Sun, ‘Opportunities and Challenges of Black Phosphorus for Electrocatalysis and Rechargeable Batteries’, *Adv Sustain Syst*, vol. 6, no. 12, Dec. 2022, doi: 10.1002/adsu.202200301.
- [42] I. Rajender, B. Abdullah, and M. Asiri Editors, ‘Engineering Materials Black Phosphorus Synthesis, Properties and Applications’. [Online]. Available: <http://www.springer.com/series/4288>
- [43] A. Zurutuza and C. Marinelli, ‘Challenges and opportunities in graphene commercialization’, *Nature Nanotechnology*, vol. 9, no. 10. Nature Publishing Group, pp. 730–734, Jan. 01, 2014. doi: 10.1038/nnano.2014.225.
- [44] N. R. Pradhan, B. H. Moon, and S. K. Behura, ‘Preface on:“Challenges and Opportunities for 2D Materials and Heterostructure Devices”’, *Emergent Materials*, vol. 4, no. 4.

- Springer Nature, pp. 811–812, Aug. 01, 2021. doi: 10.1007/s42247-021-00272-9.
- [45] S. Yang, Y. Chen, and C. Jiang, ‘Strain engineering of two-dimensional materials: Methods, properties, and applications’, *InfoMat*, vol. 3, no. 4. Blackwell Publishing Ltd, pp. 397–420, Apr. 01, 2021. doi: 10.1002/inf2.12177.
- [46] M. Pandey, C. Pandey, R. Ahuja, and R. Kumar, ‘Straining techniques for strain engineering of 2D materials towards flexible straintronic applications’, *Nano Energy*, vol. 109, p. 108278, May 2023, doi: 10.1016/J.NANOEN.2023.108278.
- [47] S. Deng, A. V. Sumant, and V. Berry, ‘Strain engineering in two-dimensional nanomaterials beyond graphene’, *Nano Today*, vol. 22, pp. 14–35, Oct. 2018, doi: 10.1016/J.NANTOD.2018.07.001.
- [48] X. Xu, T. Liang, D. Kong, B. Wang, and L. Zhi, ‘Strain engineering of two-dimensional materials for advanced electrocatalysts’, *Mater Today Nano*, vol. 14, p. 100111, Jun. 2021, doi: 10.1016/J.MTNANO.2021.100111.
- [49] Y. Han *et al.*, ‘Experimental nanomechanics of 2D materials for strain engineering’, *Applied Nanoscience (Switzerland)*, vol. 11, no. 4. Springer Science and Business Media Deutschland GmbH, pp. 1075–1091, Apr. 01, 2021. doi: 10.1007/s13204-021-01702-0.
- [50] E. D. Klema, F. K. McGowan, J. W. Beams, W. E. Walker, and H. S. Morton, ‘Gamma-Gamma Angular Correlation in Cd 114 Mechanical Properties of Thin Films of Silver*’, 1946.
- [51] G. Wang *et al.*, ‘Measuring interlayer shear stress in bilayer graphene’, *Phys Rev Lett*, vol. 119, no. 3, Jul. 2017, doi: 10.1103/PhysRevLett.119.036101.
- [52] R. I. Tanner and E. Tanner, ‘Heinrich Hencky: A rheological pioneer’, *Rheol Acta*, vol. 42, no. 1, pp. 93–101, Jan. 2003, doi: 10.1007/s00397-002-0259-6.
- [53] S. P. Koenig, N. G. Boddeti, M. L. Dunn, and J. S. Bunch, ‘Ultrastrong adhesion of graphene membranes’, *Nat Nanotechnol*, vol. 6, no. 9, pp. 543–546, 2011, doi: 10.1038/nnano.2011.123.

- [54] G. Wang *et al.*, ‘Bending of Multilayer van der Waals Materials’, *Phys Rev Lett*, vol. 123, no. 11, Sep. 2019, doi: 10.1103/PhysRevLett.123.116101.
- [55] J. U. Lee, D. Yoon, and H. Cheong, ‘Estimation of young’s modulus of graphene by Raman spectroscopy’, *Nano Lett*, vol. 12, no. 9, pp. 4444–4448, Sep. 2012, doi: 10.1021/nl301073q.
- [56] J. S. Bunch *et al.*, ‘Impermeable atomic membranes from graphene sheets’, *Nano Lett*, vol. 8, no. 8, pp. 2458–2462, Aug. 2008, doi: 10.1021/nl801457b.
- [57] J. O. Carneiro, J. P. Alpuim, and V. Teixeira, ‘Experimental bending tests and numerical approach to determine the fracture mechanical properties of thin ceramic coatings deposited by magnetron sputtering’, *Surf Coat Technol*, vol. 200, no. 8, pp. 2744–2752, Jan. 2006, doi: 10.1016/J.SURFCOAT.2004.11.010.
- [58] F. P. (Ferdinand P. Beer, *Mechanics of materials*. McGraw-Hill, 2011.
- [59] G. Tsoukleri *et al.*, ‘Subjecting a graphene monolayer to tension and compression’, *Small*, vol. 5, no. 21, pp. 2397–2402, Nov. 2009, doi: 10.1002/sml.200900802.
- [60] R. Roldán, A. Castellanos-Gomez, E. Cappelluti, and F. Guinea, ‘Strain engineering in semiconducting two-dimensional crystals’, *Journal of Physics Condensed Matter*, vol. 27, no. 31. Institute of Physics Publishing, Aug. 12, 2015. doi: 10.1088/0953-8984/27/31/313201.
- [61] H. J. Conley, B. Wang, J. I. Ziegler, R. F. Haglund, S. T. Pantelides, and K. I. Bolotin, ‘Bandgap engineering of strained monolayer and bilayer MoS₂’, *Nano Lett*, vol. 13, no. 8, pp. 3626–3630, Aug. 2013, doi: 10.1021/nl4014748.
- [62] H. Zhang *et al.*, ‘Atomic force microscopy for two-dimensional materials: A tutorial review’, *Opt Commun*, vol. 406, pp. 3–17, Jan. 2018, doi: 10.1016/J.OPTCOM.2017.05.015.
- [63] K. K. Al-Quraishi, Q. He, W. Kauppila, M. Wang, and Y. Yang, ‘Mechanical testing of two-dimensional materials: a brief review’, *International Journal of Smart and Nano Materials*.

- Taylor and Francis Ltd., pp. 207–246, 2020. doi: 10.1080/19475411.2020.1791276.
- [64] C. Lee, X. Wei, J. W. Kysar, and J. Hone, ‘Measurement of the Elastic Properties and Intrinsic Strength of Monolayer Graphene’, *Source: Science, New Series*, vol. 321, no. 5887, pp. 385–388, 2008, doi: 10.1126/science.1156211.
- [65] H. H. Pérez Garza, E. W. Kievit, G. F. Schneider, and U. Staufer, ‘Controlled, reversible, and nondestructive generation of uniaxial extreme strains (>10%) in graphene’, *Nano Lett*, vol. 14, no. 7, pp. 4107–4113, Jul. 2014, doi: 10.1021/nl5016848.
- [66] J. W. Christopher *et al.*, ‘Monolayer MoS₂ Strained to 1.3% with a Microelectromechanical System’, Mar. 2018, [Online]. Available: <http://arxiv.org/abs/1803.02787>
- [67] Y. Lu and J. Lou, ‘Overview Nanomechanics: Theory and Experiments Quantitative In-situ Nanomechanical Characterization of Metallic Nanowires’. [Online]. Available: www.tms.org/jom.html
- [68] IEEE Electron Devices Society and Institute of Electrical and Electronics Engineers, *2019 20th International Conference on Solid-State Sensors, Actuators and Microsystems & Eurosensors XXXIII (TRANSDUCERS & EUROSENSORS XXXIII)*.
- [69] X. Li, M. Sun, C. Shan, Q. Chen, and X. Wei, ‘Mechanical Properties of 2D Materials Studied by In Situ Microscopy Techniques’, *Advanced Materials Interfaces*, vol. 5, no. 5. Wiley-VCH Verlag, Mar. 09, 2018. doi: 10.1002/admi.201701246.
- [70] C. Gómez-Navarro, M. Burghard, and K. Kern, ‘Elastic properties of chemically derived single graphene sheets’, *Nano Lett*, vol. 8, no. 7, pp. 2045–2049, Jul. 2008, doi: 10.1021/nl801384y.
- [71] C. Zhang, K. L. Firestein, J. F. S. Fernando, D. Siriwardena, J. E. von Treifeldt, and D. Golberg, ‘Recent Progress of In Situ Transmission Electron Microscopy for Energy Materials’, *Advanced Materials*, vol. 32, no. 18. Wiley-VCH Verlag, May 01, 2020. doi: 10.1002/adma.201904094.

- [72] C. Jiang, H. Lu, H. Zhang, Y. Shen, and Y. Lu, ‘Recent Advances on In Situ SEM Mechanical and Electrical Characterization of Low-Dimensional Nanomaterials’, *Scanning*, vol. 2017. Hindawi Limited, 2017. doi: 10.1155/2017/1985149.
- [73] T. Filleter and A. M. Beese, ‘In Situ Transmission Electron Microscopy: Mechanical Testing’, in *Encyclopedia of Nanotechnology*, Springer Netherlands, 2015, pp. 1–12. doi: 10.1007/978-94-007-6178-0_100990-1.
- [74] C. Li, G. Cheng, & H. Wang, and Y. Zhu, ‘Microelectromechanical Systems for Nanomechanical Testing: Displacement- and Force-Controlled Tensile Testing with Feedback Control’, doi: 10.1007/s11340-020-00619-z/Published.
- [75] X. Wang *et al.*, ‘MEMS device for quantitative in situ mechanical testing in electron microscope’, *Micromachines (Basel)*, vol. 8, no. 2, 2017, doi: 10.3390/mi8020031.
- [76] J. W. Christopher *et al.*, ‘Monolayer MoS₂ Strained to 1.3% with a Microelectromechanical System’, Mar. 2018, [Online]. Available: <http://arxiv.org/abs/1803.02787>
- [77] IEEE Electron Devices Society and Institute of Electrical and Electronics Engineers, *2019 20th International Conference on Solid-State Sensors, Actuators and Microsystems & Eurosensors XXXIII (TRANSDUCERS & EUROSENSORS XXXIII)*.
- [78] P. Zhang *et al.*, ‘Fracture toughness of graphene’, *Nat Commun*, vol. 5, Apr. 2014, doi: 10.1038/ncomms4782.
- [79] Q. Yu, M. Legros, and A. M. Minor, ‘In situ TEM nanomechanics’, *MRS Bulletin*, vol. 40, no. 1. Materials Research Society, pp. 62–68, Jan. 13, 2015. doi: 10.1557/mrs.2014.306.
- [80] U. Weierstall, ‘Low-Temperature Scanning Tunneling Microscopy’.
- [81] R. Decker *et al.*, ‘Local electronic properties of graphene on a BN substrate via scanning tunneling microscopy’, *Nano Lett*,

- vol. 11, no. 6, pp. 2291–2295, Jun. 2011, doi: 10.1021/nl2005115.
- [82] A. Pradeepkumar, D. K. Gaskill, and F. Iacopi, ‘Electronic and transport properties of epitaxial graphene on SiC and 3C-SiC/Si: A review’, *Applied Sciences (Switzerland)*, vol. 10, no. 12. MDPI AG, pp. 1–32, Jun. 01, 2020. doi: 10.3390/app10124350.
- [83] R. J. Nichols, ‘STM studies of electron transfer through single molecules at electrode-electrolyte interfaces’, *Electrochim Acta*, vol. 387, p. 138497, Aug. 2021, doi: 10.1016/J.ELECTACTA.2021.138497.
- [84] S. Kano, T. Tada, and Y. Majima, ‘Nanoparticle characterization based on STM and STS’, *Chemical Society Reviews*, vol. 44, no. 4. Royal Society of Chemistry, pp. 970–987, Feb. 21, 2015. doi: 10.1039/c4cs00204k.
- [85] O. Marti, G. Binnig, H. Rohrer, and H. Salemink, ‘Low-temperature scanning tunneling microscope’, *Surf Sci*, vol. 181, no. 1–2, pp. 230–234, Mar. 1987, doi: 10.1016/0039-6028(87)90163-4.
- [86] W. Tao *et al.*, ‘A low-temperature scanning tunneling microscope capable of microscopy and spectroscopy in a Bitter magnet at up to 34 T’, *Review of Scientific Instruments*, vol. 88, no. 9, Sep. 2017, doi: 10.1063/1.4995372.
- [87] J. A. Stroscio, R. J. Celotta, S. Blankenship, E. Hudson, and A. P. Fein, ‘Fig. 1: CAD drawing of the NanoPhysics System. Cryostat Metal MBE III-V MBE STM Loading A Low Temperature STM System for the Study of Quantum and Spin Electronic Systems*’.
- [88] S. Zhang, D. Huang, and S. Wu, ‘A cryogen-free low temperature scanning tunneling microscope capable of inelastic electron tunneling spectroscopy’, *Review of Scientific Instruments*, vol. 87, no. 6, Jun. 2016, doi: 10.1063/1.4952577.
- [89] P. Li *et al.*, ‘In situ microscopy techniques for characterizing the mechanical properties and deformation behavior of two-dimensional (2D) materials’, *Materials Today*, vol. 51, pp. 247–272, Dec. 2021, doi: 10.1016/J.MATTOD.2021.10.009.

- [90] N. R. Glavin, C. Muratore, and M. Snure, ‘Toward 2D materials for flexible electronics: opportunities and outlook’, *Oxford Open Materials Science*, vol. 1, no. 1, Nov. 2020, doi: 10.1093/oxfmat/itaa002.
- [91] Y. Sun and K. Liu, ‘Strain engineering in functional 2-dimensional materials’, *Journal of Applied Physics*, vol. 125, no. 8. American Institute of Physics Inc., Feb. 28, 2019. doi: 10.1063/1.5053795.
- [92] M. F. Pantano and I. Kuljanishvili, ‘Advances in mechanical characterization of 1D and 2D nanomaterials: progress and prospects’, *Nano Express*, vol. 1, no. 2, p. 022001, Sep. 2020, doi: 10.1088/2632-959x/abb43e.
- [93] J. J. Brown, A. I. Baca, K. A. Bertness, D. A. Dikin, R. S. Ruoff, and V. M. Bright, ‘Tensile measurement of single crystal gallium nitride nanowires on MEMS test stages’, *Sens Actuators A Phys*, vol. 166, no. 2, pp. 177–186, Apr. 2011, doi: 10.1016/j.sna.2010.04.002.
- [94] J. Qu and X. Liu, ‘MEMS-Based Platforms for Multi-Physical Characterization of Nanomaterials: A Review’, *IEEE Sens J*, vol. 22, no. 3, pp. 1827–1841, Feb. 2022, doi: 10.1109/JSEN.2021.3135888.
- [95] M. F. Pantano, R. A. Bernal, L. Pagnotta, and H. D. Espinosa, ‘Multiphysics design and implementation of a microsystem for displacement-controlled tensile testing of nanomaterials’, *Meccanica*, vol. 50, no. 2, pp. 549–560, Dec. 2015, doi: 10.1007/s11012-014-9950-9.
- [96] N. M. Kommanaboina, M. F. Pantano, and A. Bagolini, ‘Design and simulation of a MEMS device to investigate the strain engineering properties of 2D nanomaterials’, in *2021 Symposium on Design, Test, Integration & Packaging of MEMS and MOEMS (DTIP)*, IEEE, Aug. 2021, pp. 01–06. doi: 10.1109/DTIP54218.2021.9568495.
- [97] N. M. Kommanaboina, M. F. Pantano, and A. Bagolini, ‘Optimization of an amplification mechanism enabling large displacements in MEMS-based nanomaterial testing devices’, *Micro and Nano Engineering*, vol. 15, Jun. 2022, doi: 10.1016/j.mne.2022.100131.

- [98] M. F. Pantano and N. M. Pugno, ‘Design of a bent beam electrothermal actuator for in situ tensile testing of ceramic nanostructures’, *J Eur Ceram Soc*, vol. 34, no. 11, pp. 2767–2773, 2014, doi: 10.1016/j.jeurceramsoc.2013.12.001.
- [99] M. Tecpoyotl-T., P. Vargas Ch., S. Koshevaya, R. Cabello-R., A. Ocampo-D., and J. G. Vera-D., ‘Design and simulation of a MEM pressure microgripper based on electrothermal microactuators’, in *Thin Films for Solar and Energy Technology VIII*, SPIE, Sep. 2016, p. 99360I. doi: 10.1117/12.2237533.
- [100] N. M. Kommanaboina, M. F. Pantano, and A. Bagolini, ‘Design and simulation of a MEMS device to investigate the strain engineering properties of 2D nanomaterials’, in *2021 Symposium on Design, Test, Integration and Packaging of MEMS and MOEMS, DTIP 2021*, Institute of Electrical and Electronics Engineers Inc., Aug. 2021. doi: 10.1109/DTIP54218.2021.9568495.
- [101] Q. Qin and Y. Zhu, ‘Temperature control in thermal microactuators with applications to in-situ nanomechanical testing’, *Appl Phys Lett*, vol. 102, no. 1, Jan. 2013, doi: 10.1063/1.4773359.
- [102] R. Crescenzi, M. Balucani, and N. P. Belfiore, ‘Operational characterization of CSFH MEMS technology based hinges’, *Journal of Micromechanics and Microengineering*, vol. 28, no. 5, Mar. 2018, doi: 10.1088/1361-6439/aaaf31.
- [103] S. Iqbal, A. A. Malik, and R. I. Shakoor, ‘Design and analysis of novel micro displacement amplification mechanism actuated by chevron shaped thermal actuators’, *Microsystem Technologies*, vol. 25, no. 3, pp. 861–875, Mar. 2019, doi: 10.1007/s00542-018-4078-9.
- [104] N. Lobontiu and E. Garcia, ‘Analytical model of displacement amplification and stiffness optimization for a class of flexure-based compliant mechanisms’, *Comput Struct*, vol. 81, no. 32, pp. 2797–2810, Dec. 2003, doi: 10.1016/j.compstruc.2003.07.003.
- [105] X. Li *et al.*, ‘Design of a large displacement thermal actuator with a cascaded V-beam amplification for MEMS safety-and-

- arming devices’, *Microsystem Technologies*, vol. 21, no. 11, pp. 2367–2374, Nov. 2015, doi: 10.1007/s00542-015-2447-1.
- [106] Institute of Electrical and Electronics Engineers., *Sensors 2010 Hawaii : IEEE Sensors 2010 Conference : November 1-4, 2010, Waikoloa, Big Island, Hawaii*. IEEE, 2010.
- [107] S. Iqbal, R. I. Shakoor, Y. Lai, A. M. Malik, and S. A. Bazaz, ‘Experimental evaluation of force and amplification factor of three different variants of flexure based micro displacement amplification mechanism’, *Microsystem Technologies*, vol. 25, no. 7, pp. 2889–2906, Jul. 2019, doi: 10.1007/s00542-019-04313-6.
- [108] S. Iqbal, R. I. Shakoor, H. N. Gilani, H. Abbas, and A. M. Malik, ‘Performance Analysis of Microelectromechanical System Based Displacement Amplification Mechanism’, *Iranian Journal of Science and Technology - Transactions of Mechanical Engineering*, vol. 43, no. 3, pp. 507–528, Sep. 2019, doi: 10.1007/s40997-018-0213-6.
- [109] E. Davies, D. S. George, M. C. Gower, and A. S. Holmes, ‘MEMS Fabry-Pérot optical accelerometer employing mechanical amplification via a V-beam structure’, *Sens Actuators A Phys*, vol. 215, pp. 22–29, Aug. 2014, doi: 10.1016/j.sna.2013.08.002.
- [110] X. Shen and X. Chen, ‘Mechanical performance of a cascaded V-shaped electrothermal actuator’, *Int J Adv Robot Syst*, vol. 10, Nov. 2013, doi: 10.5772/56786.
- [111] L. Que, J.-S. Park, and Y. B. Gianchandani, ‘Bent-Beam Electrothermal Actuators-Part I: Single Beam and Cascaded Devices’, 2001.
- [112] J.-S. Park, L. L. Chu, A. D. Oliver, and Y. B. Gianchandani, ‘Bent-Beam Electrothermal Actuators-Part II: Linear and Rotary Microengines’, 2001.
- [113] Y. Zhang, Q. A. Huang, R. G. Li, and W. Li, ‘Macro-modeling for polysilicon cascaded bent beam electrothermal microactuators’, *Sens Actuators A Phys*, vol. 128, no. 1, pp. 165–175, Mar. 2006, doi: 10.1016/j.sna.2005.12.033.

- [114] Y. Zhang *et al.*, ‘A MEMS tensile testing device for mechanical characterization of individual nanowires’, in *Proceedings of IEEE Sensors*, 2010, pp. 2581–2584. doi: 10.1109/ICSENS.2010.5690164.
- [115] C. Li, D. Zhang, G. Cheng, and Y. Zhu, ‘Microelectromechanical Systems for Nanomechanical Testing: Electrostatic Actuation and Capacitive Sensing for High-Strain-Rate Testing’, *Exp Mech*, vol. 60, no. 3, pp. 329–343, Mar. 2020, doi: 10.1007/s11340-019-00565-5.
- [116] P. H. Pham, K. T. Hoang, and D. Q. Nguyen, ‘Trapezoidal-shaped electrostatic comb-drive actuator with large displacement and high driving force density’, *Microsystem Technologies*, vol. 25, no. 8, pp. 3111–3118, Aug. 2019, doi: 10.1007/s00542-019-04315-4.
- [117] J. Pons-Nin, A. Rodríguez, and L. M. Castañer, ‘Voltage and Pull-In Time in Current Drive of Electrostatic Actuators’, 2002.
- [118] J. B. C. Engelen, ‘Optimization of comb-drive actuators’, University of Twente, Enschede, The Netherlands, 2011. doi: 10.3990/1.9789036531207.
- [119] S. Xia and S. Nihtianov, ‘Capacitive sensors for displacement measurement in the subnanometer range’, in *Smart Sensors and MEMS: Intelligent Sensing Devices and Microsystems for Industrial Applications: Second Edition*, Elsevier Inc., 2018, pp. 87–99. doi: 10.1016/B978-0-08-102055-5.00004-8.
- [120] C. M. Chang, S. Y. Wang, R. Chen, J. Andrew Yeh, and M. T. Hou, ‘A comb-drive actuator driven by capacitively-coupled-power’, *Sensors (Switzerland)*, vol. 12, no. 8, pp. 10881–10889, Aug. 2012, doi: 10.3390/s120810881.
- [121] R. Legtenberg, A. W. Groeneveld, and M. Elwenspoek, ‘Comb-drive actuators for large displacements’, 1996.
- [122] Y. Ura, K. Sugano, T. Tsuchiya, and O. Tabata, ‘Tensile testing of fullerene nano wire using electrostatic MEMS device’, in *TRANSDUCERS 2009 - 15th International Conference on Solid-State Sensors, Actuators and Microsystems*, 2009, pp. 2062–2065. doi: 10.1109/SENSOR.2009.5285640.

- [123] S. Iqbal and A. Malik, ‘A review on MEMS based micro displacement amplification mechanisms’, *Sensors and Actuators, A: Physical*, vol. 300. Elsevier B.V., Dec. 01, 2019. doi: 10.1016/j.sna.2019.111666.
- [124] P. Schmitt and M. Hoffmann, ‘Engineering a Compliant Mechanical Amplifier for MEMS Sensor Applications’, *Journal of Microelectromechanical Systems*, vol. 29, no. 2, pp. 214–227, Apr. 2020, doi: 10.1109/JMEMS.2020.2965260.
- [125] J. Pribošek and M. Eder, ‘Parametric amplification of a resonant MEMS mirror with all-piezoelectric excitation’, *Appl Phys Lett*, vol. 120, no. 24, p. 244103, Jun. 2022, doi: 10.1063/5.0087067.
- [126] A. Bagolini, B. Margesin, A. Faes, G. Turco, and F. Giacomozzi, ‘Novel test structures for stress diagnosis in micromechanics’, in *Sensors and Actuators, A: Physical*, Sep. 2004, pp. 494–500. doi: 10.1016/j.sna.2004.03.050.
- [127] B. P. Van Dneenhmzen, J. F. L. Goosen, P. J. French, and R. F. Wolffenbittel, ‘Comparison of techniques for measuring both compressive and tensile stress in thin films’, 1993.
- [128] Z. Liu, Q. A. Huang, and W. Li, ‘Analysis of optimized micro-rotating-structure for MEMS’, in *International Conference on Solid-State and Integrated Circuits Technology Proceedings, ICSICT*, 2004, pp. 1747–1750. doi: 10.1109/icsict.2004.1435171.
- [129] L. J. Currano *et al.*, ‘MEMS rotational actuator for high force and large displacement’, in *CIMTEC 2008 - Proceedings of the 3rd International Conference on Smart Materials, Structures and Systems - Smart Materials and Micro/Nanosystems*, Trans Tech Publications Ltd, 2008, pp. 372–377. doi: 10.4028/www.scientific.net/AST.54.372.
- [130] P. J. French *et al.*, ‘The Development of a Low-Stress Polysilicon Process Compatible with Standard Device Processing’, 1996.
- [131] J. Burns *et al.*, ‘Lincoln Laboratory’s 3D Circuit Integration Technology’, in *Handbook of 3D Integration: Technology and Applications of 3D Integrated Circuits*, vol. 2, John Wiley and Sons, 2008, pp. 393–411. doi: 10.1002/9783527623051.ch20.

- [132] N. Gupta *et al.*, ‘Design and fabrication of SOI technology based MEMS differential capacitive accelerometer structure’, *Journal of Materials Science: Materials in Electronics*, vol. 30, no. 16, pp. 15705–15714, Aug. 2019, doi: 10.1007/s10854-019-01955-0.
- [133] H. Moriceau, F. Fournel, and F. Rieutord, ‘Materials and manufacturing techniques for silicon-on-insulator (SOI) wafer technology’, *Silicon-On-Insulator (SOI) Technology*, pp. 3–51, Jan. 2014, doi: 10.1533/9780857099259.1.3.
- [134] H. Moriceau, F. Fournel, and F. Rieutord, ‘Materials and manufacturing techniques for silicon-on-insulator (SOI) wafer technology’, in *Silicon-On-Insulator (SOI) Technology*, Elsevier, 2014, pp. 3–51. doi: 10.1533/9780857099259.1.3.
- [135] P. Li, X. Li, E. Li, Q. Shen, and H. Chang, ‘Design and fabrication of an in-plane SOI MEMS accelerometer with a high yield rate’, in *2015 IEEE 10th International Conference on Nano/Micro Engineered and Molecular Systems, NEMS 2015*, Institute of Electrical and Electronics Engineers Inc., Jul. 2015, pp. 511–514. doi: 10.1109/NEMS.2015.7147480.
- [136] Y. Gangamwar, S. Chate, M. Bhandare, V. Deo, and H. N. Deshpande, ‘Analytical, Experimental Determination of Deflection of Curved Beams and its Validation’, *International Journal of Innovative Research in Science, Engineering and Technology (An ISO)*, vol. 3297, 2007, doi: 10.15680/IJRSET.2015.0506158.
- [137] H. Ahuett-Garza, O. Chaides, P. N. Garcia, and P. Urbina, ‘Studies about the use of semicircular beams as hinges in large deflection planar compliant mechanisms’, *Precis Eng*, vol. 38, no. 4, pp. 711–727, 2014, doi: 10.1016/j.precisioneng.2014.03.008.
- [138] J. Yan Editor, ‘Micro and Nano Fabrication Technology’. [Online]. Available: <http://www.springer.com/series/13903>
- [139] H. H. Gatzert, · Volker, S. · Jürg, and L. Tools, ‘Micro and Nano Fabrication’.
- [140] F. Mancarella, ‘SILICON MICRO-AND NANO-TECHNOLOGIES ETCHING’.

- [141] J. J. Allen, ‘Challenges of MEMS Design, Fabrication and Design Verification’. [Online]. Available: <http://www.mems.sandia.gov/>
- [142] D. R. Hines, N. P. Siwak, L. A. Mosher, and R. Ghodssi, ‘MEMS Lithography and Micromachining Techniques’, 2011, pp. 667–753. doi: 10.1007/978-0-387-47318-5_9.
- [143] M. Geissler and Y. Xia, ‘Patterning: Principles and some new developments’, *Advanced Materials*, vol. 16, no. 15 SPEC. ISS. pp. 1249–1269, Aug. 03, 2004. doi: 10.1002/adma.200400835.
- [144] F. Laermer, A. Schilp, K. Funk, and M. Offenber, ‘Bosch deep silicon etching: Improving uniformity and etch rate for advanced MEMS applications’, in *Proceedings of the IEEE Micro Electro Mechanical Systems (MEMS)*, IEEE, 1999, pp. 211–216. doi: 10.1109/memsys.1999.746812.
- [145] F. Laermer and A. Urban, ‘MEMS at Bosch – Si plasma etch success story, history, applications, and products’, *Plasma Processes and Polymers*, vol. 16, no. 9. Wiley-VCH Verlag, Sep. 01, 2019. doi: 10.1002/ppap.201800207.
- [146] M. Gad-el-Hak, *MEMS: applications*. CRC Press/Taylor & Francis, 2006.
- [147] A. Bagolini, P. Scauso, S. Sanguinetti, and P. Bellutti, ‘Silicon Deep Reactive Ion Etching with aluminum hard mask’, *Mater Res Express*, vol. 6, no. 8, May 2019, doi: 10.1088/2053-1591/ab2423.
- [148] A. Bagolini, S. Ronchin, P. Bellutti, M. Chistè, M. Verotti, and N. P. Belfiore, ‘Fabrication of Novel MEMS Microgrippers by Deep Reactive Ion Etching With Metal Hard Mask’, *Journal of Microelectromechanical Systems*, vol. 26, no. 4, pp. 926–934, 2017, doi: 10.1109/JMEMS.2017.2696033.
- [149] H. Xu, C. Liu, V. V. Silberschmidt, Z. Chen, and J. Wei, ‘The role of bonding duration in wire bond formation: A study of footprints of thermosonic gold wire on aluminium pad’, *Microelectronics International*, vol. 27, no. 1, pp. 11–16, 2010, doi: 10.1108/13565361011009469.